MICRO-DOPING IN ULTRAFINE-GRAINED GOLD BONDING WIRES

EFFIE CHEW YEONG HUEY

School of Materials Science and Engineering

A thesis submitted to the Nanyang Technological University
in fulfillment of the requirements for the degree of Doctor of Philosophy

2009

Acknowledgement

First of all, I would like to express my utmost gratitude to my school advisor, Associate Professor Wong Chee Cheong, who has taught me to think critically and see things in many different lights, often from very fun angle. His advices have benefited me beyond academic knowledge alone, and his belief in me has given me the confidence to believe in myself.

I am really fortunate, to have the chance to interact with many knowledgeable researchers and scientists in this field of study. I am forever in debt to Miss Hui Hui Kim from IMRE, who has helped me on performing FIBS, TEM and EELS study on many samples, with generous patience and gentleness. Also, I am very thankful to Dr Cristiano Ferraris, who, with his highly skilled technique, has captured TEM images of the highest possible quality for this project. I was often stuck with some ideas and I couldn't find people in similar field to discuss with. For this, I have to thank Dr Zhao Yong Hao from UC Davis and Dr Zhang Xi from UCLA, for the many inspiring discussions. I have learned so much from them, and those helps and coaching that they have rendered to me is most valuable.

Because of this project, I have been with Heraeus (formerly Kulicke & Soffa) for six years, three years as an attachment student and another three years as a staff. This is a

special experience, which is brought to me by Associate Professor Subodh Gautam Mhaisalkar and Dr Christopher Breach. I am lucky to have been led by so many great bosses during my course in K&S. Dr Breach and Mr. Frank Wulff has given me tremendous guidance on this project, without whom the accomplishment of this project would not have been possible. Also, my sincere thanks go to the VP of my division, Mr. Avi Pollak and Dr Jeff Seuntjens, for their big trust in my ability. Also, to the directors of my department, Dr Jamin Ling and Dr Johnny Yeung, who have been very supportive for me to complete my thesis. I have great colleagues in K&S, who have helped me in various ways. I want to thank these colleagues: Dominik for the many inspiring discussion, Mui & Zaiton for helping with sample preparation, and many of the colleagues for their support and friendship. While I was doing experiments in school, I also received lots of guidance from laboratory technicians, particularly those from Microelectronic Materials Lab, Polymer Lab and TEM/ SEM Characterization Lab. Some of the results are also gathered with the help of some PhD and FYP students: Saraswati, Xu Cong, Chek Ing, Janette, Ming Hui, Barbara, Donny and Kok Hong - I would like to thank them too.

I am grateful to have many great friends. My fellow PhD friends who encourage me: Lay Kuan, Lydia, Xiao Fang, Pei Wen, Yang Choo, Mary, Shu Chen; And my other friends who bear with my absence to many gatherings: Khin Khee, Lee Yen, Siao Lin, Wen Bin, Rachel, Chee Poh, Zhen Xuan…and many.

I am most thankful to my family members, for being there for me always. My sister, Noelle who is always so understanding and thoughtful; And my mum, being the greatest mum that I could imagine. This PhD journey is long, and it is only with the support of all of these people, some of whom I may not have mentioned here, that have kept me going. I would like to thank all those who gave me the possibility to complete this thesis.

Table of Contents

Abstract

Wire bonding remains the dominant form of interconnection technology, and is expected to be used in 85% of total IC units worldwide by 2010. As device miniaturization continues, the diameters of wires get finer, requiring higher mechanical strength from the thin wires for handling. However, strong wires with low ductility pose an insurmountable hurdle in manufacturing because of formability issues. Therefore, strategies to attain both high strength and ductility (dual improvement) in Au wires need to be developed, a goal shared by researchers in the field of nanocrystalline (NC) and ultrafine-grained (UFG) materials.

The objective of this study is to establish dopant selection criteria (in low ppm level) in Au wires to achieve the goal of dual improvement. In this thesis, the unique effect of Ca on simultaneously improving the strength (by ~60%) and ductility (by ~96%) of Au wires is demonstrated. Also, Ca is shown to retard high temperature creep by 4-6 times, where the activation energy, stress and grain size exponent all indicate that grain boundary (GB) diffusion mediated GB sliding creep has occurred. Also, the Hall-Petch coefficient is increased - these obvious impacts on GB-related properties have suggested the segregation tendency of Ca in Au wires.

The postulation that stacking fault energy (SFE) reduction is the underlying mechanism is confirmed by statistical measurement on stacking fault (SF) width/ density, where SFE is found to be reduced from 15-50 mJ/m^2 to 10-34 mJ/m^2. The observations

of a straighter slip mode, more evenly distributed dislocation network, higher dislocation density and increasing random texture have further supported this conclusion. The specific location of Ca is not identified in this work, as expected from the scarcity of direct evidence in the field. Simulation is used instead to show the segregation tendency of Ca. The resulting texture with higher Schmid factor has imparted ductility to the wires. Yield strength is enhanced, even in the presence of this texture change, due to more boundaries and defects. As localized, abundant twin and SF are emitted from the GB, it is seen that partial dislocation mediated process has occurred in this relatively large GS range of 100-500 nm, compared to the literature suggested range of 50-100 nm. It is inferred that on top of the usual dopant segregation to SF (as in coarse-grained metals), segregation to GB in UFG/ NC metals could enhance the effectiveness of SFE reduction. Considering the significant impact of SFE in UFG/ NC metals, segregating dopants is proposed to be an effective strategy for achieving dual improvement in this class of materials. This is observed here, that the effect of doping on strength is ~ 20 times more in UFG Au wires, compared to Au rod. This is also the first demonstration that strength and ductility can be simultaneously improved by the optimum combination of grain size and orientation.

The dopant selection criteria proposed here centers on the impact of dopant on SFE. Since segregation tendency is found to be relevant, segregation energy and the effect on GB cohesion upon segregation are examined. Requirements on six materials parameters are suggested: atomic size misfit, crystal structure, valency, electronegativity, segregation energy and strengthening energy, some of which are established via ab initio

simulation within the framework of density functional theory. These criteria are further verified in Au-Be and Au-Pt systems.

In summary, understanding on the effects and mechanisms of Ca in Au wires has been established. The objective of this work, i.e. to determine the criteria for dopant selection in Au wires to achieve high ductility and strength are successfully fulfilled. We have also demonstrated that the effectiveness of segregating dopant in reducing SFE to improve the strength of UFG Au wires is 20 times more than in Au rod. This suggests a strategy for the dual improvement in UFG/NC materials in general, and that the very much neglected part on the impact of alloying on the properties of UFG/ NC metals should be emphasized.

List of Figures

List of Tables

Chapter 1
Introduction

1.1 Background

Wire bonding remains the dominant form of interconnection in microelectronic industry, due to its cost effectiveness, flexibility and mature infrastructure. Wire bonding accounts for 90% of IC packages shipped in 2006, and is expected to stay as the mainstream in the packaging world (Fig. 1-1). Today, the current generation of device shrinkage translates into a requirement for a bond pad pitch of 40 μm. To realize six sigma processes with such ultrafine pitch bonding, technology advancement in every relevant area, including bonding equipment, bonding wire materials and capillary materials are essential (Vardaman, 2007).

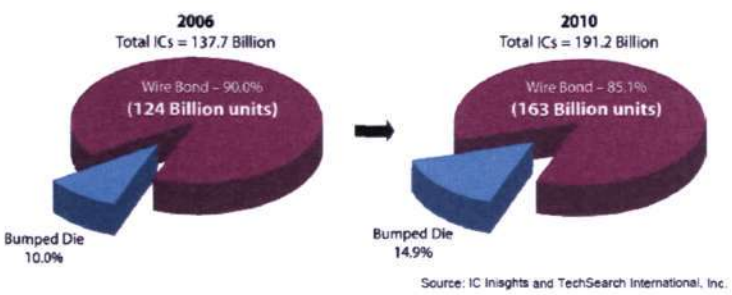

Fig. 1-1 Wire Bonding Market Share for IC Packaging. Bumped die includes flip chip, wafer level packages, gold bump driver ICs (Vardaman, 2007).

For bonding wire materials, one of the foremost challenges is the mechanical properties of fine wires. As diameters of wires get finer, wire strength decreases, and therefore wires need a higher inherent strength to start with for handling and service. So the first obvious requirement for Au wires is to have high strength. On the other hand, it is difficult to draw down wires to increasingly fine dimensions if they become too strong and brittle, so that translates into a need for ductility or formability. These requirements on strength and ductility become more stringent, as wire size decreases. Unfortunately, ductility and strength are often mutually exclusive properties, i.e., materials may be strong or ductile but are rarely both. This represents a quandary for the industry. Therefore, strategies to attain both high strength and high ductility (dual improvement) in Au wires are highly valued.

Optimization of wire mechanical properties is traditionally done empirically through alloying additions and is reported in numerous patents (e.g. Herklotz, 2001 and Kang, 1999). Clearly, to bonding wire producer, it is important to know the effect of various dopants, understand how they work, and to have some rule of thumb when it comes to dopant selection. However, there is very limited effort in attempting to understand the underlying working mechanisms of the dopants in Au wires, without which it is not possible to establish guidelines for dopant selection.

Au bonding wires go through extensive plastic deformation during the drawing process, therefore they have grain size in the UFG range, which is ~100-500 nm. (Chew, 2006). The goal of achieving concomitant high ductility and strength is shared by researchers in the field of NC and UFG materials (e.g. Koch, 1999). Most of the efforts done to accomplish dual improvement in UFG/ NC materials are

through manipulating the process. On the other hand, data on the effects of alloying/ doping are limited (Koch, 2003). Still, these valuable data highlights the differences in the alloying effects and mechanisms in UFG/ NC materials, compared to CG materials (e.g. He, 2003 and Song, 2005). For example, optimum distribution of carbon second phase of certain size can give rise to higher strain hardening rate in UFG steel, leading to higher ductility, as strain hardening (plastic instability) is the major limiting factor in NC/ UFG materials (Song, 2005). On the other hand, precipitation hardening is known to induce high strength at the expense of ductility in CG metals (Hertzberg, 1996).

Therefore, detailed mechanism study of dopant in UFG Au wires that will ultimately lead to selection rules of dopant is crucial for bonding wire manufacturer, as well as the research community in the areas of UFG/ NC materials.

1.2 Objective and scope

The objective of this thesis is to establish criteria for dopant selection in order to produce Au wires with high ductility and strength. Also, the dopants have to be effective at very low doping level (ppm), to conform to the general requirement of low doping level in Au bonding wires. In this thesis that limelight belongs to Ca.

The scope of this thesis includes:

1. Effects of Ca on room temperature tensile properties and high temperature performance of Au wires

First, we search for a dopant which could realize dual improvement in Au wires. It was reported that stacking fault energy (SFE) reduction can lead to dual improvement in UFG Cu (Zhao, 2006a). While selecting the first test vehicle, calcium (Ca) is chosen as it is a well-known strengthener in wire bonding industry (Kang, 1999; Hosoda, 1989). This element is also selected for its potential to effectively reduce SFE of Au wires, as it has low solid solubility in gold (Reed-Hill, 1991) and has high valency (Murr, 1975). It is found that Ca concurrently increases the strength and ductility of Au wires under multiple conditions, which is very desirable. For the benefits of certain wire application, the high temperature mechanical properties (creep) of Au wires are also investigated, as a function of Ca. Creep properties are studied with dynamic mechanical analyzer (DMA) and Hall-Petch coefficient is established by both tensile test and microstructure study with scanning electron microscopy (SEM).

2. Mechanisms of Ca-induced dual improvement of ductility and strength in UFG Au wires

A series of tests are designed, with the purpose of understanding the mechanisms of Ca induced dual improvement in Au wires. The form of Ca and the microstructures of Au wires are understood with combined techniques of optical microscope, SEM, electron dispersive X-ray (EDX), high resolution transmission electron microscopy (HRTEM), electron energy loss spectroscopy (EELS) and

electron back-scattered diffraction (EBSD). Also, the change of SFE is also investigated with TEM. The suppression of plastic instability via increasing strain hardening (leading to larger uniform elongation) and strain rate sensitivity (i.e. smaller activation volume) is the only established approach used for dual improvement in UFG/ NC studies (Ma, 2006), and are therefore examined in this study. To confirm on the observation of increased dislocation density from TEM study, stored energy measurement with differential scanning calorimetry (DSC) and microstrain estimation with x-ray diffraction (XRD) are conducted.

3. Dopant selection criteria for dual improvement in UFG Au wires

With the understanding on the working mechanism of Ca in Au wires, it is confirmed that Ca has obvious impact on the stacking fault energy (SFE). To propose material parameters for dual improvement, this should originate from the ability of the dopants to affect SFE of Au wires. The relevant behaviors are the segregation tendency of the dopant, and their impact upon segregation. This includes solid solubility of dopant in Au, atomic radius, electronegativity, crystal structure, valency, segregation energy and strengthening energy. The last two parameters can neither be found in literature nor be measured experimentally. For the deduction of these parameters, ab initio simulation within the framework of density functional theory, which is based on the thermodynamic model of Rice and Wang is performed. The proposed criteria are verified in two other binary systems, namely the Au-Be and Au-Pt systems, in agreement with published patents.

1.3 Thesis organization

This thesis is organized into 7 chapters. First in chapter 1 we start off with a general overview on the background, objective and scope of this thesis. Relevant literature in two major areas, wire bonding and progress in UFG/ NC materials are summarized in Chapter 2. The executions of work, i.e. sample preparation and characterization methods are described in Chapter 3. From Chapter 4 to 6, we go through the results and discussion. Chapter 3 describes the effects of Ca on both room temperature and high temperature mechanical properties of Au wires. A thorough investigation of the underlying mechanism is presented in Chapter 5. Building upon the understanding in previous chapters, we propose criteria in Chapter 6, for the selection of dopants to achieve dual improvement in Au wires. Finally, conclusions and future work are discussed in Chapter 7.

Chapter 2

Literature Review

In this chapter, two broad categories that are relevant to wire bonding technology and UFG/NC metals are reviewed. On wire bonding technology, we briefly touch on the production and wire bonding process of bonding wires, as well as critical requirement of bonding wires. Secondly, we concentrate on recent development and peculiar characteristic of plastically deformed UFG/NC metals, which is different from their CG counterpart. The focus is laid upon mechanical properties and various efforts to achieve simultaneous high ductility and strength, which is the topic of this thesis.

2.1 Wire Bonding Technology

All wire samples used in this project are specially designed engineering wires manufactured by Heraeus Materials Singapore. A general description of Au wire casting and wire bonding process are given below, some details are proprietary to Heraues and is therefore not mentioned.

2.1.1 Wire Manufacturing Process

The overall flow of the manufacturing process is shown in Fig. 2-1. Bonding wire materials are normally specified to be of relatively high purity to eliminate any undesired impurities. The starting material is the commercially available Au granules of 99.999% (5N) purity. Au bonding wire materials typically have high purity, meaning that low amount of total dopant alloy addition is used. As the amount of dopants required is unmanageably small, it is a common practice to add the dopants in the form of master alloy, which is highly doped to 1000-2000 ppm. The wire alloy lot is made from the appropriate weight ratio of 5N Au and the required master alloys of each required dopants. Continuous casting is used to produce a rod that is convenient for subsequent drawing process. The Au is melted under first vacuum, then back filled with inert gas during casting. This highly automated and efficient casting process provides both improved mechanical properties and compositional homogeneity which are crucial to wire bonding application.

The as-cast rod is then subjected to multi-die drawing process to reduce wire diameter to its desirable value. Intermediate annealing is performed and samples are taken for the verification of chemical uniformity and hardness. All drawing machines employ lubricant and the condition of lubricant is regularly monitored. Different combination of break load and elongation are required for the diversity of bonding wire applications. This is achieved with final annealing of the bonding wires.

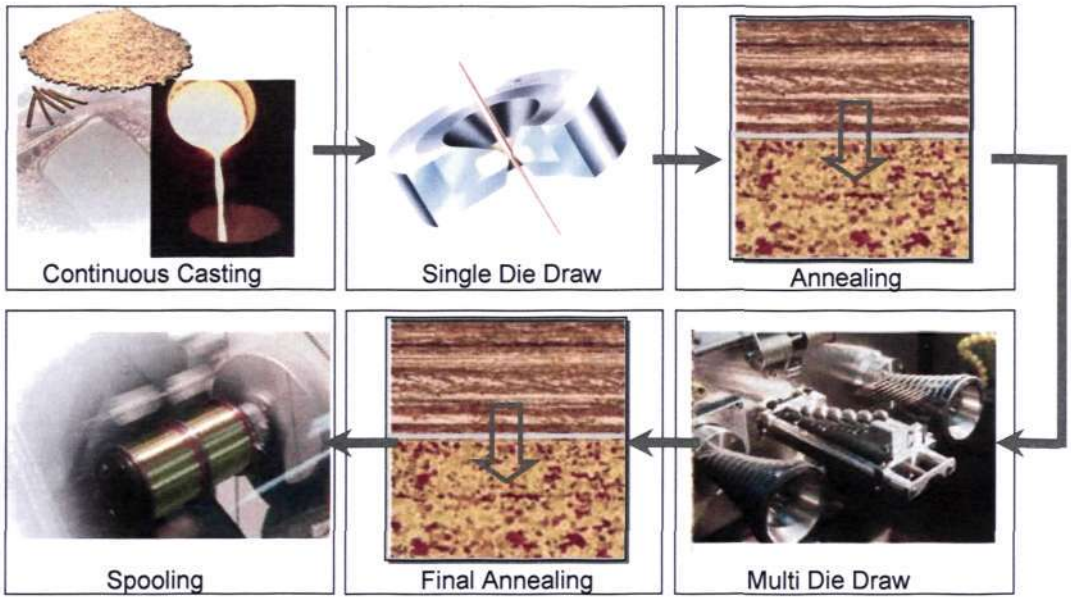

Figure 2-1 Wire manufacturing process flow (Stephan, 2008).

Extremely pure gold (>99.999% wt Au) is simply too soft and unstable for successful wire drawing and wire bonding. Therefore, it is a common practice to add various dopants at ppm level (by weight) into the high purity gold. This study focuses on Ca and Au-Ca phase diagram is attached here for reference (Fig. 2-2).

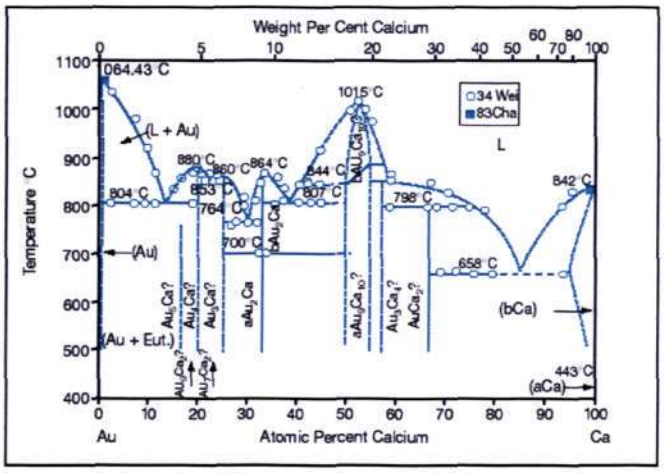

Figure 2-2 Au-Ca phase diagram (Massalski, 1986).

2.1.2 Wire Bonding Process

A brief description of wire bonding process is included here, to illustrate how the wires are being applied in final application. The wire bonding process begins with the ball formation at the capillary. Au wire is fed through the capillary and a spark would melt the wire and surface tension leads to the formation of ball at the end of the wire. The capillary presses against the bond pad on the die and squashes the ball. With a combination of pressure, heat and ultrasonic energy the ball bond is formed. The tool is raised and forms a wire loop as it moves towards the second bond position. The capillary makes contact to the lead-frame and a second bond is established like before. This time the second ball morphology pinches off the wire, leaving only a small 'tail' to hold the wire. This is the stitch bond and the cycles repeat. A typical bonding cycle is < 0.15 seconds per wire with two bonds (Fig. 2-3).

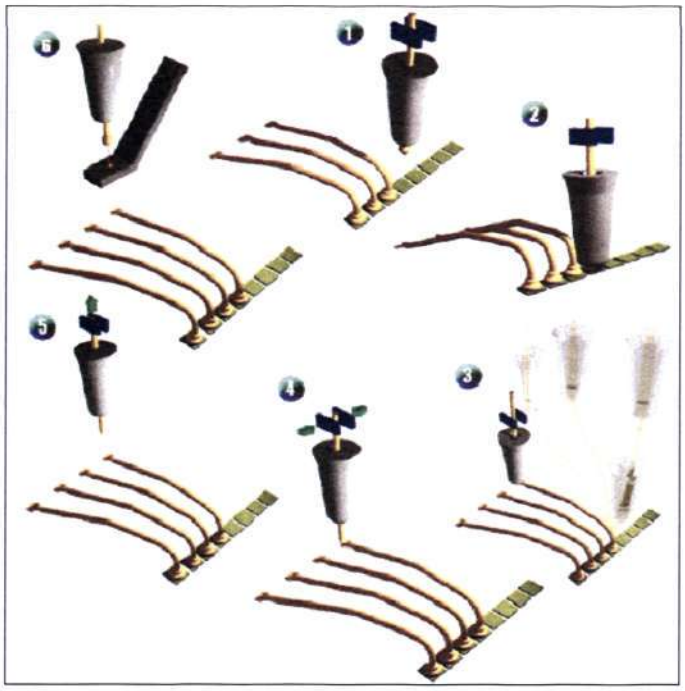

Figure 2-3 Basic gold ball wire bonding cycle (Small Precision Tool, 2009).

2.1.3 Critical Requirement of Bonding Wires

The materials requirement of the bonding wire depends on the application. For example, for automobile application, as a car is expected to be in service for > 10 years, stringent requirement on reliability is imposed. On the contrary, an inexpensive chip-on-board IC device used in a singing Christmas card, needs bonding wires that can be bonded at high speed to reduce cost, and come with minimum reliability requirement.

First and foremost, formability, which determines if a wire can be produced at high volume is an important consideration. After being manufactured, broadly speaking, bonding wires are to fulfill functions in three areas, namely bondability, reliability and

looping performance. Bondability refers to how easy a bond is formed, and how good is the bond formed. Bondability is becoming more and more challenging, as the more fragile low k substrate gains popularity. Second, the focus of wire bonding is to create a perfect metallurgical interface, and that this interface stays strong throughout service, which this is quantified in reliability test. Typically reliability reduces as the wire size shrinks. Third requirement is that it is important that the wire is strong enough to sustain through the entire mechanical load, maintain the desired loop shape to avoid electrical shorting. This project focuses on the impact of dopant on the mechanical properties of Au wires, which is closely related to the manufacturing, looping and bondability of the wires.

2.2 Characteristics of Ultrafine-grained and Nanocrystalline Metals Produced Via Plastic Deformation

Even though Au wire interconnection is a mature and established technology, the approach used has been more empirical so far. Most research in this area focus on *how* to solve problems in wire bonding, but not *why*. Typical 25 μm Au wires are manufactured through several stages of drawing processes, which resulted in heavily deformed, fine fibrous grain structure of ~100-500 nm (Chew, 2006). The final grain size (GS) corresponds to the GS of UFG materials, which with NC materials, this class of materials emerges as a relatively new area of research in materials science. In the mid-1980s, Gleiter made the visionary arguments that metals and alloys, if made NC would have a

number of appealing mechanical characteristics of potential significance for structural applications. The definitions are:

Coarse-grained (CG): GS > 1 μm

ultrafine-grained (UFG): 500 nm >GS> 100 nm

nanocrystalline (NC): GS <100 nm

Both UFG and NC metals are considered as fine-grained (FG) materials (Dao, 2007). It has been concluded that this class of materials shares many commonalities with conventional heavy plastically deformed materials (Valiev, 1996). Therefore, many understanding on the mechanical properties of UFG Au wires are borrowed from the UFC/NC study.

Bulk FG materials can be synthesized via either a bottom-up approach, where the nanostructure is built atom by atom and layer by layer, or a top-down approach, where the fine structures are synthesized by breaking down the bulk microstructure into the nanoscale. Several major processing techniques include inert gas condensation, mechanical milling, electrodeposition, severe plastic deformation (SPD) etc. Among them, cold-drawn Au wires share the greatest similarity with FG metals produced with SPD method. Therefore we will benchmark mostly with this group of FG metals. Common SPD methods include equal channel angular pressing (ECAP), surface mechanical attrition treatment (SMAT) etc. (Gleiter, 2000).

2.2.1 Strength of UFG/NC Metal

The strength of materials generally scales with the inverse of GS, following the famous Hall-Petch Law. The Hall-Petch Law, which relates the yield strength (σ_y) of polycrystalline materials to its GS, can be written as:

$$\sigma_y = \sigma_o + k\ GS^n \qquad (2\text{-}1)$$

where σ_y = yield strength
σ_0 = friction stress
k = Hall-Petch coefficient
GS = grain size
n = exponent and is usually taken to be -0.5 for most FCC metals.

The Hall-Petch coefficient, k, can be regarded as a measure of the difficulty of slip transmittal across GB. Some author commented that k depends on the way the dislocation structure builds up during the deformation, and its meaning is not straightforward. Still in general, the k value is typically viewed as a "locking parameter", which measures relative hardening contribution of GB (Hertzberg, 1996), or as GB parameter that serves as obstacles to the propagation of deformation (Lu, 2001b).

Indeed, extremely high strength and hardness have been observed through nanostructuring, for example in the most studied copper (Cu) (Fig. 2-4). Note that most UFG Cu samples (with GS in the submicron regime) exhibit higher hardness and tensile strength than the Hall–Petch expectation. The possible reason may be related with

the fact that the UFG samples were prepared via SPD, in which dense dislocation walls, tangles, cell walls or even subgrain boundaries are formed. These are barriers to the motion of dislocations and hence strengthen materials. It is remarkable that a simple, relatively soft metal like Cu ($\sigma_y \sim 50$ MPa in CG state) can be made to exhibit strength as high as 1 GPa through nanostructuring. However, the mechanism for the continued Hall-Petch strengthening down to GS of 10 nm are not fully understood as yet, as the traditional picture of dislocation pileups are not expected to be applicable to NC grains.

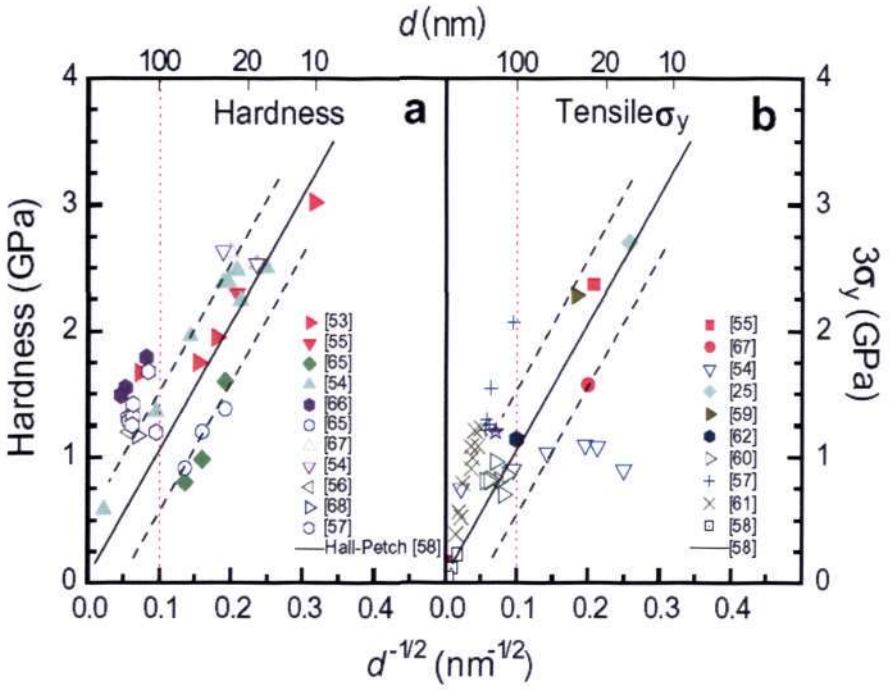

Figure 2-4 (a) Summary of experimental data from the literature on the GS dependence of strength of Cu specimens. The strength (or hardness) is plotted vs. $GS^{-1/2}$ (Dao, 2007).

enhanced to a level where they control plastic deformation. Therefore, one of the issues in debate has been whether the Hall-Petch relation breaks down at a critical GS (Dao, 2007), which some term this phenomenon as 'inverse Hall-Petch Law', or 'the strongest

GS (Lu, 2001b). One example is shown in Fig. 2-5 (Lu, 2001). This observation was first reported by Birringer and co workers (Birringer, 1984), various experiments have pointed to a departure from the linear relation when GS is in the nanometer range. As GS further decreases, the Hall-Petch plot could even exhibit a negative slope (Nieh, 1991). However, whether there is a true 'strongest GS' has not been fully confirmed experimentally, but mostly predicted by molecular dynamics (MD) simulation. Right now it is fair to say that simulation (Van Swygenhoven, 2001), as well as limited experiments on NC nickel (Ni) (Erb, 1995) have suggested that the critical GS for decreasing strength may be on the order of 7–15 nm. Many mechanisms have been put forward to interpret the negative Hall-Petch slope, most of which point to the migration of deformation mechanism, mostly GB related.

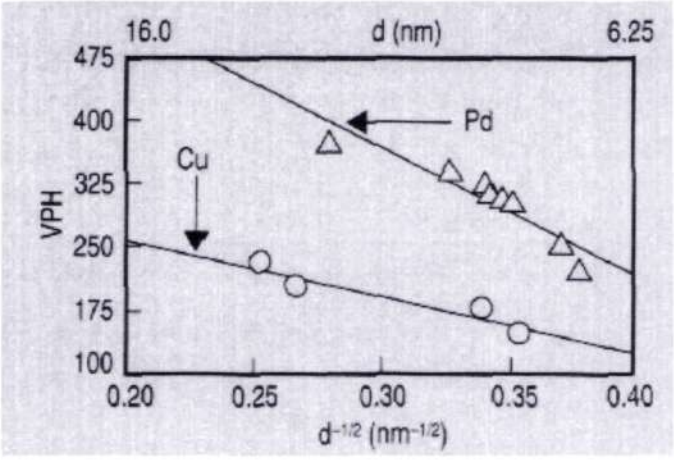

Figure 2-5 Deviation from linear relationship in NC Cu and Pd (Lu, 2001b).

2.2.2 Ductility of UFG/NC Metals

Like strength, ductility is predicted to increase as GS decreases. This expectation is based on experience with the conventional CG materials, in which GS affects yield and

fracture strength differently. As GS reduces, the fracture strength increases more than the yield strength, and the material becomes more ductile (Lu, 2001b). It is suggested that the small GS can lead to reduced flaw sizes and increased difficulties for the imposed stress concentration at the flaw to exceed the critical toughness, thus suppressing the crack nucleation/ propagation instability (Wang, 2002). Thus grain refinement is one mechanism that makes material both stronger and more fracture resistant than their CG counterparts (Courtney, 2000).

While the anticipated strength improvement over CG materials has indeed been realized, rarely has the predicted ductility enhancement been observed. In general it is reported that the ductility of NC/UFG metals is much lower than that of their CG counterparts, even for metals that are extremely ductile in CG form. For example, CG Cu can have EL as large as ~ 60%, while EL of Cu (100 nm > GS > 10 nm) reported ranged from 1% to 7%, as depicted in Fig. 2-6 (Lu, 2001b). Three major limitations of ductility for NC/ UFG materials can be identified. These are: (1) artifacts from processing; (2) force instability in tension; (3) crack nucleation or propagation instability (Koch, 2007).

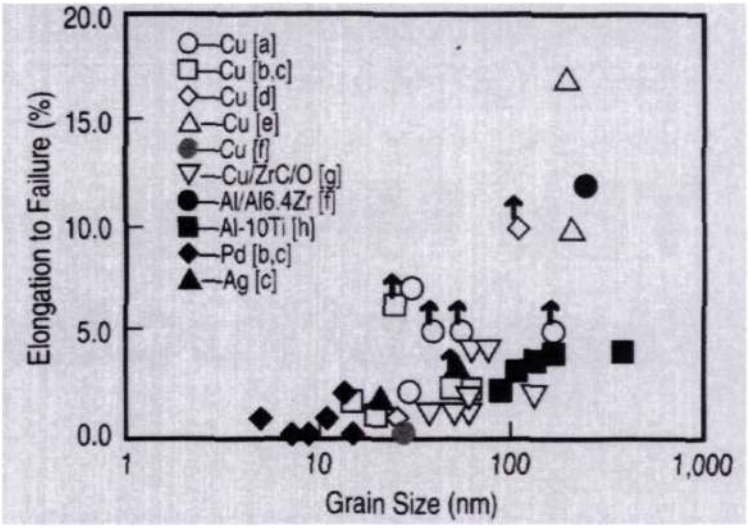

Figure 2-6 Plots of ductility vs. GS for several metals and alloys (Lu, 2001b).

Processing artifacts such as large residual stresses, porosity, contamination from gaseous and metallic species as well as the imperfect bonding between particles are inevitable, especially for specimens that were made by "two-step" processes that required a consolidation step. Several groups have demonstrated that after minimizing processing artifacts, NC/ UFG metals can indeed be made strong and ductile (Youssef, 2005a; Li, 2004). Also, the influence of specimen dimension on ductility needs to be taken into consideration (Erb, 2004; Zhao, 2008). Another major factor limiting the ductility is the tendency for plastic instability, such as shear band formation or necking. Localized deformation modes as such may occur in the early stage, due to the decreased strain hardening capacity (Dao, 2007). Since adequate ductility is frequently required in many applications, this has evolved as a critical barrier to the successful commercialization of UFG/NC metals.

2.3 Strategies to Attain Concurrent High Strength and Ductility in UFG and NC Metals

As previously discussed, strength improvement in UFG/ NC metals has been realized but not the ductility, the focus of effort in the community therefore gear more towards increasing ductility while maintaining the high strength. In the review by Ma, most routes used to improve the tensile ductility of bulk NC metals have their concepts rooted in enhancing strain hardening (n) and strain rate hardening (m) (Ma, 2006), as stated in Hart's criterion. In this section we will briefly go through the success so far.

To enhance n, one method is to introduce bimodal or multi-modal GS distribution. This is because the small grains can then maintain the strength level, while the bigger grains can act like conventional grains to contribute to strain hardening (Wang, 2004). For the same purpose, a mixture of two or more phases with varying size scales and properties is also effective (e.g. Song, 2005). Besides the original materials, one can also play around with deformation/ processing condition. For example, increasing deformation strain rate or using cryogenic deformation is helpful for improving m, and therefore ductility. These two methods are known for CG metals. It would be interesting to see if similar principles can be useful for FG metals as well. These differences are illustrated In Fig. 2-7. In Fig. 2-7a, the conventional CG Cu is represented by curve B. Curve A is the ECAP Cu with nanostructure, and curve C is for the bimodal nanostructure. Finally for curve D, the ECAP Cu was cold rolled at liquid nitrogen

temperature. In Fig. 2-7b, from curve A to D, the deformation strain rate increases progressively from 1 x 10^{-4} to 1 x 10^{-1} s^{-1}. It is clear that both n and ductility are higher with higher strain rate (Wang, 2004).

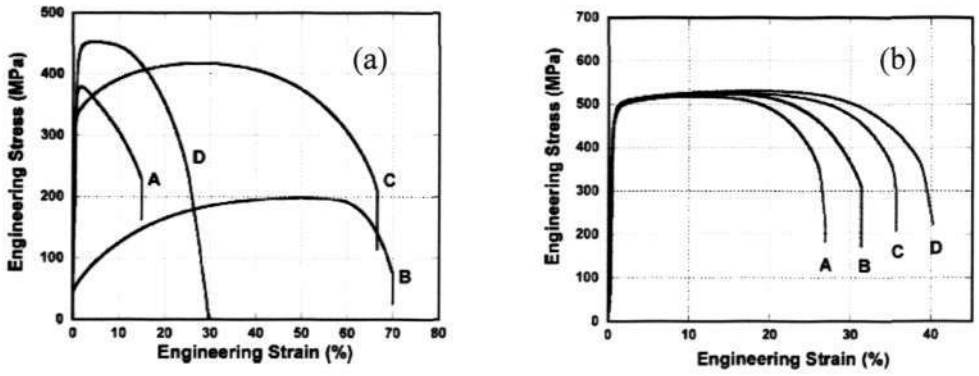

Figure 2-7 Room temperature testing engineering stress-strain curves (a) for Cu obtained by different microstructures (b) by different strain rate. Details are in text (Wang, 2004).

The second parameter from Hart's criterion, is the strain rate sensitivity m (Dieter, 1986). For FCC metals, GS in the NC range does increase m (e.g. Wei, 2004). The reasons are yet to be fully clarified, but the refined GS and the highly non-equilibrium GB structures may be promoting GB deformation mechanisms which offer a relatively high m (Valiev, 2002). One example is to introduce nanoscale growth twin, which can lead to both higher m (Dao, 2006) and n (Ma, 2004). These twins are referring to growth-in twin formed during processing, not during actual deformation test. Other approaches, namely transformation-induced plasticity (TRIP) and twinning-induced plasticity (TWIP), are also well established for conventional metals and alloys. It seems that TRIP is operative in NC/ UFG materials (Wu, 2005). Lastly, imperfection in bonding has been

one reason for the low ductility observed so far. Therefore, striving for flaw-free materials is one of the strategies for getting excellent mechanical properties in UFG/ NC metals. Very recently, there was a breakthrough in obtaining NC Cu of such quality at least for pieces on the order of 1 cm in diameter. The Cu was consolidated in-situ to full density from ball-milled nanostructured powders, rendering a final average GS of only 23 nm and a narrow GS distribution. This Cu is remarkably strong (stronger than all previous NC Cu) and at the same time ductile, while strain hardening at high rates (Youssef, 2005a).

Most of these current efforts done are through manipulating the process. In contrast, work on the effects of alloying/ doping in UFG/ NC materials are limited (Koch, 2003). And in most cases, the effects of alloying at higher concentration (not doping) which in general leads to second phase formation are studied (e.g. He, 2003; Zimmerman, 2002). For example, in the work done by Sun et al., multiple dopants were added into titanium to yield a multi-phase composite consisting of a micrometer-sized dendritic Ti-based solid solution intermixed with a UFG eutectic matrix. The tailored microstructure demonstrated both higher strength and tensile plastic strain (Sun, 2006). This thesis focuses on a much lower dopant concentration, at the ppm level, for which information is clearly lacking.

Chapter 3

Experimental Techniques

This thesis focuses on characterizing the mechanical and microstructural aspects of Au bonding wires. The experimental details of all techniques used will be described in this chapter. Also, more in-depth description will be highlighted on electron back-scattered diffraction (EBSD), transmission electron microscopy (TEM) and X-ray diffraction (XRD), which were used extensively in this project.

3.1 Electron back-scattered Diffraction (EBSD) Technique

Texture is a measure of the similarity in orientation of the crystal lattice within the constituent grains of a polycrystal. A single crystal would have the maximum texture, whereas a material where all grains have different orientations would have a random texture (Fig. 3-1). Traditionally, common techniques used for texture measurements are transmission electron microscopy (TEM), X-ray diffraction (XRD) and scanning electron microscopy (SEM) etc. Texture analysis is most commonly done using pole figures obtained by X-ray or neutron diffraction. Larger sampling volume is required for these methods, and this provides information of bulk or average texture but no information is available on individual grain (Weiland, 1986).

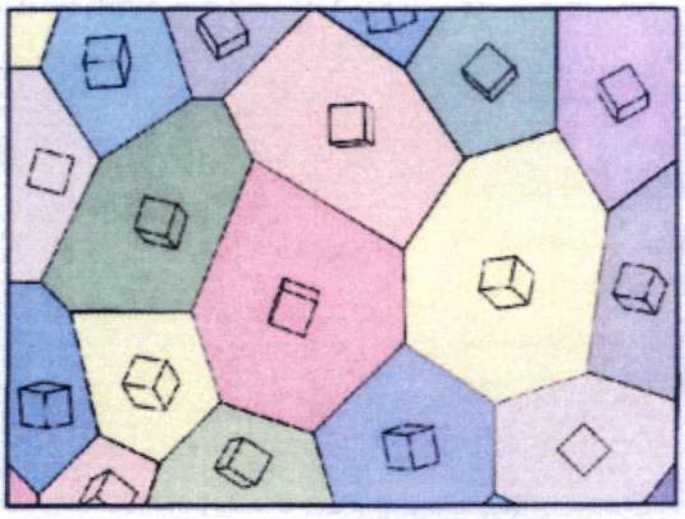

Figure 3-1 Schematic representation of texture of materials (Tan, 2003).

TEM has the advantage of giving information pertaining to grain boundaries (GB) such as the presence of precipitates, solutes, dislocations and atomic arrangement in GB together with misorientation measurements. Though TEM can give orientation information from grains larger than 10 nm and with high precision, inconvenience of sample preparations prevents this technique to be used effectively and routinely. It is impractical to obtain statistically significant quantities of data using TEM.

As for techniques which are attached with SEM, there are EBSD and selected area channeling (SAC). It is commonly accepted that EBSD has superseded SAC since the former has much better spatial resolution, relative ease of specimen preparation and the set up fits most microscopes. Comparing to other texture measurement techniques, the principle advantage of EBSD is that it provides a direct link between microstructure and

crystallography, which leads to the creation of a new area named "microtexture" (Randle, 1997).

3.1.1 General Principles

EBSD is based on the acquisition of diffraction pattern, which is essentially a backscattered Kikuchi pattern. They are formed as a result of divergence of the electron beam when it penetrates the material. The inelastically scattered electrons, satisfying Bragg's Law, are diffracted. The resultant loci of diffraction are two cones subtending twice the Bragg's angle between them. This is illustrated schematically in figure 3-2a. As the wavelength of the electron beam is small, Bragg's angle of diffraction is small, resulting in flat cones. The intersections of the flat cones on the screen appear as parallel lines. Kikuchi patterns are the projection of the geometry of crystal lattice planes. An imaginary line in the middle of and parallel to the Kikuchi band is a physical trace of the lattice planes. The intersection of two or more Kikuchi band is a crystallographic pole. By identifying the crystallographic planes and poles and their orientation with respect to a datum, it is possible to obtain the orientation of the crystal. A typical Kikutchi pattern obtained from Au wires is shown in Fig. 3-2b.

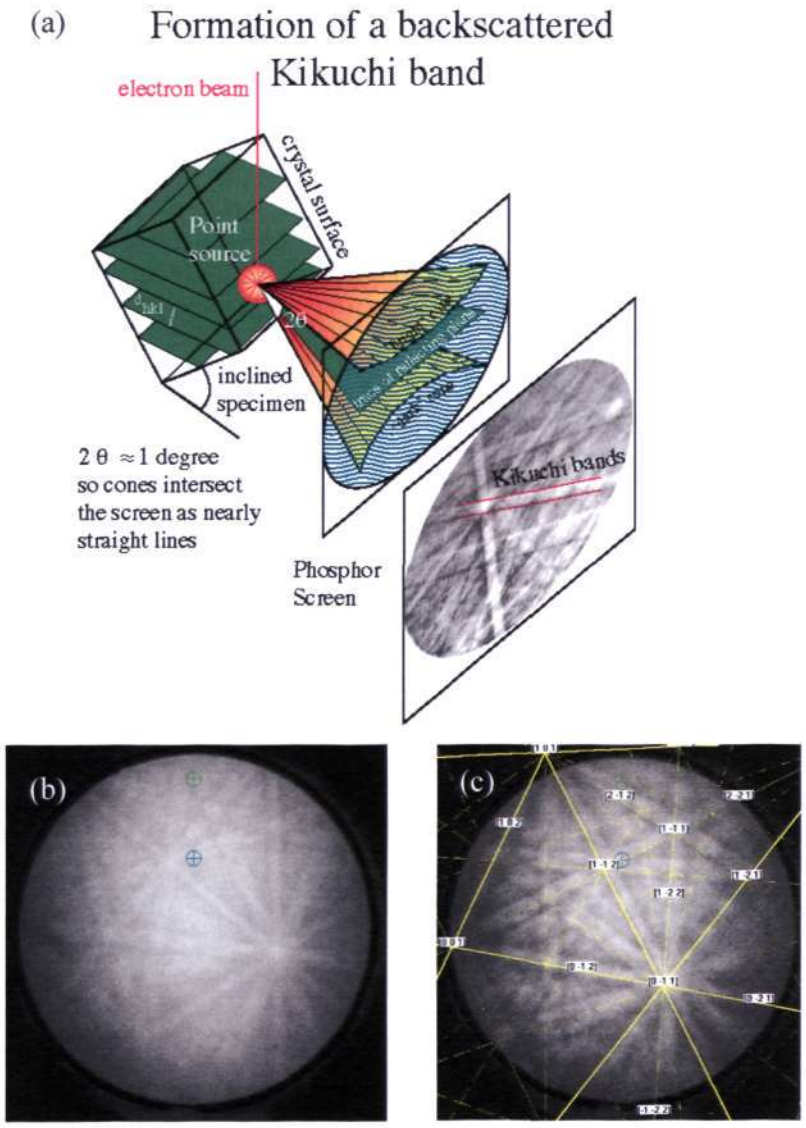

Figure 3-2 (a) Schematic illustration on the formation of Kikuchi pattern (Tan, 2003), (b) Typical Kikutchi pattern of Au wires before indexing and (c) after indexing.

3.1.2 Representation of Texture

A simple treatment of texture representation is given in this section, in relation to those that are used in this project.

Pole Figure

The pole figure is a stereographic projection (a projection of 'reference sphere space') of poles of chosen planes from each orientation, where the reference axes of the stereogram are those which correspond to the macroscopic specimen geometry. A typical choice will be the normal to the specimen surface from which EBSD measurements have been taken.

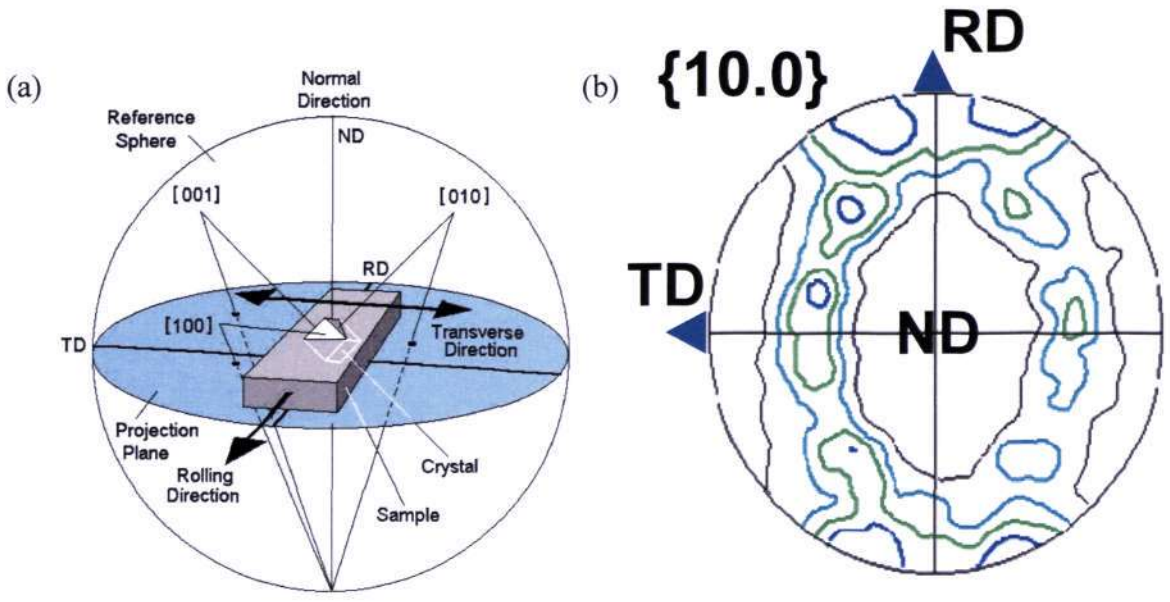

Figure 3-3 (a) Family of {100} poles in a cubic crystal projected onto the reference sphere of a steoreographic projection and (b) Typical pole figure (Randle, 1997).

Fig. 3-3a shows the family of {100} poles for one cubic crystal in a specimen which has been processed by rolling. Imagine a specimen to be placed at the center of the sphere, as the specified direction (normal direction facing upwards). Considering the (001) planes of the crystal, when their normal intersect with the sphere, the line is connected to the vertices of the sphere. The point where the arrow cuts across blue plane will leave a data point. Typical pole figure of Au wires is shown in Fig. 3-3b. Key features of the pole figure representation of EBSD data are that it has gained familiarity from its use in macrotexture studies. Also, its way of representation is compact, that a single projection at a time can be viewed (Randle, 1997).

Orientation distribution function (ODF) and Euler space

Pole figures give the distributions of the normal from a particular set of planes but not the distribution of the grain orientations. This only gives the most likely grain orientations present, and spatial distribution of the crystal orientations is not available, therefore the information from pole figure is incomplete (Weiland, 1986). A better description is given by the ODF which describes the orientation of all the discrete volumes in the aggregate, which the ODF is obtained from pole figures from different sets of planes.

ODF can be displayed in Euler space. The three independent variables which comprise an orientation can be described in terms of three rotations which, when applied in a specific sequence, effect the transformation between crystal axes and specimen axes.

Following Bunge definition, the crystallography axes are represented in the normal way in standard projection and the specimen direction is specified by the directions normal direction (ND), rolling direction (RD) and transverse direction (TD). Euler angles are typically expressed by $\{\varphi_1, \Phi, \varphi_2\}$, and represent the relative position of sample axes (ND, RD, TD) and crystal axes ([100], [010], [001]). Imagine the rotation of crystal, starting from an original position of sitting right along ND, RD and TD. Then imagining rotating the crystal (all rotations are in anti clockwise direction) about the ND (1st angle, φ_1), then rotate out of the plane (about the [100] axis, Φ), and lastly rotate by the 3rd angle (φ_2) about [001]. The rotation sequences are illustrated in Fig. 3-4, which the sequence is the rotation highlighted in red, then green and finally blue. Therefore the blue lines represent the final position of the crystal (Rollett, 2005).

Discrete orientations from EBSD can be displayed in Euler space, and appropriate contouring/ smoothing routines can make them appear identical to an ODF from XRD. However, there is a crucial difference: discrete orientations, as measured by EBSD, give directly the true orientation distribution whereas a macrotexture ODF from XRD has to be calculated, and there are inherent inaccuracies in this procedure. To summarize, the principal advantage of Euler space is that it contains more complete information about texture, especially when it is gathered from EBSD, as EBSD gives a direct ODF. Also, it affords comparisons with ODF which are familiar to the macrotexture community. A typical ODF displayed in Euler space is shown in Fig. 3-5 (Randle, 1997).

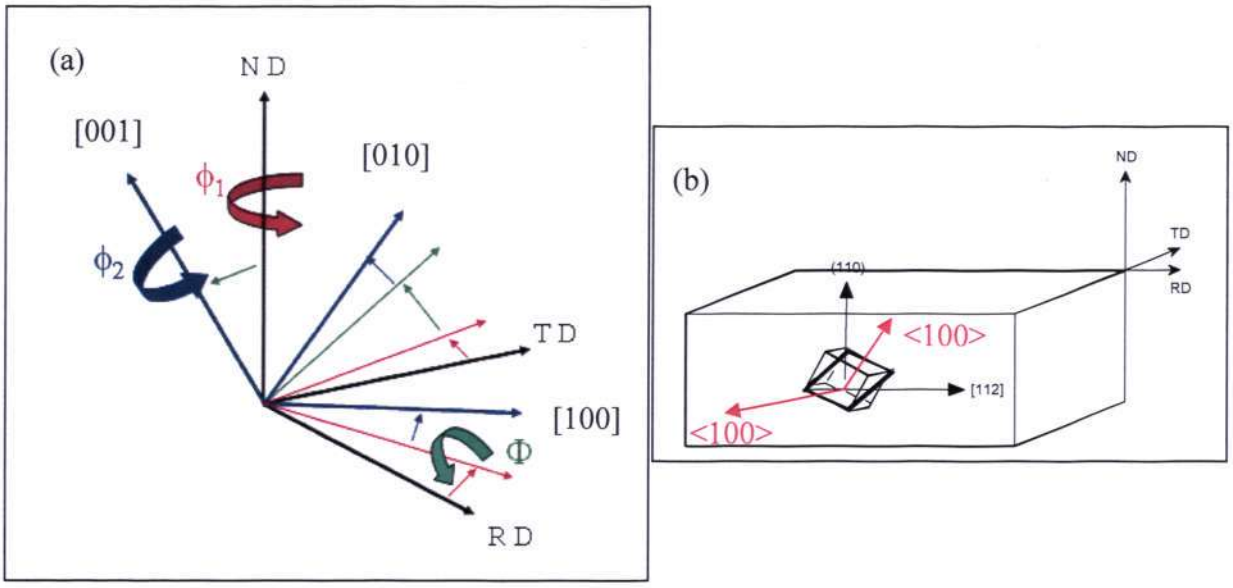

Figure 3-4 Definition of Euler angles, (a) sequences of rotations and (b) relative position of crystal and sample axis (Rollett, 2005).

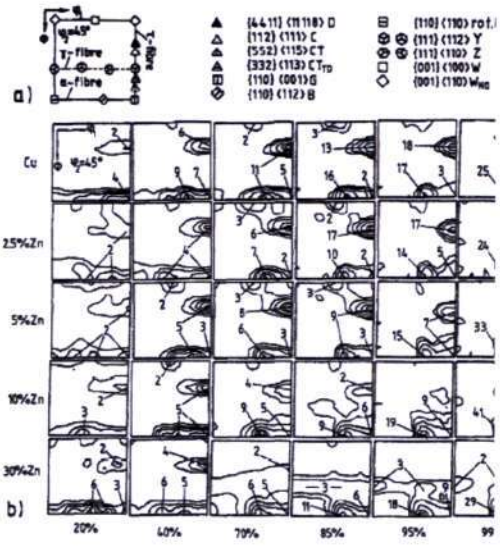

Figure 3-5 Typical orientation distribution function displayed in Euler space (Engler, 2000).

Orientation imaging map (OIM) and ratio of <100>/<111>

The most powerful data representation method of EBSD is orientation imaging mapping (OIM). This is a graphical way to plot the orientation computed from each diffraction pattern according to its spatial coordinates. Since an orientation comprises three independent variables, a compressed version of the parameter is calculated to render it convenient to use colour scale to denote regions of different orientation. The map is plotted according to its spatial coordinates, the location of discrete orientation changes are revealed in the plot as the change in color as shown in Fig. 3-6. Hence the plot provides a map of orientation with respect to position in the microstructure. OIM is very powerful as it links orientation directly to microstructure. It can be seen in Fig. 3-6 that the microstructure only focuses well in the middle portion of the image, but is blur at the two sides. This is because of the slanted position of EBSD holder in SEM, which is to enhance signal collection. With the OIM, the ratio of grains with wire texture of <100> and <111> can then be estimated and compared.

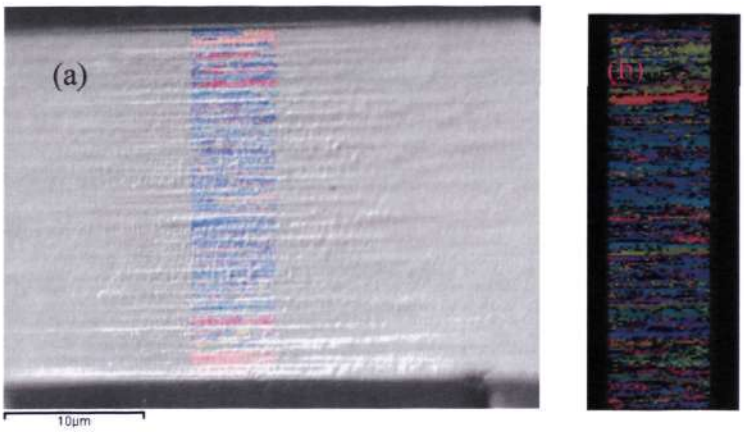

Figure 3-6 (a) Superimpose of orientation imaging map (OIM) onto the SEM captured microstructure and (b) OIM alone.

Coincidence Site Lattice (CSL)

The coincidence site lattice (CSL) is a model which has been adopted widely for classification of GB geometry, especially in cubic materials. These are the idealized GB which their misorientations permit certain atoms to belong to the lattices of both grains- CSL site- forming an interface of a kind of superlattice common to two grains. Its characteristic depends on the axis, <hkl>, about which the rotation is made, and the angle of rotation (the misorientaion angle). CSL may be generated by (Murr, 1975):

$$\Sigma = x^2 + Ny^2 \qquad (3\text{-}1)$$

where Σ is the ratio of the area of the coincidence lattice cell to that of the original lattice; x and y are non-negative integers representing Cartesian coordinates of the lattice point joined to an origin; and $N = h^2 + k^2 + l^2$. Two issues which affect CSL classification are the upper cut-off value of Σ and the spread permitted around the exact CSL configuration. On the whole as the Σ-value increases there is less chance of the boundary having 'special' properties; but since this is not an exact relationship there is no prescriptive upper limit for Σ. The mode value, compiled from the existing literature, is 29. For textured materials, usually a higher upper cut-off is more appropriate. By far the well-used rule to define the maximum allowable spread around a CSL, V_m, is the 'Brandon criterion' (Randle, 1997):

$$V_m = 15\Sigma^{-1/2} \qquad (3\text{-}2)$$

3.1.3 Experimental Details

Samples for EBSD study were mounted in epoxy and prepared by standard metallographic procedures, with careful attention paid to avoid smear and surface work hardening. Samples were then etched with aqua regia for slightly longer etching time, to remove any mechanical strain on wire surface that could cause diffuseness in the Kikutchi pattern. For every composition, ten wire strands from two batches of casting were studied.

The EBSD experiment was performed using the Oxford Instrument Link Opal EBSD system attached to a JEOL JSM-5410LV SEM at 25 kV. The mesh sizes are ~0.02 μm^2 and ~0.09 μm^2 for Ca-doped Au wires and pure Au wires respectively, which the former is the smallest possible mesh size. Calibration of the EBSD system was carried out using single-crystal germanium with [001] being the surface normal and the [110] parallel to the horizontal edge.

3.2 Transmission Electron Microscopy (TEM) & Energy Loss Spectrometer (EELS)

3.2.1 General Principles of TEM

A schematic of transmission electron microscope (TEM) is shown in Fig. 3-7. As opposed to a light microscope, the TEM operates with electrons instead of light. Using an electron microscope offers the advantage of increasing both the magnification of an object and the resolution over other imaging tools. TEM images are formed in two stages. The first stage consists of scattering of an incident electron beam by a specimen, followed by the formation of diffraction pattern at the back-focal plane by the objective lens. The second stage consists of the formation of the primary image by Fourier transform of the diffraction pattern and the magnification of the primary image by a series of projection lenses (William & Carter, 1996).

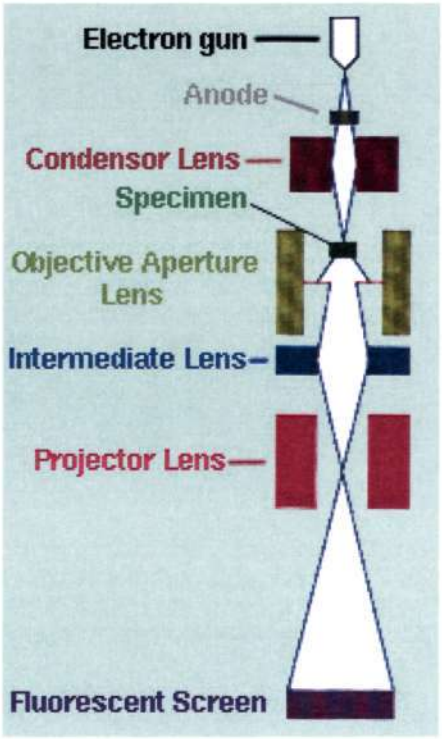

Figure 3-7 A schematic of the TEM (Walker, 2009).

Because an image has to be reconstructed from diffraction pattern, it is important to understand the possible contrast mechanism which will determine whether a feature will appear dark or bright in an image. TEM image contrast arises because of the scattering of the incident beam by the specimen. As a consequence the electron wave can change both in amplitude and in phase as it traverses the specimen and both these kinds of change can give rise to image contrast. In most images, both types of contrasts contribute but one will tend to dominate. The two principal types of amplitude contrast are the mass-thickness contrast and the diffraction contrast. Mass-thickness contrast arises from incoherent elastic scattering of electrons and is a strong function of the atomic number and thickness, i.e. regions which are thicker and of higher density will appear darker in the image. If the specimen is crystalline then an additional diffraction contrast is encountered. Amplitude contrast is used to produce bright field or dark field images by selecting the direct or scattered electrons respectively. On the other hand, phase contrast is due to the differences in phase of the electron waves scattered through the thin specimen. A phase contrast image requires the selection of more than one beam. In general, the more beams are collected, the higher is the resolution of the image. This differs from the case of bright field or dark field image, which require us to select a single beam using the objective aperture. A more common type of phase contrast image is the high-resolution transmission electron microscopy (HRTEM) images. Good HRTEM images can only be obtained when (Ferraris, 2007):

1. Thin specimen, since inelastic scattering will tend to degrade the image quality
2. The microscope must be aligned as accurately as possible

3. The objective lens astigmatism must be minimized
4. The specimen must be carefully tilted so that the beam direction coincides with a crystallographic axis

3.2.2 General Principles of EELS

The principle of EELS is based on a form of inelastic scattering that knocks out an inner shell electron. The signal produced is less pronounced in intensity for elements of high atomic number since the critical energy to excite X-ray increases with atomic number. As such it is generally used for light elements, and it has the advantage of detecting elements whose X-rays are too soft to be counted e.g. helium and lithium. As shown in Fig. 3-8 an EEL spectrum is conventionally considered to consist of 3 regions. Those electrons (usually the majority) that have suffered negligible inelastic scattering contribute to the zero lost peaks. For analytical purpose, the characteristic edges that correspond to inner shell excitation are useful, as they are characteristic of the element as are X-ray peaks. Leapman and Hunt showed that EELS can detect smaller amounts of an element than EDX spectroscopy for elements below sodium ($Z<11$) based on K-shell excitation, or below iron ($Z<26$) using L-excitation (EELS, 2006), and that the detection of Ca ($Z=20$) in the parts per million ranges has been reported in an EELS study on MgO (Yan, 1998). It is thus one of the most practical ways to study low level Ca segregation at the GB.

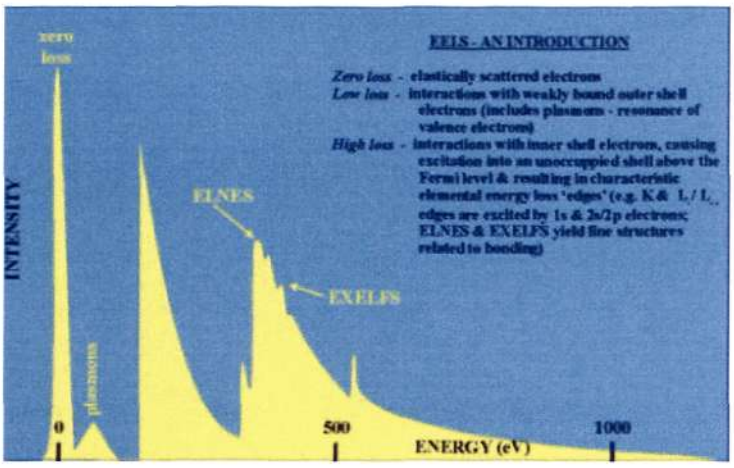

Figure 3-8 Typical EELS data (Walker, 2009).

3.2.3 Experimental Details

Sample preparation for TEM was done with FEI FIB200XP focused ion beam (FIB). Standard copper grid was cut into a half and used as a holder for wire, as shown in Fig. 3-9. FIB was performed on the area near to the tensile-fractured surface, the purpose is to capture the area which has undergone tensile deformation. The Au wires were cut using the ion beam at a high current of 6500 nA and 30kV. The current was subsequently tuned to 20k nA, 920 nA, and slowed down to 280 nA and finally ~90 nA to clean the surface. TEM investigations in this work were performed at 200 kV on a JEOL JEM-2100F field emission electron microscope equipped with double-tilt holder, CCD and TV-rate camera, and LINK ISIS EDS X-ray micro-analyzer. At least two samples and upto four samples are studied for every sample condition.

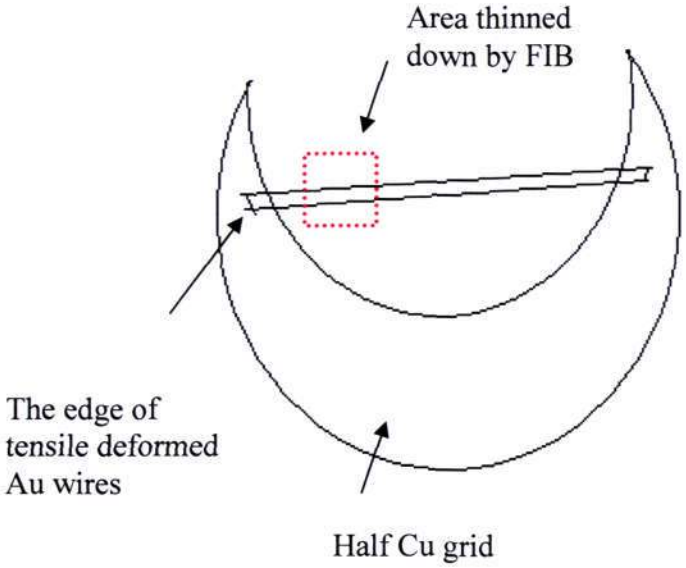

Figure 3-9 Schematic of FIB and TEM sample.

3.3 X-ray Diffraction (XRD)

3.3.1 General Principles

X-ray scattering techniques are a family of non-destructive analytical techniques which reveal information about the crystallographic structure, chemical composition, and physical properties of materials and thin films. These techniques are based on observing the scattered intensity of an X-ray beam hitting a sample as a function of incident and scattered angle, polarization, and wavelength or energy. In this section, discussion will focus on microstrain measurement with XRD.

Because of the interaction between grains, a single grain in a polycrystalline mass is not free to deform in the same way as an isolated single crystal would, if subjected to the same deformation. As a result, a plastically deformed grain in a solid aggregate usually has regions of its lattice left in an elastically bent or twisted condition. The metal is then said to contain microstress (also called residual stress) that vary from one grain to another, or from one part of a grain to another part, on a microscopic scale.

If grains are given a uniform tensile strain at right angle to the reflecting planes, their spacing becomes larger than d_o and the corresponding diffraction line shifts to lower angles but does not otherwise change, as shown in Fig. 3-10b. This line shift is the basis of the x-ray method for the measurement of macrostress. In 3-10c, the grain is bent and the strain is nonuniform; on the top (tension) side the plane spacing exceeds do, on the bottom (compressive) side it is less than d_o, and somewhere in between it equals d_o. We may imagine this grain to be composed of a number of small regions in each of which the plane spacing is substantially constant but different from the spacing in adjoining regions. These regions cause the various sharp diffraction lines indicated by the right on (c) by the dotted curves. The sum of these sharp lines, each slightly displaced from the other, is the broadened line. While macrostrain is a vector, microstrain is defined to be a scalar (Cullity, 1967).

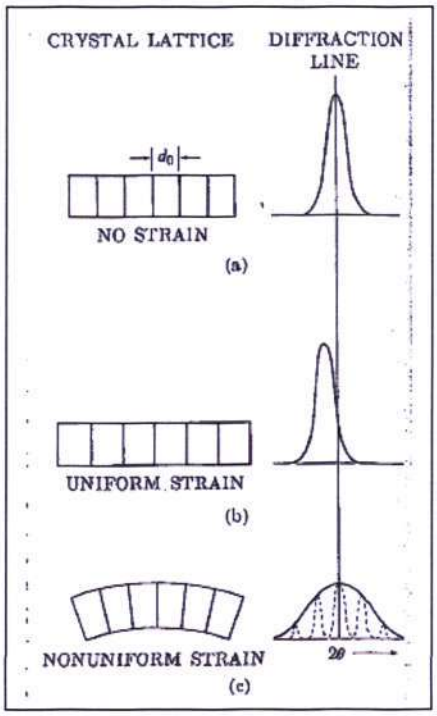

Figure 3-10 Effect of Lattice Strain on Debye-line width and position (Cullity, 1967).

3.3.2 Experimental Details

The fine wires were cut into length of not more than 15 mm and attached to a 15 mm x 10mm glass slide. Fine wires had to cover a sufficient area with no space in between the wires. The slide was then attached to the sample holder using carbon adhesives. Fig. 3-11 shows the sample together with the XRD sample holder.

Wire samples were characterized by Rigaku Dmax 2200 X-Ray Diffractometer system with CuK_α radiation operating at 50kV, 20mW. X-Ray Powder Diffraction (XRPD) data was collected in the range of 30 ° to 80° (2θ range). The scan rate was 2°

per minute at a scan step of 0.002. The contribution of $K_{\alpha 2}$ radiation were subtracted from the total profiles, thus the results obtained correspond to just $K_{\alpha 1}$ component of the K_{α} doublet. Through the broadening of the peaks detected, microstrain was then calculated with Williamson-Hall plot (Williamson, 1953). Three runs were repeated to confirm the trend observed.

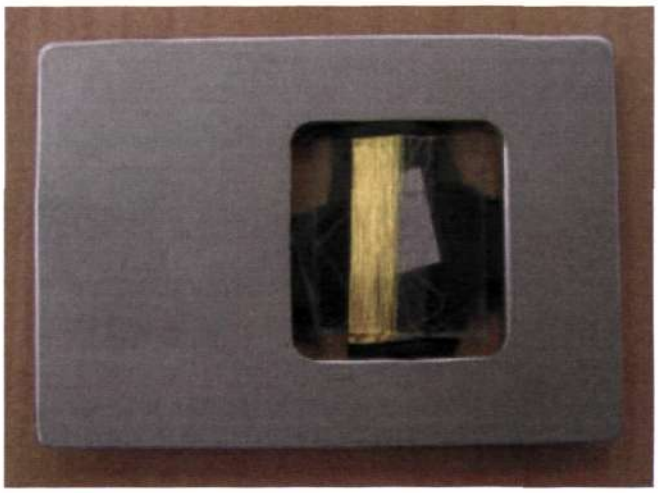

Figure 3-11 XRD sample together with sample holder.

3.4 Tensile Mechanical Testing

In this work, INSTRON 5543 Universal Tensile Testing Machine was used to conduct the tensile test at room temperature. The machine is operated by displacement control in mm/ min, the load cell used is 5N. The clamps of the machine are of the conventional type with certain type of tape added on to improve the gripping of the fine wire. The exact detail of the setup is proprietary to the company. Experimental procedures were set in accordance to ASTM Standard Test Method F 219 (ASTM, 1996).

The gauge length of specimen was 10 inch (254 mm) and the standard pulling speed was 1 inch per minute.

The strain rates were varied for the strain rate tests, where five strain rates within the range of 10^{-3} to 10^{-1} s^{-1} were used, which were 0.1, 0.017, 0.01, 0.005 and 0.001 s^{-1}, respectively. The initial load applied to the specimen before conducting the test was sufficient to keep the wire straight. Ten tests were conducted for each wire composition. In this test procedure, a specimen was subjected to a continually increasing uniaxial load, while simultaneous observation was made on the elongation by the extensometer. The applied load and extension readings were recorded.

3.5 DSC stored energy measurement

For sample preparation, wires were cut into small strand of about 5 mm to fit into the aluminium pan. Cutting was selected to minimize possible strain induced and to allow for tighter crimping as small wire strand can move more freely to fill in spaces in between wires, thus allow better heat conduction within sample. The sample pan was then crimped using an appropriate TA Instruments, Inc. sample press.

DSC measurements were carried out in a TA Instrument Heat Flux DSC 2010 with a heating rate of 40 ^{o}C/min going up to 450^{o}C, under nitrogen environment. It was air-cooled to 50^{o}C after the first heating. Without moving either the sample or the reference, a second run, programmed just like the first, was performed. The heat flow

values of this so-called second run were then subtracted from the initial measurements to separate those parts of the heat flow signal due to imbalance of the calorimeter (i.e. heat capacity of the two furnaces), mismatch of the heat capacity of sample and references or equipment signal noises. Heating rate of 40 °C/min was used in order to amplify our signal. Sample size was kept strictly between 18 to 22 mg. Precautions were taken in order not to diminish the indistinct signal. Cell cleaning, temperature calibration, cell calibration with Indium and also baseline calibration were carried out before each round of test run. Three runs were repeated to confirm the trend observed.

3.6 Creep study with Dynamic Mechanical Analyzer

Creep tests were performed with a dynamic mechanical analyzer (DMA) from Thermal Analysis (TA) Instruments (model no DMA 2980), under tension mode. As the wire diameter is too fine for the fiber clamp, film clamp was used instead. Grooved aluminium balls (also provided by TA Instruments) were used to clamp the wires at two ends. The gauge length used was kept constant at 20 mm.

Following the criterion for creep test, the force was selected to be lower than the 0.2% yield strength of the weakest sample in our collection (Au20Ca as defined in Chapter 4) at 513 K; And the temperatures are chosen to be lower than ~700 K (which is $0.4T_m$). With an initial static force of 0.001N, the temperature was ramped from room temperature to different test temperatures (493, 503 and 513 K) at 10°C/min. After the temperature has stabilized, the force was ramped at a rate of 0.005 N/min to the final

testing stress levels (67 and 88MPa). The data collection was then initialized when both the load and temperature have reached their respective target levels.

3.7 Determination of Hall-Petch Behavior

To examine the Hall-Petch behavior, annealing was employed to alter GS of Au wires. Au wires were wound loosely around a spool, paying special attention that the wires were not touching each other, to avoid wire sticking under high temperature. The wires were annealed at 573K , 673 K, 773 K and 873 K for half an hour, respectively. The temperature range was selected to cover the temperature before and after grain growth occurs. The recrystallization temperatures of both Au20Ca and Au90Ca(defined in Chapter 4), which were determined using DSC, were~ 613 K and 633 K, respectively.

3.8 Materials

All wire samples used in this project are specially designed engineering wires manufactured by Heraeus Materials Singapore. A general description of Au wire casting and wire bonding process are in Chapter 2.

The GS of Au20Ca is ~100 nm larger than the Au250Ca in the as-drawn state whereas it is ~1 μm larger in the annealed state (Kulicke, 2005). The effect of GS could

dominate over other factors. To single out the effects of GS, all wires in this study are wires in the as-drawn state, i.e. non-annealed wires.

Chapter 4
Beneficial effects of Ca in Au wires

Strength and ductility are two of the most important mechanical properties of structural materials. However, they are mutually exclusive, i.e. a material may be strong or ductile, but rarely both at the same time. This is the dilemma shared by both wire bonding producers and researchers studying the mechanical properties of UFG/ NC materials (Koch, 1999).

Here we focus on the unique effect of Ca that brings desirable concurrent improvement in ductility and strength of Au wires. First, the effect of Ca on room temperature tensile properties of Au wires is examined. Second, we also look at high temperature properties of Au wires with creep test. The results point towards a GB related mechanism, therefore we are interested to understand the impact of Ca on GB properties. For this purpose, the effect of Ca on Hall-Petch behavior is studied.

4.1 Composition of Au wires

The compositions of the wires studied in this work are as shown in Table 4-1:

Table 4-1 Code names and targeted compositions of Au wires

Code name	Concentration of Ca		
	ppm by weight	Atomic % (At %)	Weight % (Wt %)
Au5N*	~ 0	~ 0	~ 0
Au20Ca	20	0.01	0.002
Au60Ca	60	0.03	0.006
Au90Ca	90	0.04	0.009
Au250Ca	250	0.12	0.025
Au500Ca	500	0.24	0.05
Solid solubility (at 800°C)	3750	1.8	0.36

* Au5N is Au wires with 99.999% purity

Binary Au wires of the above mentioned intended compositions were prepared, and their compositions were verified with ICP-MS (Inductively coupled plasma mass spectrometry) technique. The actual compositions of the wires are listed in Table 4-2. It can be seen that the achieved dopant levels are usually quite near to the targeted values, except that Au500Ca has lower Ca content of ~ 400 ppm by wt. The other impurities are in general < 2 ppm by wt. All the wires have gone through exactly the same manufacturing process; therefore differences in their properties can be clearly attributed to the differences in Ca level.

Table 4-2 Actual compositions of Au wires (ppm by wt), determined with ICP technique

	Au5N	Au20Ca	Au60Ca	Au90Ca	Au250Ca	Au500Ca
Au	balance	balance	balance	balance	balance	balance
Ca	0.3	***21***	***58***	***87***	***210***	***400***
Zn	0.5	<0.5	<0.5	0.7	<0.5	<0.5
Ag	1.8	1.75	1.7	1.65	2	1.7
Al		<1	<1	<1	<1	<1
As		<2	<2	<2		
Be	<0.1	<0.1	<0.1	<0.1	<0.1	<0.1
Ce		<2	<2	<2	<1	<1
Cu	<0.5	<0.5	<0.5	<0.5	<0.5	<0.5
Fe	<2	0.7	<0.5	0.7	1.2	1.2
Ge		<2	<2	<2		
In		<2	<2	<2		
Mg		0.3	0.3	0.2	0.2	0.2
Mn		0.1	0.1	0.1	<0.1	<0.1
Ni	<0.5	<0.5	<0.5	<0.5	<0.5	<0.5
Pb	1	1.35	1.6	1.25	1.1	1.5
Pd	<0.5	0.75	0.7	0.7	<0.5	<0.5
Pt	<1	<1	<1	<1		
Si		<1	<1	<1		
Ti		0.1	0.1	0.1	<0.1	<0.1
Tl		<1	<1	<1		
Y		<0.1	<0.1	<0.1		

4.2 Effect of Ca on Tensile Properties of Au wires

Room temperature tensile properties of as-drawn Au wires at several levels of Ca are compared in this section. Fig. 4-1 shows the engineering stress strain curves of Au wires at five levels of Ca additions, from 20 ppm to 500 ppm. The stress strain curve of

Au5N wire is included as a reference. Even in the as-drawn state, Au5N has good ductility of ~3.5%, but has extremely low strength of ~ 100 MPa, which is one of the reasons why doping is needed for Au bonding wires. By adding only 20 ppm of Ca, the strength goes up to ~400 MPa, but the ductility is also significantly reduced to ~1.6%. The strength of Au wire is as high as ~700 MPa, at the highest Ca level of 500 ppm used. Ca is a well-known strengthener used in Au bonding wire industry, with their strengthening effects documented in many patents (Kang, 1999; Herklotz, 2001). Interestingly, Ca also has an obvious beneficial effect on the ductility of Au wires. It has been reported in one patent that Ca can prevent brittleness (Hosoda, 1989). From the results, it is clear that both ductility and strength of Au wires are progressively and consistently improved by Ca. However, ductility improvement seems to saturate and stop at Au500Ca. At this doping level also, second phases start to appear (section 5-1). For these reasons, subsequent study will focus only on wires with 250 ppm Ca and below.

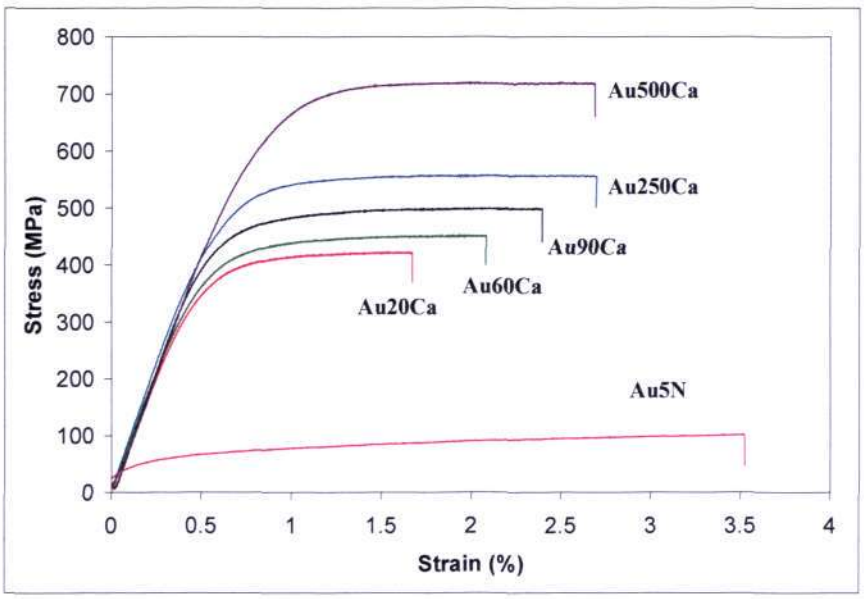

Figure 4-1 Engineering tensile stress strain curves of as-drawn Au wires at various levels of Ca.

A characteristic feature of these curves is a steep rise followed by yielding and a flat response under an essentially constant load until fracture. This absence of strain hardening after yield is termed elastic-perfectly plastic stress strain behavior, and is commonly observed in UFG and NC materials (Furukawa, 1997). This is believed to be caused by the small grains which can not contain dislocations because that image force is too low. The theory of the steady state (flat region) portion of tensile curves for UFG materials such as those in Fig. 4-1 is that strain hardening mechanisms such as dislocation pile up are not effective with the small GS (Zhu, 2004). In actual bonding application, Au bonding wires used are usually annealed wires. Wires used in this work were annealed at 500°C for ~ 3 min, and their stress-strain curves are plotted in Fig. 4-2. As mentioned, Au500Ca will be excluded, while Au5N is also omitted as it is too soft to be annealed at 500 °C.

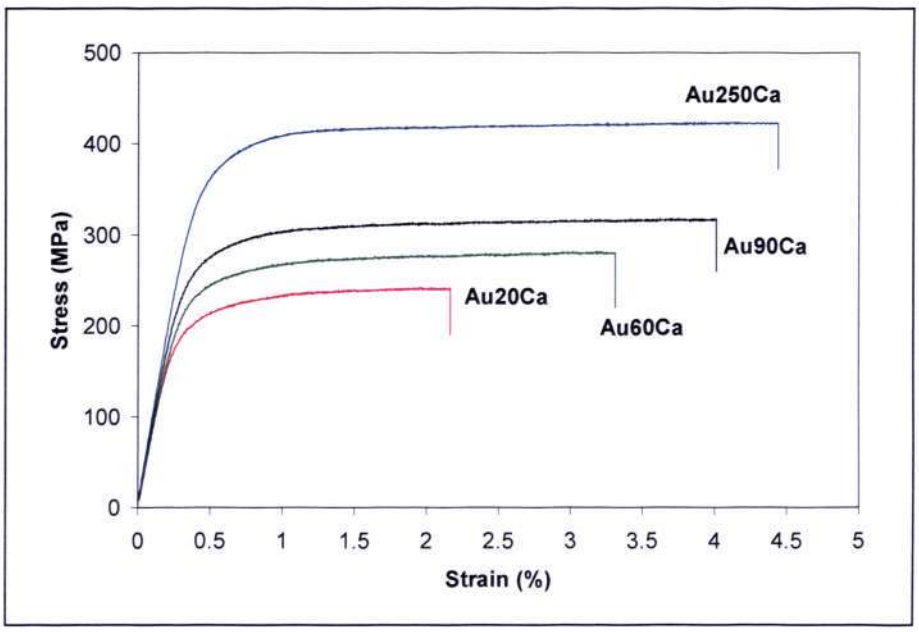

Figure 4-2 Engineering tensile stress strain curves of annealed Au wires, at various levels of Ca.

The effects of Ca are retained in the annealed wires, i.e. Ca increases the strength and ductility of Au wires concurrently. With this concomitant improvement, toughness (area under the curve) is invariably enhanced. The percentage of toughness increment, comparing Au20Ca and Au250Ca, are 127% and 277% for as-drawn and annealed wires, respectively. The values of ductility, strength and the percentage of improvement for the as-drawn and annealed wires are presented in Table 4-3. It can be seen that in the as-drawn state, Au250Ca has 69% and 32% higher ductility and strength than those of Au20Ca. Furthermore, after annealing at 500 ^{o}C, the level of increment between Au20Ca and Au250Ca for ductility and strength has gone up to 96% and 60% respectively. The percentage of improvement is remarkable, considering that the difference of Ca is only in the ppm level. These levels of enhancement are more impressive than those from other similar studies (e.g., Song, 2005; Zhao, 2006). For example, by adding 10% zinc in Cu, Zhao et al. has increased the ductility and strength over pure Cu by ~ 40% and 55% respectively (Zhao, 2006).

Obviously, we can further increase the ductility of these wires by annealing, but it comes at the expenses of strength. As mentioned, the improvement of properties is greater for the annealed wires (Table 4-3). Some of the properties e.g. uniform elongations are discussed in greater details in section 5.6.1. It was suggested that this phenomenon be possibly caused by Ca due to its effectiveness of inhibiting grain growth (Herklotz, 2001). The GS of Au20Ca is ~100 nm larger than the Au250Ca in the as-drawn state whereas it is ~1 μm larger in the annealed state (Kulicke, 2005). The effect of GS could dominate over other factors; therefore analysis of the mechanism is focused on

the as-drawn wires only.

Table 4-3 Tensile properties of the Au wire at room temperature

Properties	Au5N	Au20Ca	Au60Ca	Au90Ca	Au250Ca	Improvement from Au20Ca to Au250Ca (%)
As drawn						
Tensile strength (MPa)	98.64 ± 1.14	421.29 ± 1.54	450.07 ± 0.98	500.15 ± 1.12	556.30 ± 0.97	32
Percentage elongation (%)	3.51 ± 0.08	1.60 ± 0.15	2.10 ± 0.05	2.40 ± 0.05	2.70 ± 0.10	69
Uniform elongation (%)	3.51 ± 0.12	1.60 ± 0.08	2.10 ± 0.04	2.10 ± 0.10	2.10 ± 0.09	31
Annealing at 500°C						
Tensile strength (MPa)	N. A.	237.72 ± 0.80	279.38 ± 0.62	314.75 ± 0.54	379.95 ± 0.74	60
Percentage elongation (%)	N. A.	2.20 ± 0.18	3.30 ± 0.20	4.05 ± 0.04	4.30 ± 0.05	96

Compared to other studies, the absolute values of the percentage of elongation-to-failure (EL) reported here is not high. For example, EL of FG Cu ranges between 1- 7% (Lu, 2001b), for Cu having the GS between 10 nm- 100 nm. For Ni, EL is generally between 1- 10%, and can be tailored to reach as high as 50%, with a GS distribution of 100 nm to 8 μm (Zhao, 2008). However, the EL of FG materials is typically at ~2% (Koch, 1999). It is not meaningful to compare the absolute value of EL, since the sample used here is vastly different from most studies conducted in similar areas, especially in terms of materials, sample shape, sample size and test gauge length. For instance, most studies used standard dog-bone shape specimen, which can not be realized for fine wires. In this work, wire diameters used are relatively thin (0.025 mm) and are tested at long gauge length of 250 mm. Most other studies have much thicker/ bigger diameter samples of ~ 0.15 mm- 5 mm, especially for SPD samples. Commonly used gauge length is also

much shorter than our case, which is ~ 5 mm to 18 mm (Zhao, 2006; Hayes, 2004). In a paper dedicated to study the effect of specimen dimension on tensile properties of UFG/ NC metals, Zhao et al. have concluded that EL increases with increasing thickness or decreasing gauge length. Specimen with thinner diameter or thickness shall be susceptible to instability and premature failure, while the effect of gauge length originates from the definition for strain (Zhao, 2008; Li, 2004). Therefore both the sample diameter and gauge length work against higher EL in our case. Instead, the high percentage improvement induced with such low level of doping is the focus of this work. It is intriguing that the addition of Ca can bring about both higher ductility and strength at the same time, while the two properties are in general trade-off properties. The results from this study also highlight the importance of purity control in the study of UFG/ NC materials, as very low ppm level of dopant could give major impact on their properties.

All the above mentioned tests were conducted at a fixed strain rate of 0.017 s^{-1} (1 inch/minute). Subsequently, to understand the effect of Ca on tensile properties under various strain rates, tests were carried out at five different strain rates. The common ranges for strain rate testing are between 10^{-3} to 10^{-1} (static) and 10 to 10^{3} (dynamic). Due to equipment constraint, the highest strain rate that we can use is 10^{-1}. The strain rates used are within the range of 10^{-3} to 10^{-1}, which are 0.1, 0.017, 0.01, 0.005 and 0.001 s^{-1} respectively. The results of tensile testing, i.e. 0.2% offset yield strength (σ_y), tensile strength (σ_{TS}), EL are listed in Table 4-4, and plotted in Fig. 4-3 to Fig. 4-5, where standard deviations are omitted to avoid confusion. The beneficial effects of Ca addition on Au wires are very clear and consistent throughout the five strain rates used.

Table 4-4 Room temperature tensile properties of Au wires

Au wires	Strain rate (s^{-1})	σ_y (MPa)	σ_{TS} (MPa)	EL (%)
Au20Ca	0.1	422.33±2.63	437.16±2.62	1.5±0.15
	0.017	390.85±0.64	426.29±1.01	1.6±0.15
	0.01	390.87±1.06	421.67±4.58	1.6±0.2
	0.005	388.17±0.81	419.86±1.21	1.3±0.15
	0.001	382.06±1	405.57±3.63	1±0.1
Au60Ca	0.1	449.39±0.78	466.17±0.55	2.2±0.05
	0.017	415.53±0.33	456.07±0.41	2.1±0.05
	0.01	414.45±0.63	455.47±0.4	2.2±0.05
	0.005	411.63±0.53	451.48±0.32	2.1±0.05
	0.001	405.53±0.96	440.78±1.83	1.9±0.2
Au90Ca	0.1	496.99±0.49	517.27±0.3	2.4±0.1
	0.017	462.02±0.77	504.15±0.31	2.4±0.05
	0.01	461.2±1.09	504.25±0.3	2.4±0.05
	0.005	458.06±0.99	498.96±0.41	2.3±0.05
	0.001	452.03±0.67	489.66±0.42	2.3±0.05
Au250Ca	0.1	557.12±0.56	581.10±0.46	2.6±0.20
	0.017	534.02±0.43	557.30±0.53	2.6±0.10
	0.01	536.2±1.30	556.25±0.65	2.6±0.05
	0.005	528.46±0.59	549.32±0.47	2.5±0.15
	0.001	498.73±0.62	540.36±0.42	2.5±0.05

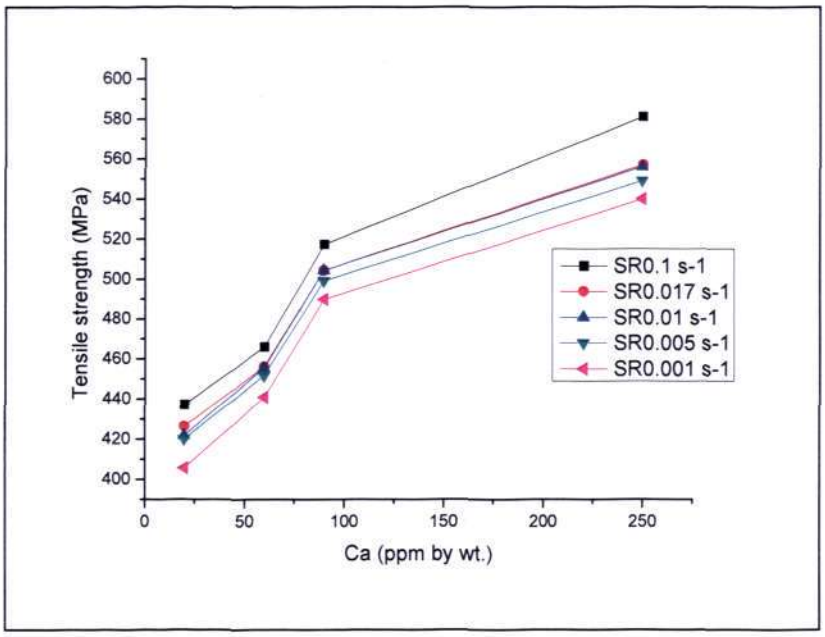

Figure 4-3 Tensile strength of Au wires as a function of Ca level at different strain rates.

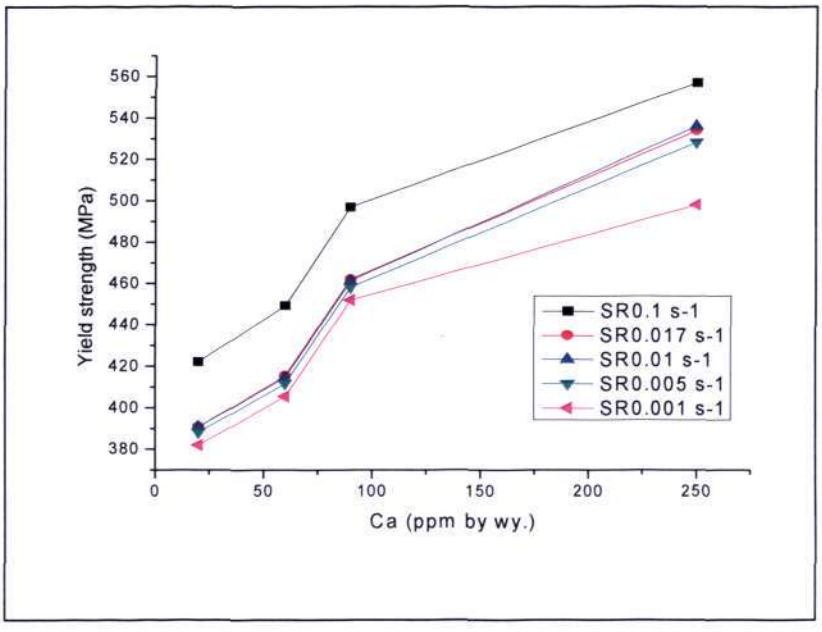

Figure 4-4 Yield strength of Au wires as a function of Ca level at different strain rates.

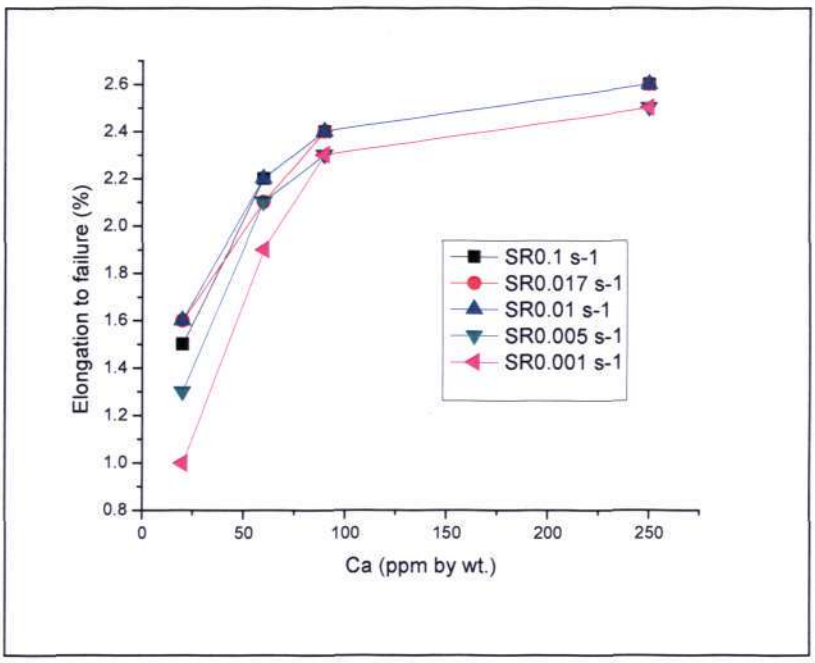

Figure 4-5 Elongation to failure of Au wires as a function of Ca level at different strain rates.

Strength is observed to be higher at higher strain rate and vice versa. It is clear that strain rate has an obvious impact on the σ_y and σ_{TS} of Au wires. Strength is always the highest for the fastest strain rate used (0.1 s^{-1}) and the lowest for the slowest strain rate used (0.001 s^{-1}), for Au wires at all Ca levels. This is consistent with numerous studies conducted on UFG/ NC face-centered cubic (FCC) metals (Torre, 2002), which their behavior deviates from the strain rate insensitive behavior of bulk CG FCC metals. Ductility (EL), on the other hand, seems to have weaker dependency on the strain rate. The variation of EL at various strain rate is high, still, there seems to be a trend that EL is the lowest when tested at the slowest strain rate. The trend is clearer only for Au20Ca. Whether ductility of UFG/NC metals should decrease or increase with strain rate is more

controversial. For example, Lu et al. reported that EL for electrodeposited NC Cu (GS ~ 30 nm) was ~ 25% larger when the strain rate was increased from ~ 10^{-6} to 10^{3} s^{-1}. They suggested that the behavior may originate from the change in the fracture mechanism (Lu, 2001a). However, the opposite was observed by Torre et al. with NC nickel, and ductility was found to decrease as the strain rate was raised from 10^{-5} to 10^{-2} s^{-1} (Torre, 2002).

4.3 Creep Performances of Au wires

High temperature performance of Au wires is important for certain applications such as automobile electronics. Devices are required to operate safely with high reliability over a long period, even under harsh working conditions, such as high temperatures and high humidity conditions enveloping an engine, which is peculiar to automobiles (Gallo, 2004). The requirement for Au wires is mainly from the reliability and resistivity aspects, also strong mechanical properties which can be extended into high temperature regime are needed. In this work, creep test conducted at low stress levels and high temperature (typically > 0.4-0.5T_m, where T_m is the melting point) is employed for the determination of high temperature properties of Au wires (Courtney, 2000). The main objective is to determine the effect of Ca on high temperature mechanical properties of Au wires.

For real life application, Au wires are usually doped at low doping level, with a mixture of various dopants (Kulicke, 2005). Because creep test are concerned with the actual performance of the Au wires, only wires with dopant concentration of < 100 ppm

are considered. Also, only two wires of extreme conditions are selected, which are Au20Ca and Au90Ca. Following the criteria for creep test, the force was selected to be lower than the 0.2% yield strength of the weaker Au20Ca at 513 K; And the temperatures are chosen to be lower than ~700 K (which is $0.4T_m$). Fig. 4-6 shows typical creep responses of Au wires, deformed with stress of 88 MPa and at temperature of 513 K. The creep curves exhibit a primary transient period, which then settle into steady state. The change of creep rate as a function of strain is also followed, as shown in Fig. 4-7. It can be seen that the strain rate has gone into a steady state and stabilized as strain proceeds, signifying that the creep rate attained is the minimum creep rate.

More than 70% of the time, the creep tests stopped before 3000 minutes, and mostly at the EL of < 1%. The low EL is expected, as it is known that high temperature EL of wires is lower than their room temperature EL, which is ~ 2% for our case (Kulicke, 2005). The creep rates are extracted from the time range of 1500-2500 min, where steady state creep rate has been achieved. It is obvious that Au20Ca has significantly higher slope, thus higher creep rate (%/min), than Au90Ca. The creep rates of Au20Ca and Au90Ca were collected under two loads and three temperatures, as shown in Table 4-5. Each experimental value corresponds to three data points, with a standard deviation between 0.1 %/min – 1 %/min. It can be seen that the creep rate of Au90Ca is consistently lower than Au20Ca, and the disparity ranges between 4 to 6 times. Considering that the dopant concentration only differs by 70 ppm, the retardation effect is quite significant. As a comparison, creep rate was reduced by 0.5-1 order of magnitude with 700 ppm (by weight) of boron added into NC nickel (Yin, 2001). Also, the creep

rates are always higher when the temperatures or stress levels are raised. It is concluded that Ca can retard the creep rate of the Au wires effectively. This shows that Ca has beneficial effects on both the room temperature and high temperature mechanical properties of Au wires, both of which are critical for wire applications.

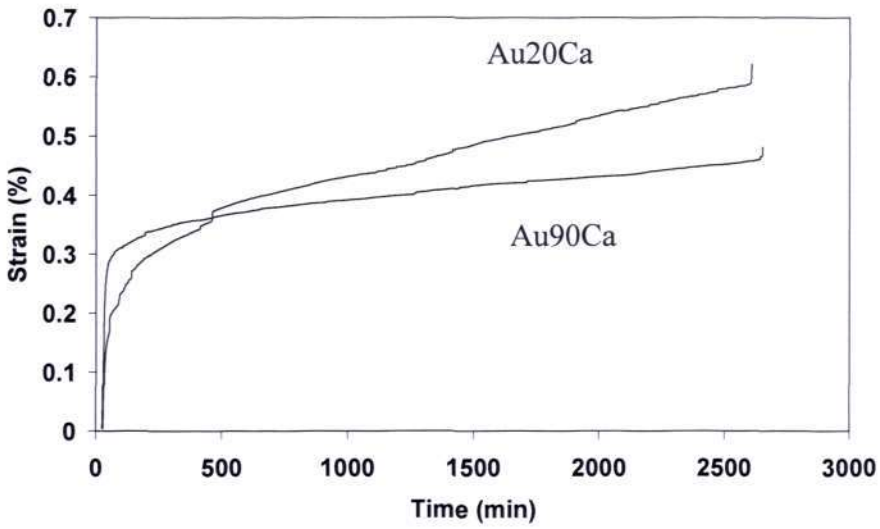

Figure 4-6 Typical creep curves of the Au wires deformed at 88 MPa, at 513 K.

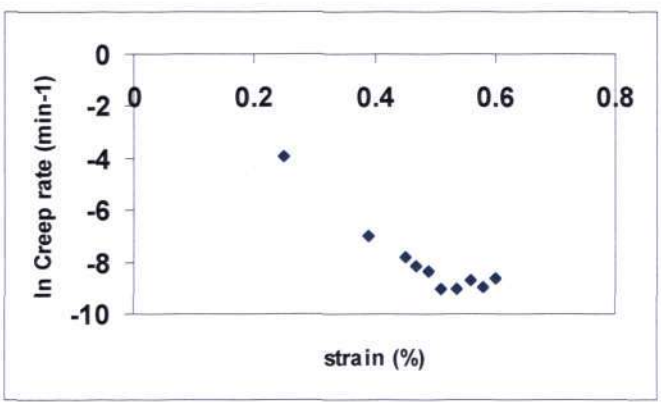

Figure 4-7 Creep data of Au20Ca plotted versus strain showing the minimum strain rate corresponds to steady-state creep.

Table 4-5 Creep rates of Au20Ca and Au90Ca at different stresses and temperatures, with standard deviations ranging between 0.1-1 %/min.

	Creep rate (%/min)	
	Stress at 67 MPa	**Stress at 88 MPa**
Au20Ca at 493 K	3.1	6.1
Au20Ca at 503 K	5.4	10
Au20Ca at 513 K	6.3	11.2
Au90Ca at 493 K	0.75	1.28
Au90Ca at 503 K	1.33	1.5
Au90Ca at 513 K	1.73	2.4

To further quantify and compare the creep behavior of the two samples, the general creep equation is used (Wakai, 1997):

$$\frac{d\varepsilon}{dt} = A\left(\frac{\sigma^n}{GS^p}\right)\exp\left(\frac{-Q}{RT}\right) \qquad (4\text{-}1)$$

where A is a constant determined by the slowest diffusing species along the most rapid diffusion path, σ is the applied stress, n is the stress exponent, GS is the grain size, p is the inverse GS exponent, Q is the activation energy and T is the temperature. Besides the creep rate, three parameters were also extracted from this set of creep data, namely the stress exponent, the grain size exponent and activation energy. As creep tests are very time consuming (each sample takes 2 days), we have limited data points for some of the derivations. For example, we have only two data points for the determination of stress exponent of Au20Ca at 493 K. This, however, is compensated by similar data gathered at

503 K and 513 K. These derived parameters are used to give a hint of the possible creep mechanism that could have taken place.

First, the data on creep rate as a function of the applied stress gives the stress exponent, n. Fig. 4-8 shows the creep data, plotted as steady state creep rate versus stress on double logarithmic scales. The slopes of the curves correspond to n, which are ~2 for Au20Ca and ~1 for Au90Ca at all three temperatures used (493 K, 503 K and 513 K). Diffusional creep has a linear dependence on stress, and has n value of 1. The n value obtained here shows that the creep in Ca-doped Au wires is sensitive to dislocation glide as well as diffusion, but is not as heavily dislocation-dependent as in the case of power law creep which has n ~ 3-8 (Courtney, 2000).

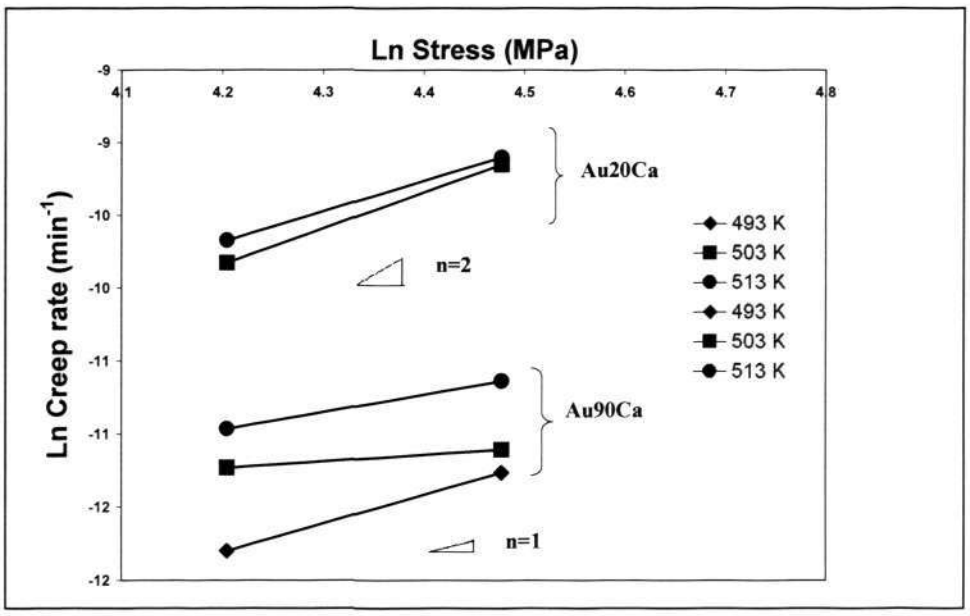

Figure 4-8 Creep rate vs. applied stress of Au20Ca and Au90Ca, which the slopes represent stress exponent, n.

Second, the activation energies (Q) of the creep process are derived from the Arhenius plot of creep rate versus reciprocal of temperature. The values of Q are shown in Fig. 4-9. It is expected that the Q obtained under the lower stress condition would be higher. For Au20Ca, the range is between 0.66-0.76 eV; For Au90Ca, the Q values are between 0.68-0.9 eV. The Q value of the GB diffusion is normally taken as half of the Q for lattice self-diffusion in conventional CG metals (1.76 eV for Au) (Gupta, 1975). It can be observed that the Q values obtained are comparable to the Q required in GB diffusion (Q_{gb}= 0.88 eV). The higher activation energy when more Ca is present correlates well with the slower creep rate observed on Au90Ca.

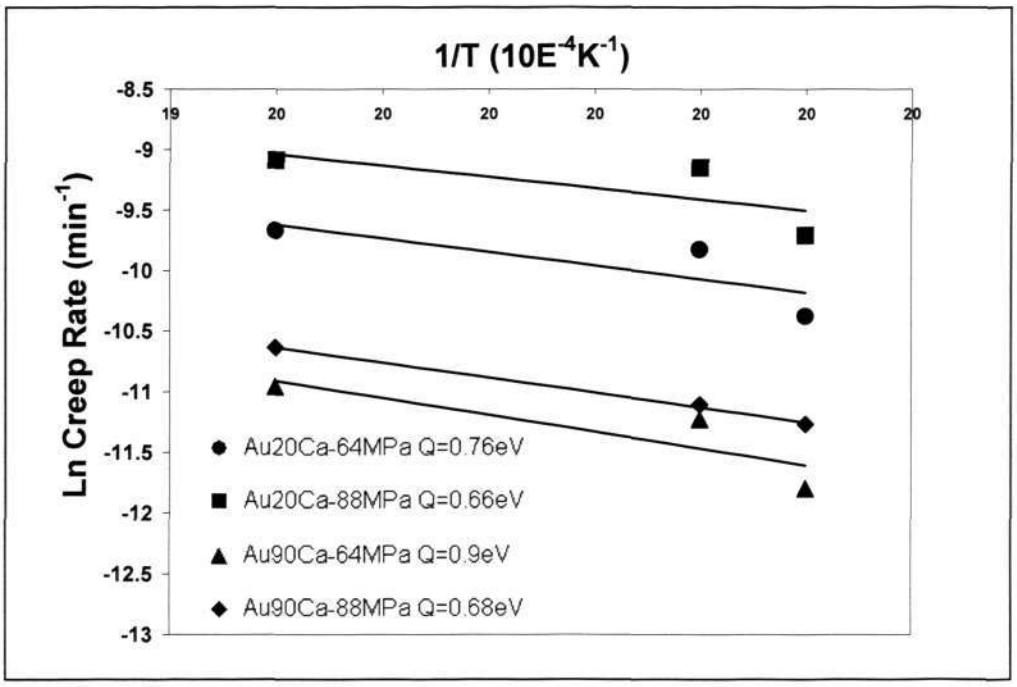

Figure 4-9 Arhenius plot of creep rate vs. reciprocal temperature of Au20Ca and Au90Ca, where the slopes represent the activation energy (Q).

Third, for the determination of the GS exponent p, the GS of the samples is measured with TEM. The average GS for Au20Ca and Au90Ca are 219 nm and 147 nm respectively, which we will discuss in detail in Chapter 5. With the average GS, the creep rate is then plotted wrt GS, to give the p value (Fig. 4-10). The GS exponent, p, is found to be ~3 at 67 MPa and ~4 at 88 MPa, which correspond to Coble creep (Courtney, 2000). The temperatures used are below the recrystallization temperatures of both Au20Ca and Au90Ca, which was determined using differential scanning calorimeter to be ~ 613 K and 633 K respectively (Cheo, 2004). Therefore we do not expect significant grain growth to occur during the creep test.

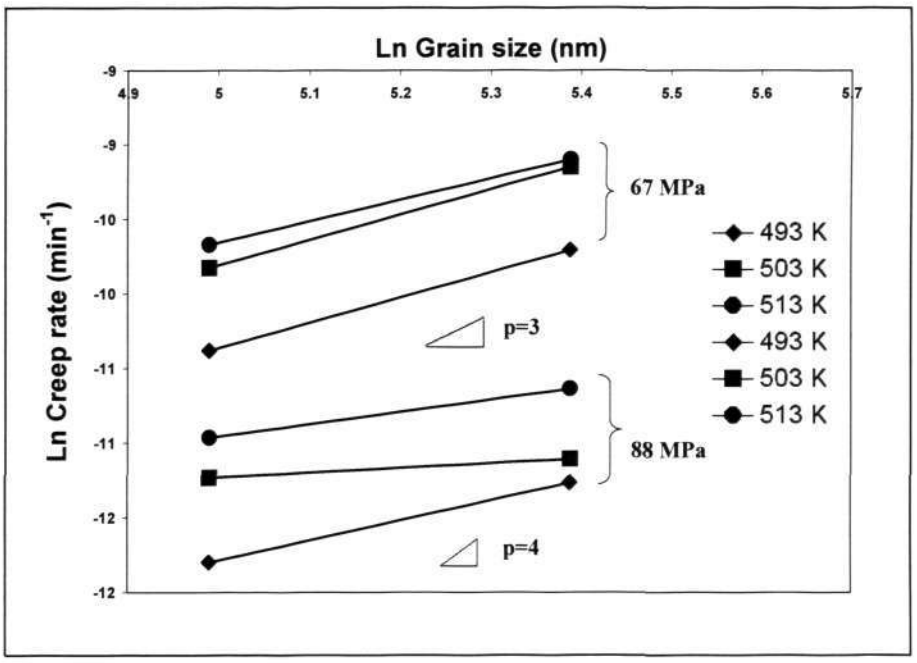

Figure 4-10 Creep rate vs. grain size of Au20Ca and Au90Ca at two levels of applied stress, where the slopes represent grain size exponent, p.

The value of p=3-4 suggests a GB diffusion controlled creep mechanism, while n=1-2 implies a dislocation-related mechanism. Also, the Q value obtained is close to Q for GB diffusion in CG Au. This combination of experimental values was also observed in other systems, especially in superplastic materials (Cho, 2001) and FG materials (Yin, 2005; Cai, 2001), where creep operates through GB sliding or GB diffusion. The commonality among the studies is that GB has a much more important role in UFG and NC metals when deformation occurs at lower temperature than CG metals. With the p, n and Q values observed, the likely creep mechanism in Au wires under present study could be GB sliding which is accommodated by GB diffusion. These findings elucidate the important role of GB in creep deformation in FG metals, observable at much lower temperatures than their CG counterpart. It is known that materials with elongated grain structure which are parallel to the major stress axis are less prone to GB sliding (Hertzberg, 1996). However this study shows that Au wires with such structures are also prone to GB sliding under high temperature, probably due to the fine grains.

As the dominating creep mechanism is likely to be GB sliding which is accommodated by GB diffusion, it is postulated that most Ca could have segregated to the GB to interfere with the deformation process. This postulation is in agreement with other similar studies (Cho, 2001; Yin, 2001). Also, the mechanical properties such as room temperature tensile properties and creep properties of FG metals are known to be very sensitive to dopants that reside at the GB (Yin, 2005). This suggests that the dopants may have segregated to the GB to manifest the effects. The form and detection of dopants will be further discussed in Chapter 5.

4.4 Hall-Petch Properties of Au wires

In previous section, the results imply that GB segregation of Ca in Au wires might have occurred. In this section, we study the Hall-Petch behaviour of Au wires, which can provide more information on the GB properties. On the basis of the dislocation pile-up mechanism for the plastic deformation of CG materials, the yield strength of a polycrystalline metal is expected to increase with reducing GS:

$$\sigma_y = \sigma_o + kGS^{-1/2} \qquad (4\text{-}2)$$

where σ_y is the yield strength, GS is the grain size and σ_o is the lattice resistance. The Hall-Petch coefficient, k, can be regarded as a measure of the difficulty of slip transmittal across GB. A previous study had commented that k depends on the way the dislocation structure builds up during the deformation, and its meaning is not straightforward. Still in general, the k value is typically viewed as a "locking parameter", which measures relative hardening contribution of GB (Hertzberg, 1996), or as GB parameter that serves as obstacles to the propagation of deformation (Lu, 2001b). The values of σ_o in the as-drawn state are derived to be 328.38 MPa and 330.09 MPa for Au90Ca and Au20Ca respectively, which are almost identical. To determine k, GS of the samples in the as-drawn and various annealed states are measured with SEM images. The GS of as-drawn wires are too fine to be distinguished with SEM, and are obtained from TEM (Chapter 5). Representative SEM images from each condition are presented in Fig. 4-11.

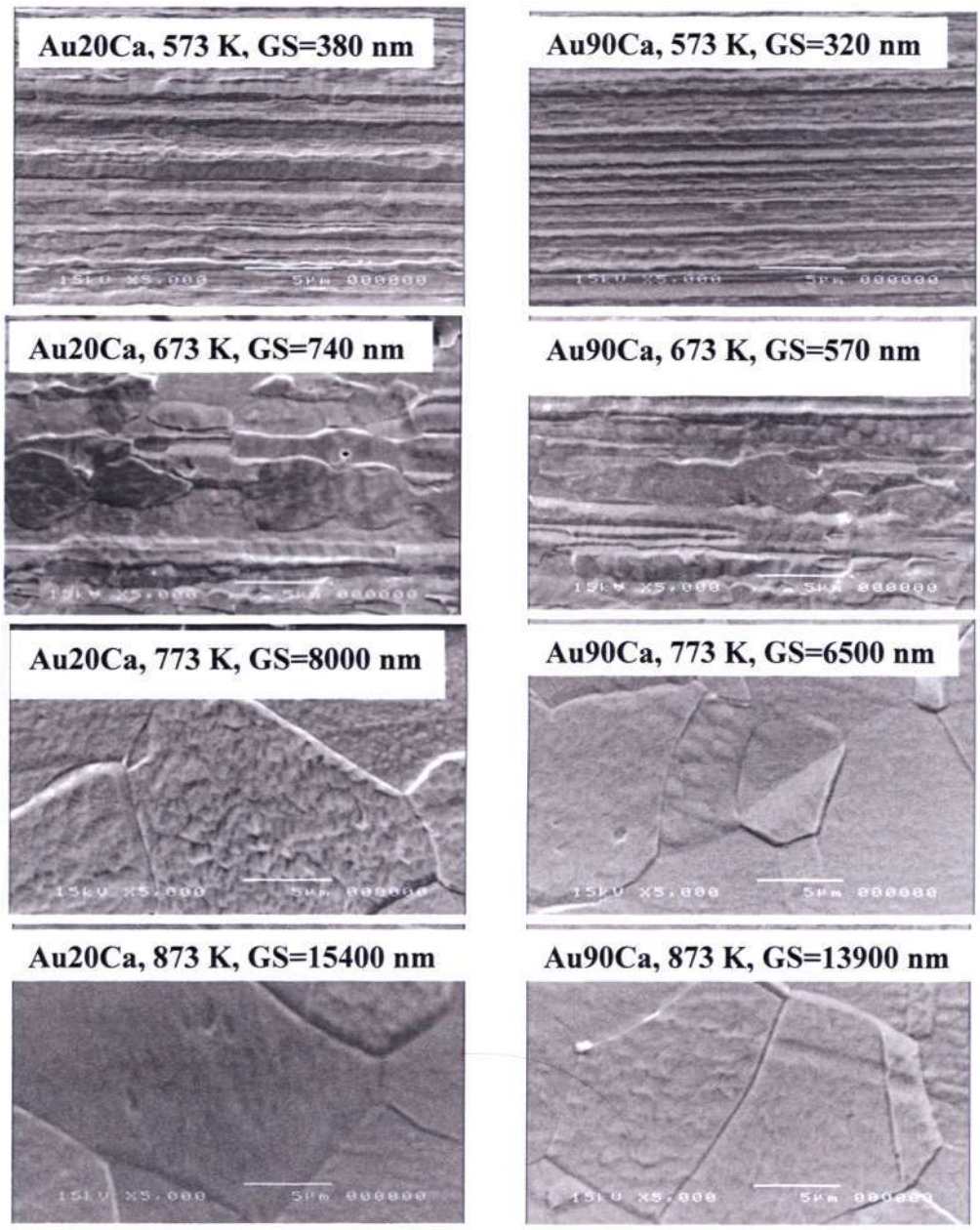

Figure 4-11 Representative SEM images of Au20Ca and Au90Ca, annealed at 573 K, 673 K, 773 K and 873 K respectively. The average grain sizes, GS, are indicated.

The slope of σ_y versus $GS^{-1/2}$ gives k, which is the Hall-Petch coefficient. Fig. 4-12 shows that the k values for Au wires are 0.06 MPa• $m^{1/2}$ and 0.02 MPa• $m^{1/2}$ for Au90Ca and Au20Ca respectively. The k value of Au film reported by Emery et al. is reproduced in Fig. 4-12, which is 0.25 MPa• $m^{1/2}$ (Emery, 2003). Since k represents the extent of GB strengthening, it seems that the GB strengthening effect is much more pronounced in Au films than Au wires. The k values of three FCC metals with micrometer GS range were summarized in Hansen's work. For aluminium, nickel and copper, the k values are 0.04 MPa• $m^{1/2}$, 0.16 MPa• $m^{1/2}$ and 0.14 MPa• $m^{1/2}$ respectively (Hansen, 2004). The values are comparable to the k found for Au wires and Au films. The difference of k between Au20Ca and Au90Ca is not very significant, however, we should bear in mind that the difference in the doping level is only 70 ppm. GB segregation has been reported to be responsible for the difference in k value. For example, the change in k was attributed to constitutional disordering of the GB that arises from co-segregation of nickel and boron in Ni_3Al. It is known that GB segregants can modify GB structures to encourage dislocation generation, which could lead to dislocation accumulation along GB and possibly a Hall-Petch strengthening effect (Baker, 1991). The k values obtained therefore support the postulation that Ca could have segregated to the GB in Au wires, as deduced in the previous section.

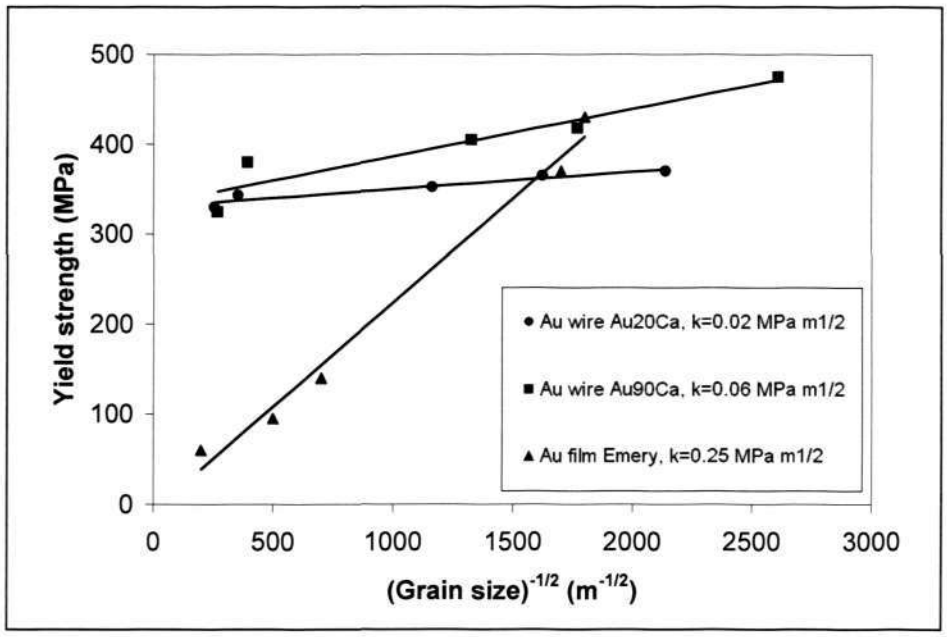

Figure 4-12 Yield strength as a function of (grain size)-1/2 for Au wire from this study; And for Au film from Emery's study.

One of the issues in debate has been whether the Hall-Petch relation breaks down at a critical GS (Dao, 2007), which some termed this phenomenon as 'inverse Hall-Petch Law', or 'the strongest GS (Lu, 2001b). This observation was first reported by Birringer and co workers (Birringer, 1984), that various experiments have pointed to a departure from the linear relation when GS decreased to the nanometer range. As GS further decreases, the Hall-Petch plot could even exhibit a negative slope (Nieh, 1991). However, whether there is a true 'strongest GS' has not been fully confirmed experimentally, but mostly predicted by molecular dynamics (MD) simulation. Right now it is fair to say that simulation (Van Swygenhoven, 2001), as well as limited experiments (Erb, 1995) have suggested that the critical GS for decreasing strength may be on the order of 5–15 nm.

Many mechanisms have been put forward to interpret the negative Hall-Petch slope, which mostly point to the migration of deformation mechanism.

In his work, Emery has suggested that Au film may deviate from Hall-Petch relation at GS significantly larger than other FG metals, which is ~ 500 nm (Emery, 2003). However, in our work, the yield strength of Au wires seems to obey Hall-Petch relationship down to GS of as fine as ~150 nm. Nieh et al. has attempted to estimate the critical GS at which inverse Hall-Petch phenomenon should take place (Nieh, 1991). They have estimated the critical GS for dislocation pile-up, below which decreases in strength with reducing GS could occur. His estimation was based on the equation:

$$l_c = \frac{3Gb}{\pi(1-\nu)3\sigma_{app}} \qquad (4\text{-}3)$$

where l_c is the critical GS, G is the shear modulus, b is the Burgers vector, v is the Poisson's ratio and σ_{app} is the applied stress. Taking σ_{app} to be ~ 450 MPa (Chew, 2006), the l_c for Au is estimated to be ~ 8-10 nm. To conclude, both the theoretical estimation suggested by Nieh and the experimental results obtained in this work do not agree with what has been suggested by Emery, that the critical GS of Au is at ~500 nm. This could also be attributed to the difference in texture (textured versus random) or grain shape (fibrous versus columnar). More work is needed to conclusively determine the critical GS of Au.

4.5 Chapter Summary

The beneficial effects of Ca on Au wires are summarized in this chapter, the results being suggestive that Ca has the tendency for GB segregation in Au wires to induce these effects.

1. The addition of Ca has the intriguing effect of progressively and consistently increasing both strength and ductility of Au wires. The improvement can be as high as 60% and 96% respectively, by comparing Au20Ca and Au250Ca. The effect has been demonstrated in as-drawn and annealed wires, at five different strain rates.
2. Ca is also shown to impede high temperature creep rate of Au wires by ~4 to 6 times. The stress exponent (1-2), activation energy (~ 06-0.9 eV) and grain size exponent (3-4) obtained all point to a GB diffusion mediated GB sliding creep mechanism. It is therefore postulated that Ca could have segregated to the GB to induce the retardation effect.
3. Hall-Petch coefficient is increased by the Ca addition, from 0.02 MPa• $m^{1/2}$ for Au20Ca to 0.06 MPa• $m^{1/2}$ for Au90Ca. This implies that Ca could have segregated to the GB to encourage dislocation generation and to strengthen the GB more effectively. Both the changes on creep and Hall-Petch behavior of Au wires as induced by Ca suggest that segregation of dopant to GB may have occurred.

In conclusion, Ca has beneficial effect on both the room temperature and high temperature mechanical properties of Au wires, which is important for bonding wire application. The impact of Ca on GB-related properties is also evident. Based on the results, it is postulated that segregation of Ca to GB is highly probable.

Chapter 5
Mechanisms of Ca-induced Dual Improvement in Au Wires

Previously we have summarized the unique and beneficial effects of Ca on Au wires in chapter 4. Ca consistently increases both strength and ductility of Au wires (dual improvement), an effect which is highly desirable. With the goal of establishing selection criteria for dopants to achieve similar effects, we present through a series of designed tests, a thorough investigation on the underlying mechanism for the dual improvement effect.

First we look at the microstructure of the Au wires, and their changes as a function of Ca content. Techniques used include optical microscopy, SEM (scanning electron microscopy), TEM (transmission electron microscopy), EBSD (electron back-scattered diffractometer), DSC (differential scanning calorimetry), XRD (X-ray diffractometer), EDX (energy dispersive X-ray spectroscopy) and EELS (Electron energy loss spectroscopy). We also access the strain rate sensitivity/ activation volume and strain hardening/uniform elongation of the Au wires, which is related to the major limiting factor of the ductility of UFG/ NC metals- plastic instability (Wang, 2004b). Based on the structures and properties observed, possible mechanisms, such as grain refinement, GB sliding, suppression of plastic instability, contribution of twin and texture induced plasticity are discussed.

5.1 The Form and Location of Ca in Au Wires

One question to be answered in this study is regarding the location and form of Ca dopants in Au wires. The phase diagram of Au-Ca shows a maximum solid solubility of 1.8 at% (0.36 wt %) at ~800°C, but the solid solubility of Ca in Au at room temperature is not known exactly (Massalski, 1986).

5.1.1 Microstructural Characterization

There is no second phase formation at all levels of Ca, up to Au250Ca. In Au500Ca, small patches of greyish second phases are observed in 2 mm Au rod, as shown in Fig. 5-1. If second phases are observed in Au rod, they will usually appear in the corresponding Au wires as well, typically at a finer size, as wire drawing could have broken down the second phase. In order not to miss out the second phase, these observations are done on 2 mm Au rod sample. Analysis with SEM/EDX shows that these second phases contain Ca (Fig. 5-2). The second phase form is probably intermetallic compound of Au and Ca. We therefore decide to drop Au500Ca, since second phase formation is not desirable in bonding wire. Bonding wires are required to have consistent mechanical and electrical properties throughout the wire strand. Second phase formation is basically non-uniform or agglomeration of dopant, and because the total dopant concentration have to be low in general, there could either be too much or too little dopants across the wire strand, if second phase forms (Stephan, 2005).

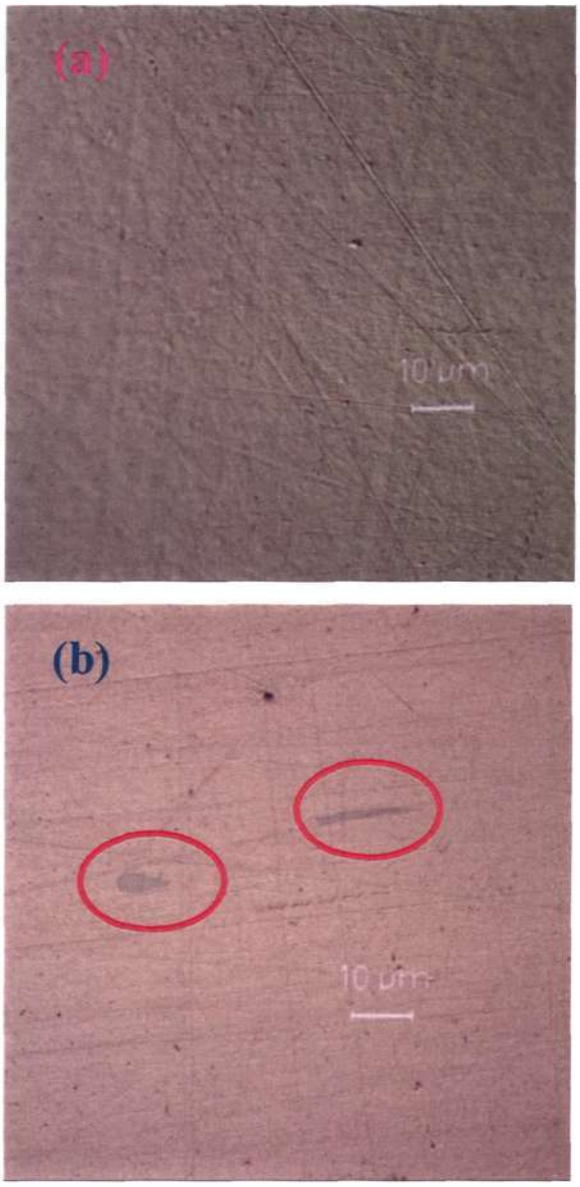

Figure 5-1 Optical micrograph on the cross-section of as-drawn 2 mm Au rod (a) Au250Ca, which no second phase is observed and (b) Au500Ca, with second phases.

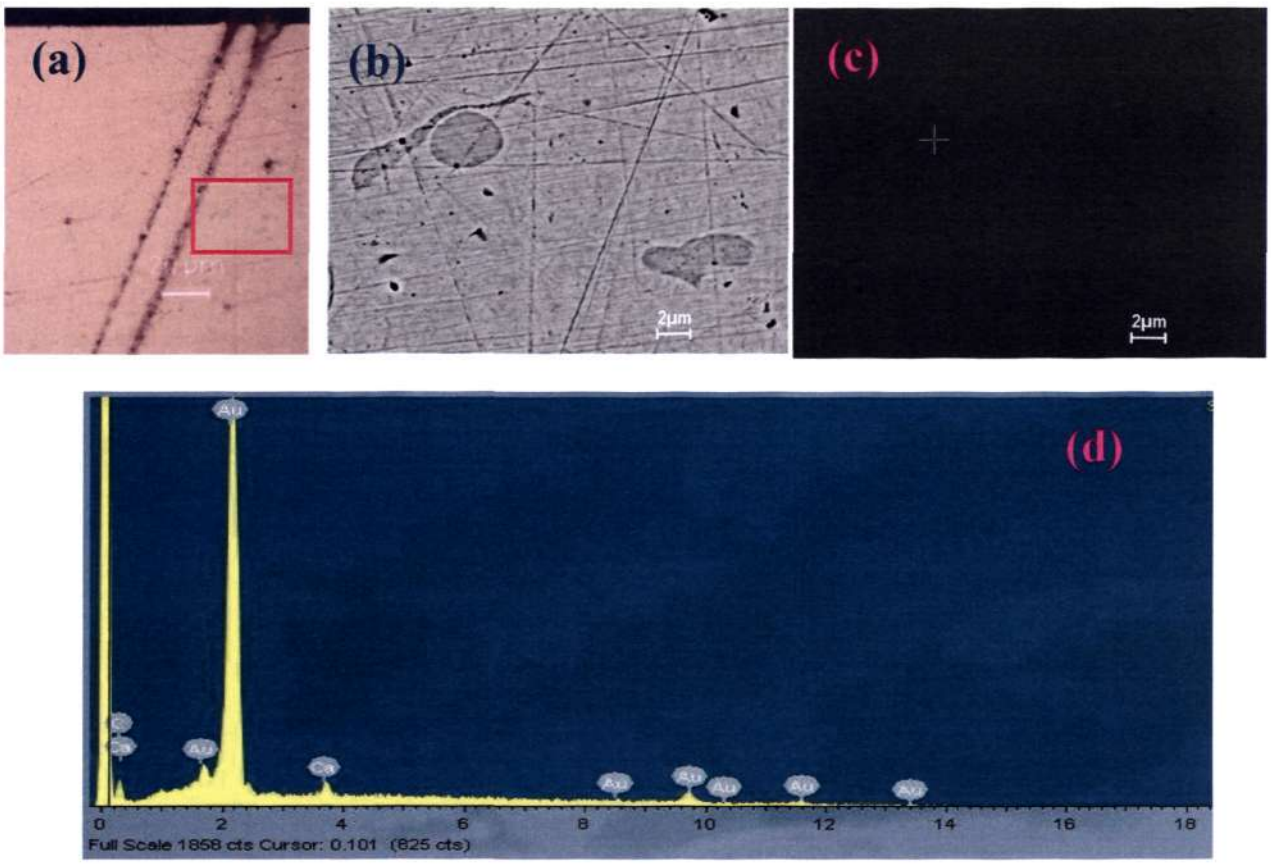

Figure 5-2 Microstructure analysis on Au500Ca Au rod (a) Optical micrograph which shows greyish second phase; (b) SEM micrograph zoom into the area enclosed by the red box in (a), viewed with back-scattered electrons; (c) SEM micrograph viewed with secondary electrons and (d) EDX analysis showing the presence of Ca peak.

Based on these observations, it is believed that Ca starts to form precipitation in Au wires at ~ 400 ppm (which is the actual composition of Au500Ca), even though the expected solid solubility limit at 800°C is about 3750 ppm. It was also reported in several publications that UFG/ NC materials have higher solubility with the presence of abundant boundaries (Liu, 2004; Yin, 2005). This means that the solid solubility of Ca in Au could be even lower in CG Au. Note that this boundary when solid solution ceases to occur is expected to vary with different processing conditions as well. It is interesting to note that,

the occurrence of second phase coincides with the point that the dual improvement comes to an end. At Au500Ca, ductility improvement saturates while the strength improvement persists (section 4.1). For both properties and microstructural consideration, subsequent study will focus only on wires with 250 ppm Ca and below.

Also, Au5N is not included in the comparison. This is mainly because of its vastly different condition from Ca-doped Au wires, in terms of their dopant concentration, GS and texture, which will be mentioned in subsequent sections 5.2 and 5.4. This complicates the identification of mechanism, as too many factors may contribute to the differences in properties. On top of that, Au5N is too soft and can not be subjected to many different conditions such as annealing and low speed tensile testing.

5.1.2 Elemental Analysis

To provide direct evidence for GB segregation, we have attempted to use EDX and EELS. The analysis was carried out on GB and SF, which are areas where Ca is proposed to segregate to (section 5.7). Sample chosen is Au250Ca, which is annealed at 600°C for 3 minutes. Also, the samples were deformed at the lowest possible strain rate (0.001 s^{-1}) and the highest possible testing temperature (250°C) to facilitate segregation of solute atoms onto the SF (called Suzuki segregation) and GB (Han, 2003). Fig. 5-3 shows one of the typical EDX analysis that we have performed. Ca was not detected, probably due to the low concentration, and the complicating presence of abundant GB and SF. Because EELS should provide better sensitivity for light elements, we have also

attempted to locate Ca with EELS. The dispersion of the spectrometer was set to 5 eV/ch, and to avoid zero loss peak, an offset of 280 eV was applied to the spectrometer drift tube. However, Ca is still not detected by this technique. Fig. 5-4 shows the EELS spectrum acquired from a region containing the boundary. The spectrum obtained at the boundary shows only the presence of C (peak edge at 300 eV) and Au (peak edge at 560 eV), both shifted by 20 eV. The reason why EELS has also failed to capture Ca is probably because there are lots of grain boundaries and stacking faults, therefore the probability of locating 'the right one' is also not high.

Direct chemical evidence for this type of segregation is generally lacking (especially to SF), because of the abundance of SF and difficulty of microanalysis (Murr, 1975). While only several investigators were able to directly identify the segregation (Kamino, 1992; Han, 2003; Mendis, 2004), most studies presented indirect identification. For example, changes in the width of an extended dislocation in a Cu–8 at. % Si alloy was inferred to be due to Suzuki segregation (Saka, 1983).

In conclusion, Ca is found to exist as solid solution in Au wires, and precipitates out when dopant concentration reaches 400 ppm. We are unable to identify the location of Ca solute exactly, even though creep test and study on Hall-Petch behaviour both suggest that Ca could have the tendency to segregate (Chapter 4). It is postulated that Ca concentrates along GB and SF, to induce an obvious effect on the mechanical properties of Au wires, as we will discuss again in section 5.7.

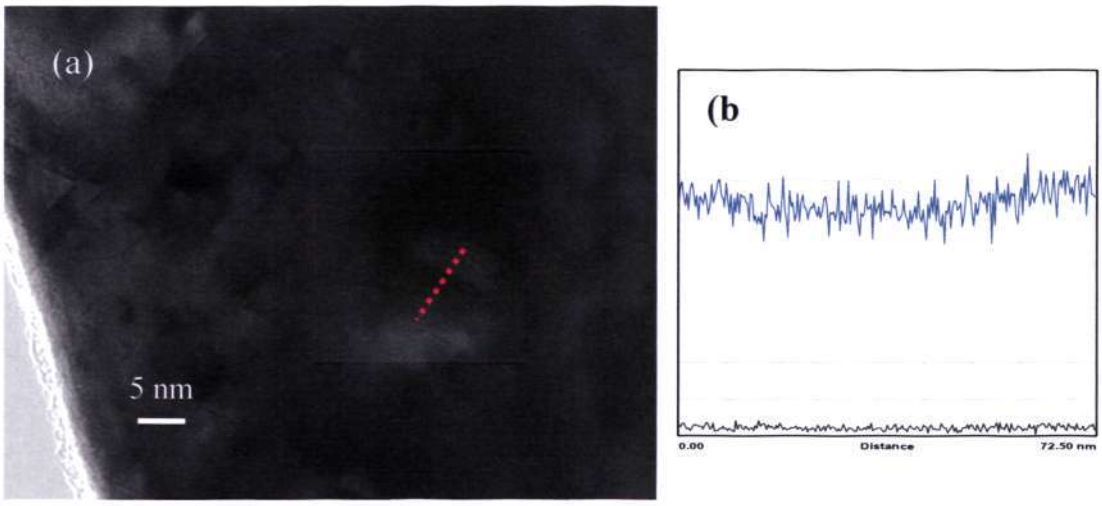

Figure 5-3 Typical EDX analysis on SF of Au wire, (a) Location of analysis and (b) EDX spectrum.

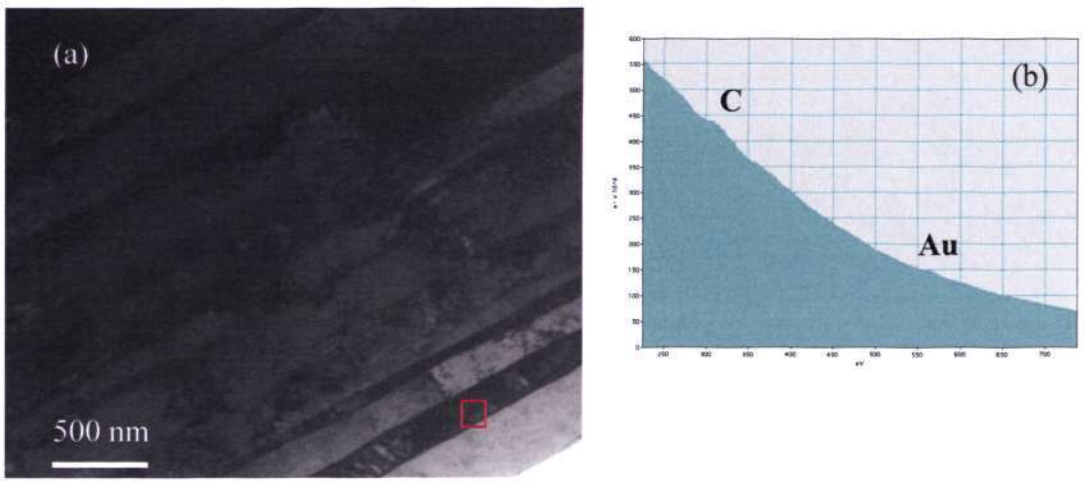

Figure 5-4 Typical EELS analysis on GB of Au wire, (a) Location of analysis and (b) EELS spectrum.

5.2 Microstructure Observations on Rods and Wires

It is a common practice in the wire bonding industry to observe the microstructure of wires in the longitudinal cross-section (Kulicke, 2005). Fig. 5-5 shows the longitudinal and transverse cross-section images of Au250Ca, in the form of 8mm Au rod and 25 μm wire. We did not study the transverse cross-section of Au wires with TEM, and have cited TEM studies of Au wires by Noguchi et al. (Noguchi, 2000) in Fig. 5-5c. The common observation is that first, the grains observed in the longitudinal cross-section appear to be elongated, while they look more equiaxed in the transverse cross-section. Second, the GS (denoted as d_s) in the longitudinal cross-section corresponds roughly to that observed from the transverse cross-section. From these observations, it is seen that a strand of 25 μm Au wire is made up of multiple bundles of Au fibers. These long grains are the product of the extensive, uni-directional plastic deformation- the drawing process. As shown in Fig. 5-5c, the long grains have two GS. One is the short side of the fiber (denoted as d_s), and another length is the long side of the grains (denoted as d_l). In this study, d_s is measured, following the convention used in the wire drawing industry. In fact, d_l of Au wires has not been reported before. This is probably because the fibers are too long to be captured under TEM, or the boundaries perpendicular to the drawing direction are not clearly defined. Noguchi et al. did not measure d_l but had suggested it to be ~ 5 μm.

One reason why d_s has been used throughout the wire bonding industry is that it has long shown good correlation with the strength of Au wires. In subsequent discussion, 'GS' refers to d_s measured from the longitudinal cross-section of the Au wires.

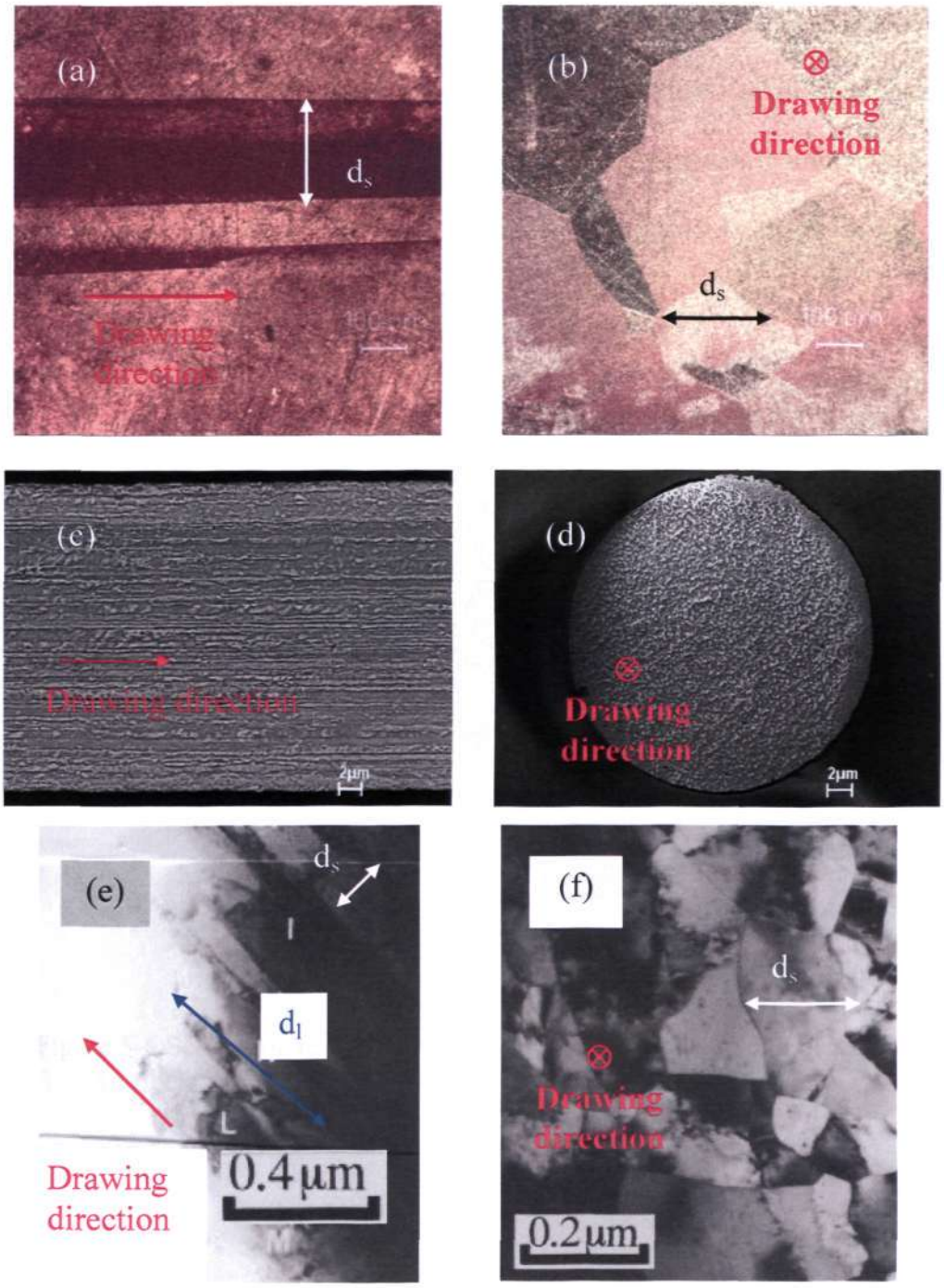

Figure 5-5 Images on (a) Longitudinal cross-section of Au250Ca, 8mm rod; (b) Transverse cross-section of Au250Ca, 8mm rod; (c) Longitudinal cross-section of Au250Ca, 25 μm wire; (d) Transverse cross-section of Au250Ca, 25 μm wire; (e) Longitudinal cross-section of ~ 25 μm Au wire under TEM and (f) Transverse cross-section of ~ 25 μm Au wire under TEM. (e) and (f) are taken from Noguchi, 2000.

Typical images of 25 μm Au wires are shown in Fig. 5-7. The wires are as-drawn 5N wires, Au20Ca and Au250Ca respectively. Pure 5N wires have larger grains of ~ 10 μm, and can be easily captured under both optical scope and SEM. On the other hand, the finer GB in Au20Ca and Au250Ca may not be accurately distinguished with these techniques. It can be seen that the grain structures of Au20Ca and Au250Ca do not appear to be very different, even when observed under SEM.

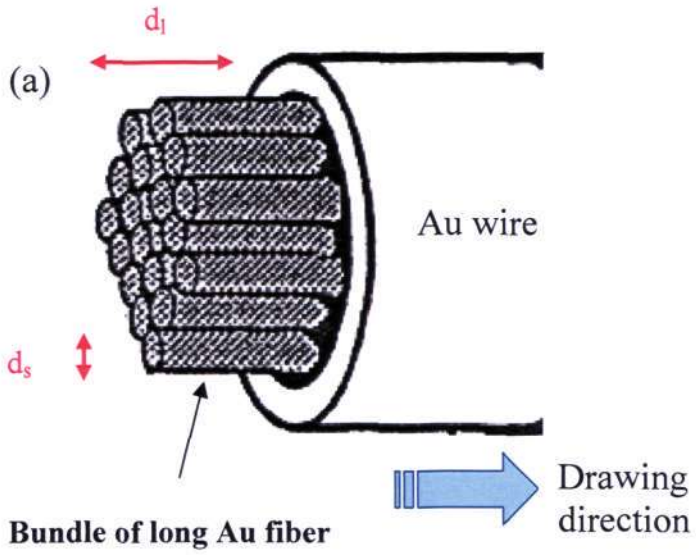

Figure 5-6 Schematic representation: Au wires are made up of a bundle of fine Au fibers.

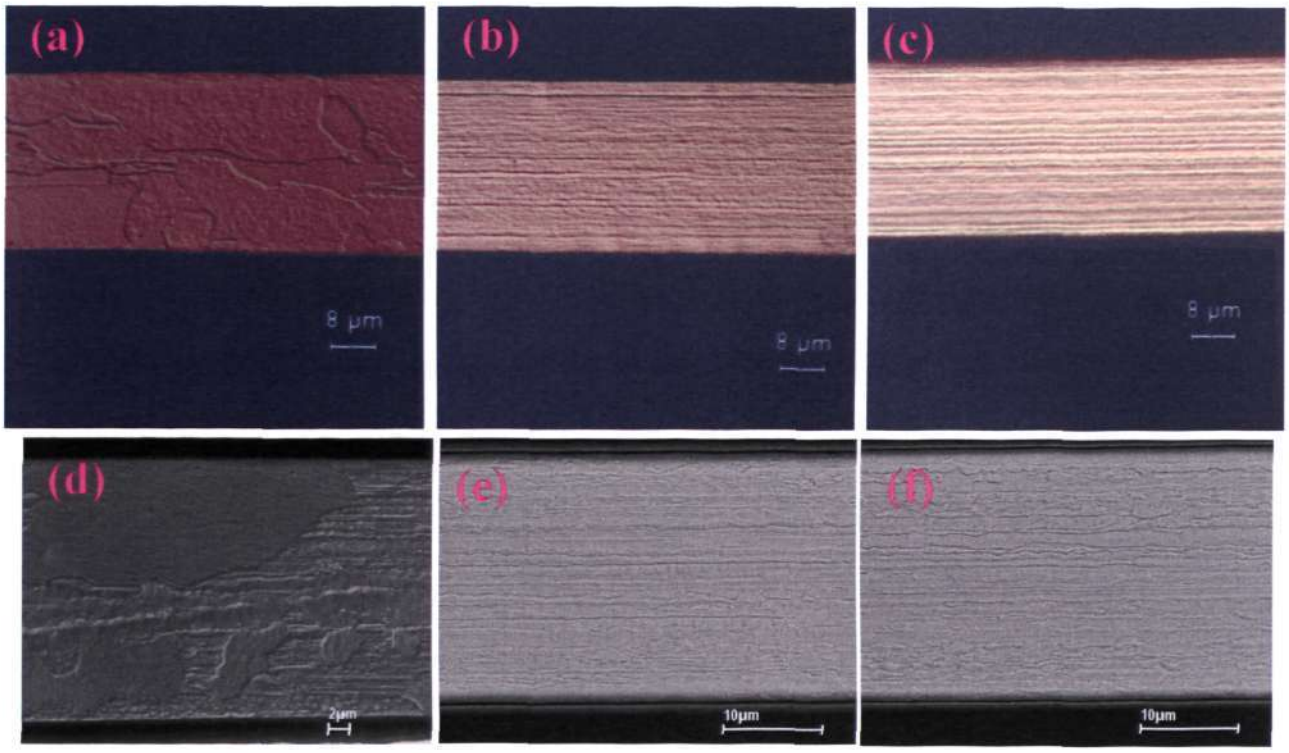

Figure 5-7 Grain structure of 25 µm Au wires in optical micrograph
(a) Au5N ; (b) Au20Ca ; (c) Au250Ca; And SEM micrograph of (d) Au5N ; (e) Au20Ca and (f) Au250Ca.

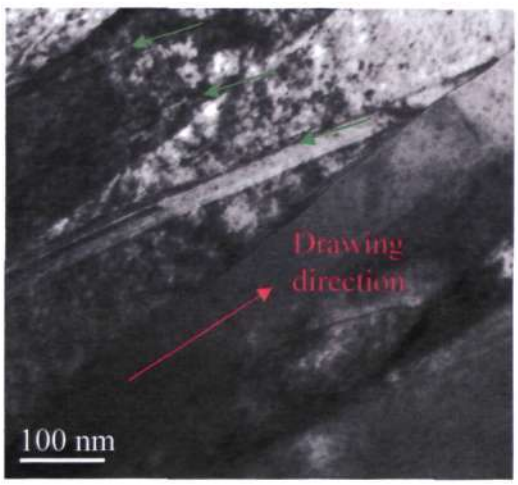

Figure 5-8 Typical brightfield TEM image of Au wires, after tensile deformation. The green arrows indicate twins.

Fig. 5-8 shows a typical brightfield TEM image of the as-drawn Au250Ca. The fine grains are clearly observed from the TEM. On top of that, fine features such as the existence of nano-twins are also observed in the TEM images. Probably because of the fine size, these twins are not observed in any of the SEM and optical images. To avoid missing these fine features, subsequent microstructure analysis will be focusing on TEM analysis only. Also, as described in Chapter 3, it is the intention to capture the structures from the tensile-deformed part of the wires. It is found that the microstructures before and after tensile deformation appear to be similar. The samples used are deformed after tensile test, as described in Chapter 3.

5.3 Microstructural Characterization with TEM

The initial reasoning for selecting Ca is both for its well-known strengthening effect and the postulation that Ca may reduce the stacking fault energy (SFE) of Au wires effectively, even at very low concentration. SFE of a material is important since it dictates many physical properties of the materials, especially mechanical properties as it has direct influence on the slip mode, deformation twinning etc. Therefore in this section, we start off with an investigation on SFE of Au wires. The GS and microstructure of the wires are presented subsequently.

5.3.1 Stacking Fault Energy of Au Wires

Alloying (in solid solution form) typically decreases SFE of the matrix materials.

The usual range of alloying study is from few percent up to as high as ~ 40 wt % (e.g. Nie, 1995; Engler, 2000), but there are also studies which focused on lower alloying concentration of as low as 0.2 wt % (Caballero, 1999; Rohatgi, 2001). The highest dopant level used in this study is 0.12 wt. %, which is on the low side among the studies that investigate the effects of dopant on SFE.

The mechanism behind the phenomenon is the segregation of dopant to stacking fault (SF), stabilizing SF and lowering SFE, as first pointed out by Suzuki. The absorption phenomenon can be treated in the same manner as at GB, and are expressed in terms of the Gibbs adsorption isotherm here:

$$\left(-\frac{\partial SFE}{\partial G_2}\right)_T = \Gamma_2 - \frac{x_2}{x_1}\Gamma_1 \qquad (5\text{-}1)$$

where x_2 and x_1 are the atom fraction of solute and solvent in the bulk phase, G_2 is the chemical potential of solute and Γ_2 and Γ_1 are the surface excess concentration of solute and solvent at the fault. For dilute solutions, where $\Gamma_2 > (x_2/x_1)\,\Gamma_1$, the adsorption isotherm reduces to:

$$\left(-\frac{\partial SFE}{\partial G_2}\right)_T = \Gamma_2 \qquad (5\text{-}2)$$

Eq. 5-2 shows that when solutes accumulate at the SF, the equilibrium SFE decreases (Hirth, 1986). Solutes that make the face-centered cubic (FCC) solvent less

stable against a transition to hexagonal close packed (HCP) structure would be expected to accumulate in the SF, which is a thin strip of HCP material, and lower its energy. The reason for that is on alloying, the free energy of the solid solution is increased, i. e. the stability of the solid solution against other phases has decreased, and hence can tolerate more mis-stacking (Cahn, 1996). Some authors commented that the driving force for Suzuki segregation has its origin in the difference in chemical free energies between the planar defect and the matrix, and is different from Cottrell segregation, where the driving force is the reduction of the solute atom misfit energy (Mendis, 2004). The theory as first proposed by Suzuki is fairly complete, however direct chemical evidence is scarce. (Murr, 1975). Mostly, the effect manifests itself as a change in the stacking fault width (SFW), which is one of the methods for SFE estimation (Hirth, 1986; Courtney, 2000), and is employed in this work.

To observe SF of the wires, high-resolution TEM (HRTEM) images from one of the grains were taken from the <110> zone axis, as shown in Fig. 5-9. The imaging of crystal defects is highly dependent on the orientation of the crystal with respect to the beam. Therefore, great care was taken to ensure that all the HRTEM images for this purpose are taken in <110> zone axis. Since there are also several [110] directions for the same zone axis, sample size is increased to obtain an overall, typical reading. For every condition, the average sample size is 3 wires, and approximately ten grains were inspected per sample.

The SF normally appears as two fold structures ('V' or inverted 'V'). These kinds of multiple folds SF have also been observed in other studies conducted on UFG/ NC metals, while the reason for these formations is unclear at the moment (Liao, 2004a; Wu, 2006a). The majority of SF planes were determined to be $(1\,\bar{1}\,\bar{1})$ and $(1\,\bar{1}\,1)$, wherein the angle between the planes is ~70.5°. HRTEM can accurately reveal the width of a SF only when the SF is edge on (two partial dislocation lines enclosing the SF are parallel to <110>). In <110> orientation, only $(\bar{1}\,1\,1)$ and $(1\,\bar{1}\,1)$ SF are edge on while SF in other orientations are inclined to the surface. Since the SF observed in this study is not all edge on, the estimated SFE may not be accurate in terms of their absolute values. However, for the purpose of comparative study among Au wires with different Ca level, this technique is still considered acceptable.

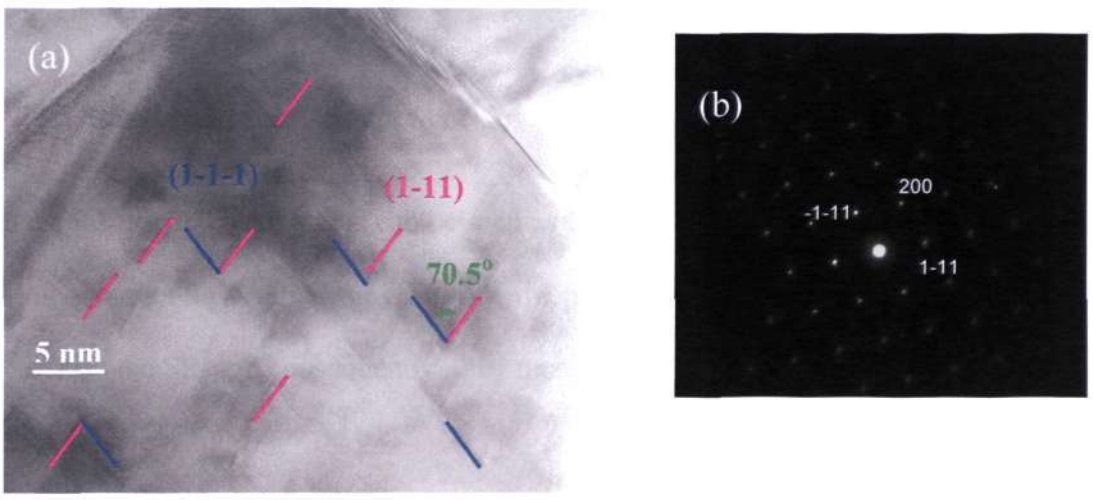

Figure 5-9 (a) HRTEM image from <110> zone axis, showing the labeled v-shaped SF and (b) SAD pattern from <110> zone axis.

Types of Partial Dislocations

SF can be composed by different types of partial dislocations. In the case of FCC metals, there are several types of partial dislocations, including Shockley partial dislocation, Frank partial dislocation, stair-rod partial dislocation etc. The observed SF are further analyzed, to determine the nature of partial dislocation. The most common types of partials dislocation, Shockley partial dislocation is shown in Fig. 5-10. Compared to a full atomic displacement Z, motion going through X then Y is not accompanied by the "up and over an adjacent ball" process as the complete slip, and has lower strain energy. The dislocation reaction is described as:

$$\frac{a}{2}[10\bar{1}] \geq \frac{a}{6}[2\bar{1}\bar{1}] + \frac{a}{6}[11\bar{2}] \qquad (5\text{-}3)$$

These half dislocations are Shockley partial dislocations with $b = \frac{a}{6[112]}$. In three dimensions, partial dislocations can be seen as the bounding dislocations at the two sides of SF. No matter how narrow or how wide the partials are separated, they are bound together by the SF, and consequently, they must move together as a unit across the slip plane (Courtney, 2000).

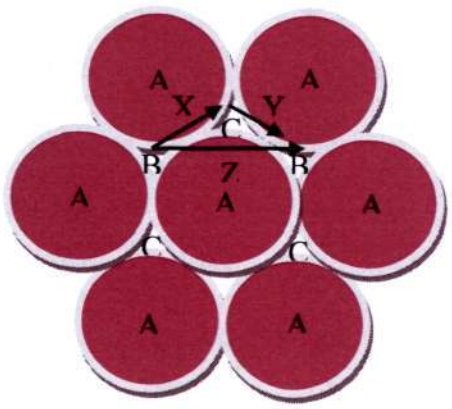

Figure 5-10 A portion of the atoms in a {111} plane in a FCC crystal, where A represents atom.

HRTEM image of a SF taken in Au250 wires is shown in Fig. 5-11a. Fourier transformation was performed on the area a, as shown in Fig. 5-11b. Additional noise is filtered away by selecting $(1\bar{1}1)$ beam only, for more accurate determination of the partials (Fig. 5-11c). Fig. 5-11d is typical $(1\bar{1}1)$ matrix planes obtained by inverse Fourier transformations of HRTEM images of area a. Lastly, the vector component of Shockley partial dislocation is shown in Fig. 5-11e. It can be seen that when we assume the partials are edge on, there are only two possible Burgers vectors. One is exactly perpendicular to (111), that there will be atomic shift of $\frac{a}{6[112]}$, which is ~ 0.16 nm (a is the lattice constant of Au, which is ~ 0.408 nm); Another is Burgers vector of the same magnitude, but is 30° inclined to (111). From the zone axis of <110>, the 30° partial will have a projected length of ~ 0.08 nm, which is about $1/3(d_{111})$ (d_{111} is the interplanar spacing of (111) planes in Au, which is ~0.24 nm). From Fig. 5-11d, the atomic shift at both ends of SF are $1/3(d_{111})$ and $2/3(d_{111})$ respectively, showing that the partial

dislocations are Shockley partial dislocations. As a result, one additional plane is formed within the partial, which is indicated by the green lines, and corresponds to the inset. Shockley partial dislocation has its Burgers vector lying in the plane of the fault, and hence is gissile as full dislocations are. The atomic shift may not be exact, which could be because the SF are not perfectly perpendicular to <110>, or the quality of HRTEM image, which could be attributed to factors like non perfect beam alignment etc.

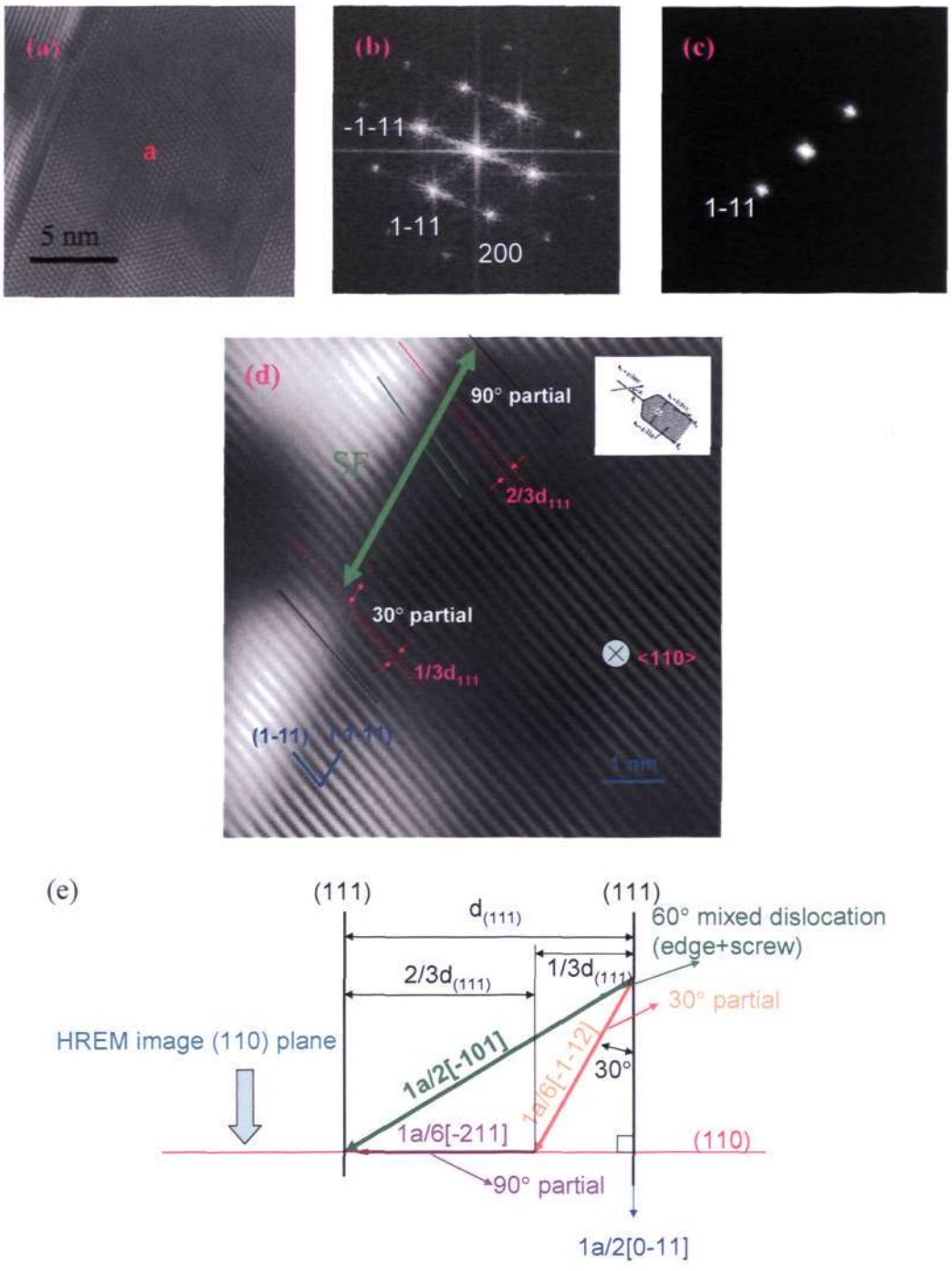

Figure 5-11 (a) HRTEM image of Au250Ca; (b) Fourier transformation of area a; (c) Fourier transformation with selected beam; (d) $(11\bar{1})$ matrix planes obtained by inverse Fourier transformation of area marked a (e) Vector component of Shockley partial dislocation.

Another type of partial dislocation is also observed, which is Frank partial dislocation ($\frac{1}{3}[11\bar{1}]$), as shown in Fig. 5-12. Fig. 5-12a shows the HRTEM image of Au250Ca at another location. {111} and {200} matrix planes obtained by inverse Fourier transformation is shown in Fig. 5-12d. The vectors of Frank partial is relatively straight-forward. Frank partial has $b = \frac{a}{3}[11\bar{1}]$, and the planes shift for $\frac{a}{3}[11\bar{1}]$ in the direction of <111>. The Burgers vectors of Frank partial is not lying in the close-packed plane, and are incapable of gliding, i.e. they are sessile. The atomic configuration of Frank partial is believed to form as a result of the collapse of the lattice surrounding a cavity which has been produced by the aggregation of vacancies on to a (111) plane, as shown in Fig. 5-13 (Smallman, 2007). It can be seen in Fig. 5-12d that the $(11\bar{1})$ plane shifts about 0.23 nm at both ends of the SF. There is a dislocation dipole interacting with the SF (as indicated by black arrows), this makes the plane $(1\bar{1}1)$ off the fault shift. Again, the atomic shift may not be exact as predicted by theory.

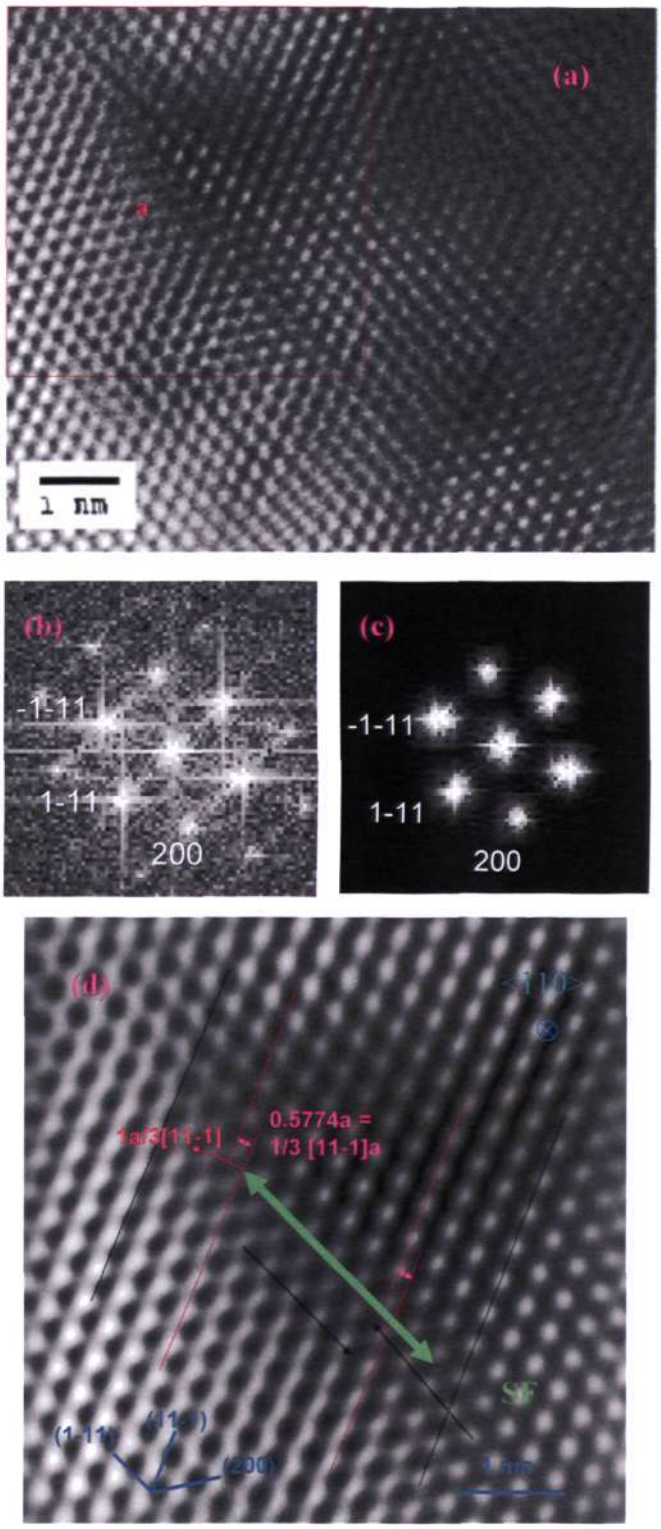

Figure 5-12 (a) HRTEM image of Au250Ca; (b) Fourier transformation of area a; (c) Fourier transformation after filtering noise (d) Matrix planes obtained by inverse Fourier transformation of HRTEM image of a.

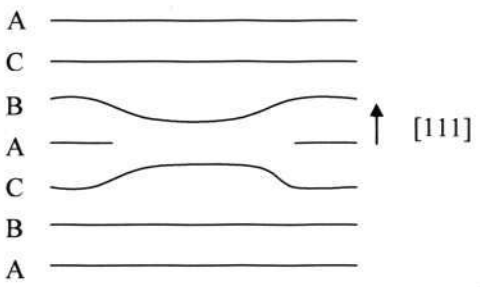

Fig. 5-13 A Frank sessile partial dislocation (Smallman, 2007).

Determination of Stacking Fault Energy

The theory of SFE measurement is not fully established, and many of the SFE values quoted in the literatures are in error by factors of two or more. There are two common methods for SFE measurement, which is the ribbon width measurement method and the node measurement method. In this work, the ribbon width measurement method is used to determine if the SFE of Au wires has been altered by Ca. The equilibrium separation, SFW, of two partial dislocations is related to SFE as follows:

$$SFW = \frac{Gb_1b_2}{8\pi SFE}\left(\frac{2-v}{1-v}\right)\left(1-\frac{2v\cos 2\alpha}{2-v}\right) \qquad (5\text{-}4)$$

where G is the shear modulus, SFW is the equilibrium separation of two partial dislocations, Burgers vectors b_1 and b_2 in a long straight extended dislocation. v is the Poisson's ratio, α is the angle between the total Burgers vector and the dislocation line. By measuring the SFW of Au wires, SFE of Au wires can then be determined. Materials

with lower SFE shall have longer SFW and more occurrence of SF, since the formation of SF requires lower energy (Hirsch, 1977).

Fig. 5-14 shows the SF in the Au wires, as a function of Ca content. It can be seen that the density of SF increases with doping level. As with other FCC structures, perfect dislocation dissociates into two partial dislocations, bounding a SF in Au wires. The lattice shift coincides with the start and end of the 'V', and is taken to be the SFW. The formation of several layers of SF will yield nanotwin. The average number of SF observed in TEM images of the same magnification are ~30 and ~50 for the Au90Ca and Au250Ca wires, respectively. In Au20Ca, very rarely can the SF be observed, which is probably attributed to the high SFE. The shift of the plane is indicated by the blue lines in Fig. 5-14d.

Statistical measurement of SFW in Fig. 5-15 shows that SFW for the Au90Ca wires ranges from 1.5 to 4.5 nm, and has an average value of 2.4 nm. For Au250Ca wires, the SFW distribution increases both in range and average value, to 1.5-7.5 nm, and 3.6 nm, respectively. Plugging in the average SFW value into Eq. 5-4 and taking α of two extreme values (90° for pure edge dislocation and 0° for pure screw dislocation), the estimated SFE are 10-34 mJ/m^2 and 15-50 mJ/m^2 for Au250Ca and Au90Ca respectively. SFE of Au20Ca cannot be estimated, as SF can hardly be seen in Au20Ca. Also, the estimated SFE values are comparable with CG Au (50 mJ/m^2) (Gorelik, 1981). The width of the SF (or the SFE) controls the ease of cross-slip in FCC metals, in which a dislocation changes from one slip plane to another intersecting slip plane. The more

widely separated the partials, the more difficult is the recombination process. As a result, low SFE materials with more and longer SF will cross-slip with difficulty and vice versa (Courtney 2000). To conclude, as postulated, Ca addition does reduce the SFE of Au wires even when added in the ppm level. Characteristic microstructures that one would expect from the difference in SFE, and therefore the difference in cross-slip behavior, are summarized in Table 5-1, and will be discussed in subsequent chapter.

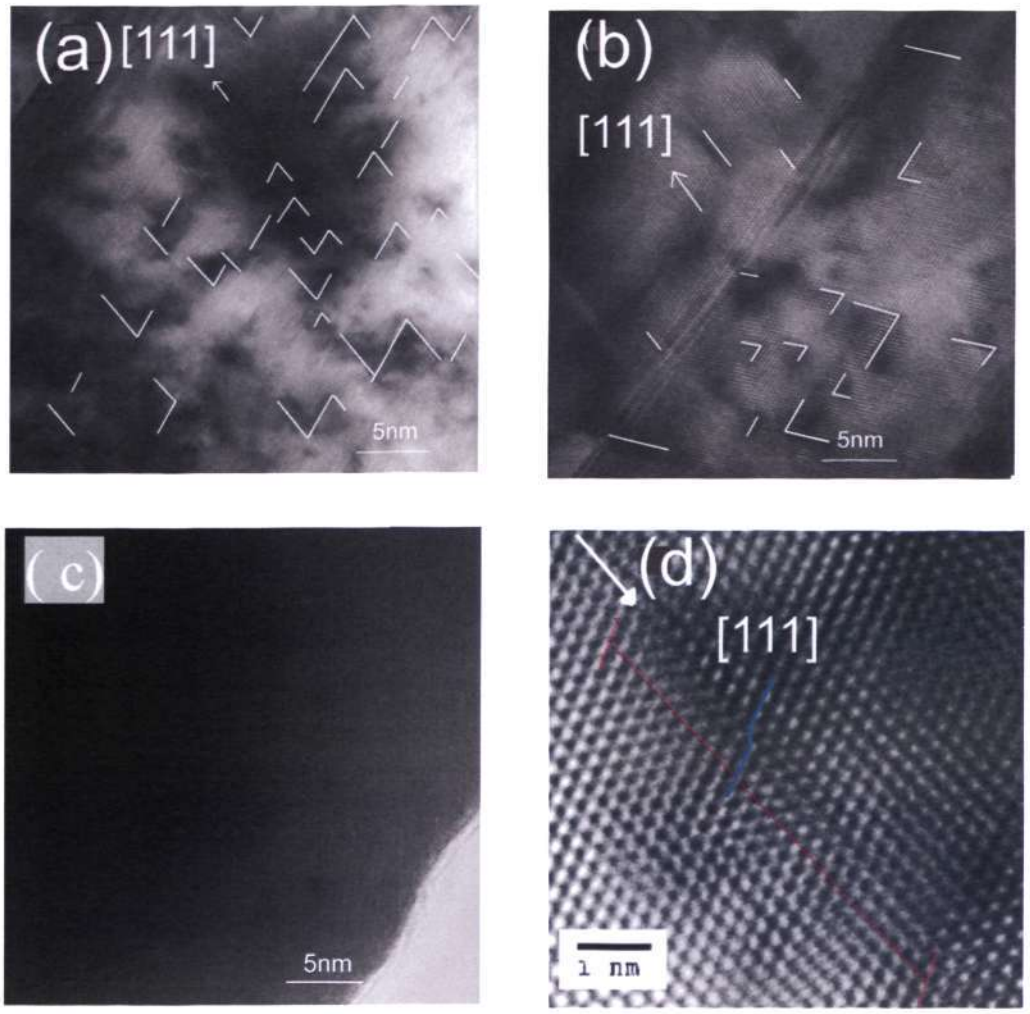

Figure 5-14 TEM images of Au wires at three Ca levels, showing the increase in stacking fault density and stacking fault ribbon width with Ca. (a) Au250Ca; (b) Au90Ca; (c) Au20Ca and (d) HRTEM image of stacking fault.

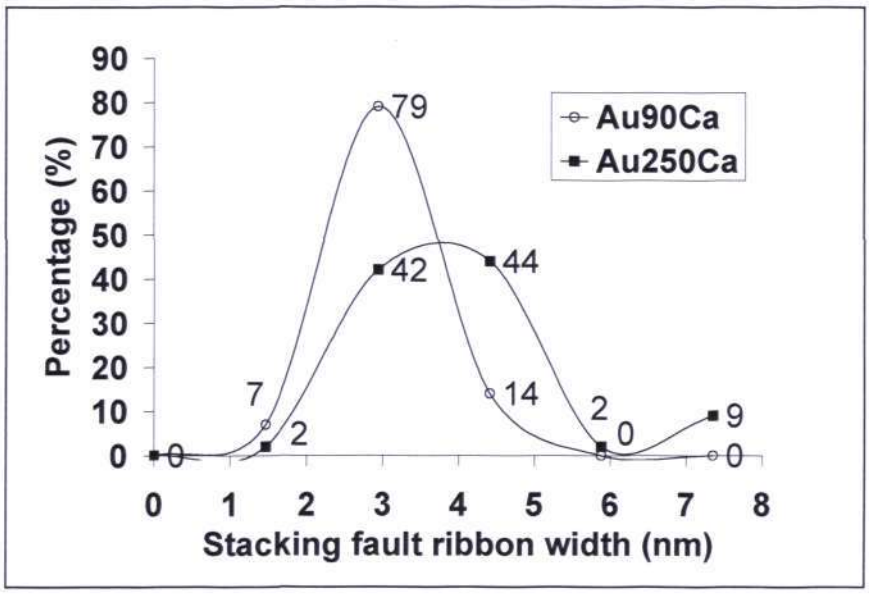

Figure 5-15 Stacking fault width distribution for Au90Ca and Au250Ca wires.

Table 5-1 Typical microstructures expected from metals with high and low SFE (Hong, 1990; Humphreys, 2004)

	High SFE	Low SFE
Grain size	Larger	Smaller
Dislocation pattern	Lower in density, tends to cluster together to form cell structure	Higher in density, distribution is more even and can be found everywhere
Slip mode	Wavy	Planar
Texture	Less random, lesser <100>	More random, more <100>
Twin	Has low frequency	Has higher frequency
Stacking fault	Has low frequency and often short in width	Has high frequency and are longer in width

5.3.2 Microstructures of Au Wires

Typical brightfield low magnification TEM images of Au wires at three Ca levels are shown in Fig. 5-16. As previously discussed, the grains of Au wires have elongated, fiber-like structure along the drawing direction. It is known that the microstructures of Au wires have several characteristic features. Firstly, GS distribution is generally broad, and can span from 100-1000 nm in some cases. Secondly, the smallest GS achievable for Au wires is ~100 nm. Thirdly, most of the GB are not of high-angle type, as Au wires are heavily textured (Chew, 2006). These features are very similar to those samples produced via severe plastic deformation (SPD) process (Dao, 2007). The GS distributions of Au20Ca, Au90Ca and Au250Ca are shown in Fig. 5-16d. While the GS in general lies in the nanometer range, there are some wider grains in Au20Ca. Au20Ca has a main peak centered at ~220 nm and a much less prominent peak at ~700 nm, which seems more like a bimodal distribution. For Au250Ca, the GS are in the range of 100- 300 nm. The addition of Ca can effectively refine the GS of Au wires, an effect well documented in patents (e. g. Herklotz, 2001). Statistically estimated averaged GS (by TEM) of Au20Ca, Au90Ca and Au250Ca are 219 nm, 147 nm and 119 nm respectively. In the inset also we have seen the corresponding selected area diffraction (SAD) patterns, as a function of Ca levels. The SAD patterns show that the diffraction rings get more continuous with Ca, indicating that texture gets more random with the presence of Ca. As it is difficult to collect statistically significant texture data from TEM, EBSD will be used for the characterization of texture (section 5.4).

Cell structure is a unique feature of high SFE materials, in which dislocations are arranged around the periphery of the cell, with the center being free of dislocations, as shown in Fig. 5-17. The black arrows point at dislocation lines, which usually terminate at the GB. By tilting the specimen to a better position, the lines can appear as thin, clear dislocation lines. For example, the dislocation lines pointed by the blue arrows are clearer, since they are in a better orientation for imaging. One small area surrounded by dislocations is indicated by a red box in Fig. 5-17a. The {111} and {200} matrix planes obtained by inverse Fourier transformations of HRTEM image from the red box is shown in 5-17c. Red arrows in the figure point to the location where one additional lattice plane is observed, therefore pure screw dislocations are not considered in this analysis. It can be seen that the arrows are arranged in a cell structure, which surround the area. This is because the dislocations in these metals can glide on more than one glide system, so that dislocations with several different Burgers vectors are available to form cell walls (Humphreys, 2004).

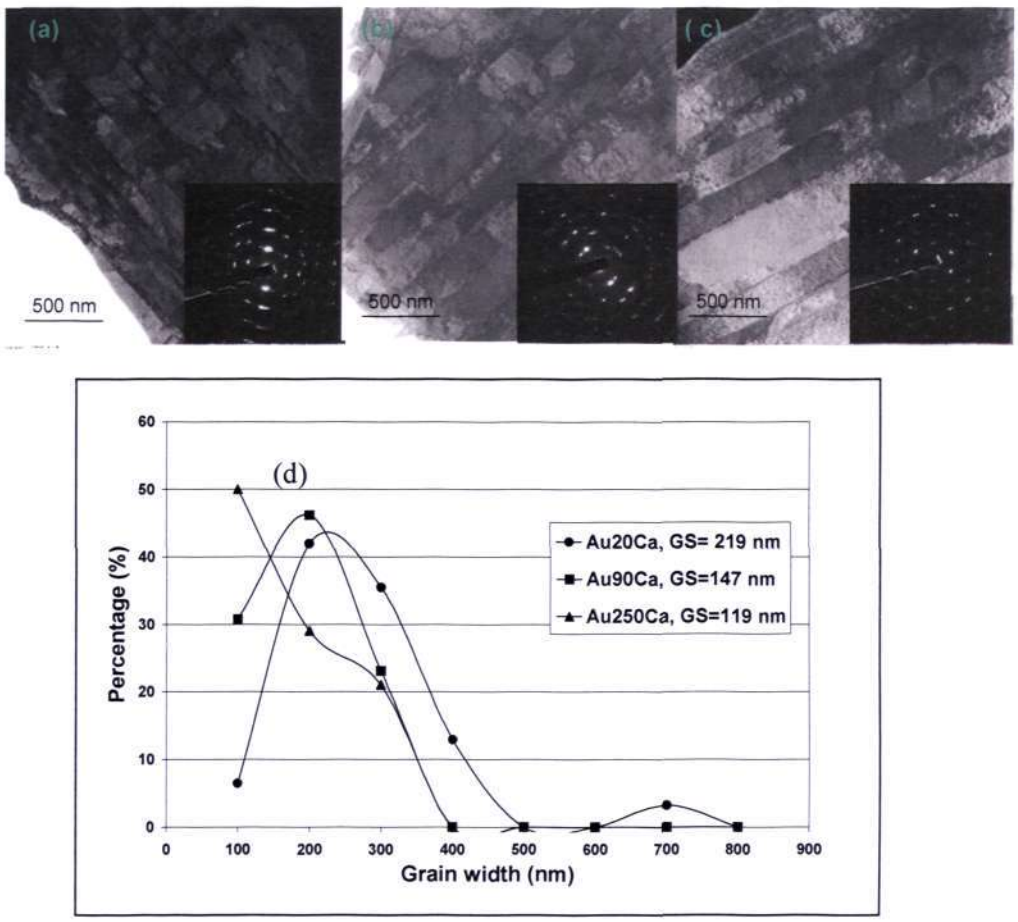

Figure 5-16 TEM images showing the grain size of Au wires. (a) Au250Ca; (b) Au90Ca; (c) Au20Ca and (d) Grain size distribution. Inset in the three images are SAD patterns obtained from those areas.

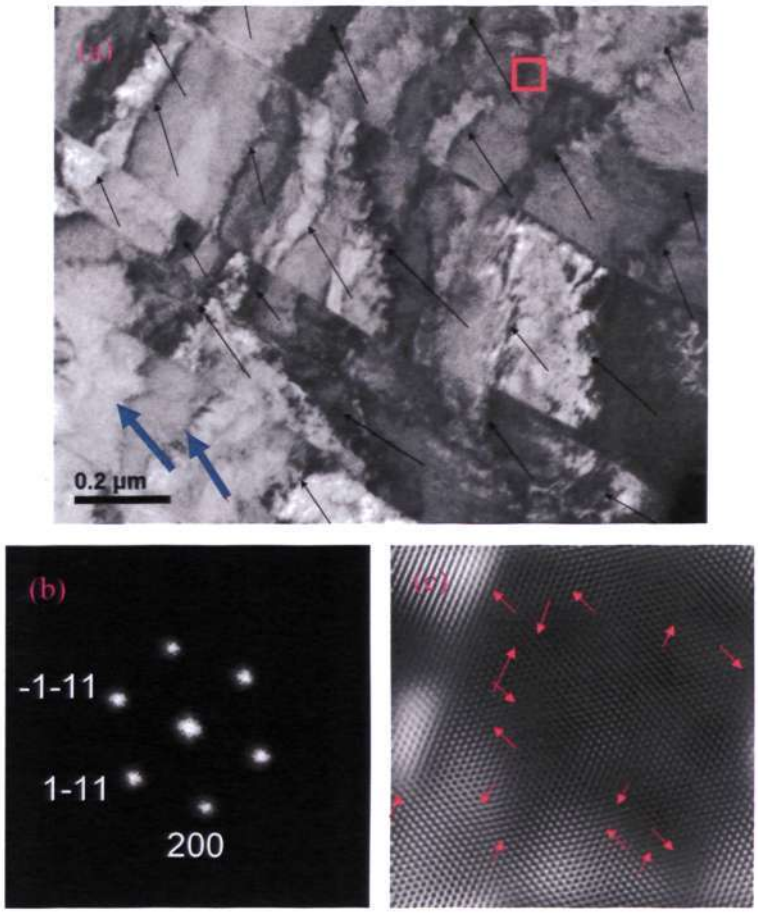

Figure 5-17 Cell structure seen in Au20Ca. (a) At lower magnification; (b) Fourier transformation of the red box area and (c) {111} and {200} matrix planes obtained by inverse Fourier transformations of HRTEM images, showing the cell structure inside the red box in (a).

Some other deformation microstructures that are expected from high SFE metals are also observed in Au20Ca. These features are the occurrence of wavy slip lines (Fig. 5-18) and 'partition like' dislocation structure (Fig. 5-19), both of which are the consequences of extensive cross-slip (Hong, 1990). Dislocation structure in the high SFE Au20Ca tends to be very uneven and most dislocations are clustered in high density regions adjacent to big patches of dislocation-free regions. This is due to the fact that

dislocations in Au20Ca have the freedom of traveling on different glide planes (giving wavy slip lines) and only stop when they run into another dislocation. On the other hand, with suppressed cross-slip tendency, Au250Ca exhibits planar slip mode, in which the straight dislocations are arranged in planar arrays (Fig. 5-18). Also, Au250Ca has a more 'dirty' kind of microstructure, where dislocations can be seen everywhere in the microstructure (Fig. 5-19). This also means that overall, Au250Ca seems to contain much more dislocations than Au20Ca. This is possible, as cross-slip, which is an effective dislocation annihilation process, is suppressed in Au250Ca. To confirm if dislocation density is indeed higher in Au250Ca, other techniques which are less localized than TEM are employed, which will be discussed in the subsequent section.

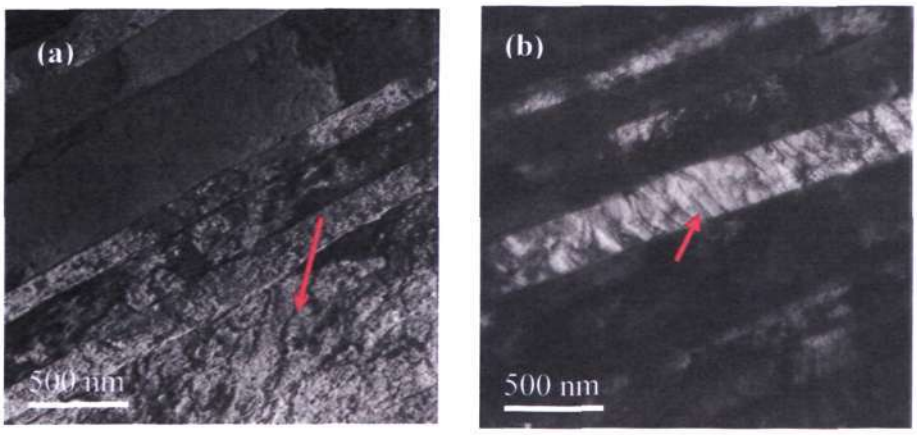

Figure 5-18 TEM images showing slip mode (a) Au20Ca with wavy slip mode and (b) Au250Ca with planar slip mode.

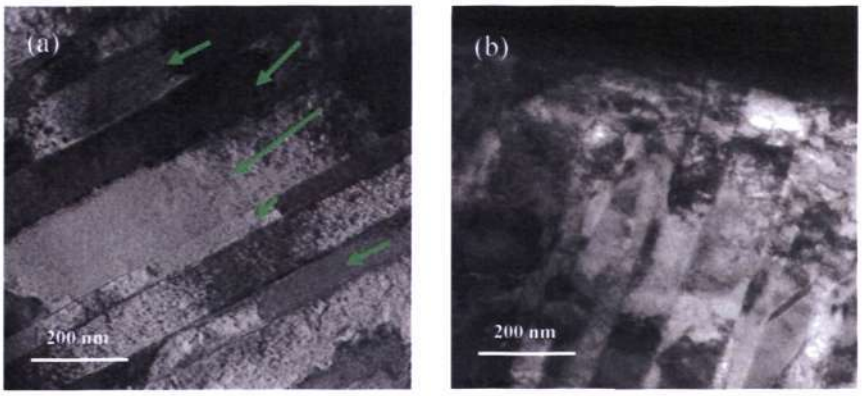

Figure 5-19 TEM images showing dislocation structures (a) Au20Ca with big patches of dislocation free areas, as pointed by the green arrows and (b) Au250Ca with evenly distributed dislocation, which the structure appears to be more 'dirty'.

Another distinct feature that we have seen with samples of higher Ca is the occurrence of nano-twin. This is not surprising, as more SF are observed in Au250Ca, and a twin is formed essentially by multiple SF. These twins are very small, and are not observable at even lower magnification in TEM. As can be seen in the low magnification TEM image in Fig. 5-20, only one twin can be seen at this low magnification, and this twin is relatively big (~ 50 nm thick). Usually only a few twins of this size can be observed at similar magnification.

Figure 5-20 TEM image of Au250Ca at lower magnification, showing the appearance of one twin.

However, large amount of nano-twins of even smaller magnitude, which can be as thin as ~ 1 Å (equivalent to two layers of SF) are also observed in Au250Ca (Fig. 5-21). Even though the twin density can be abundant in some areas, their appearance is localized, i.e. they are not ubiquitous but concentrated in certain areas, likely those containing high local stress. Fig. 5-21c is a typical SAD pattern taken using <110> zone axis from the area containing twin boundaries, which shows the mirror spots appear wrt the {111} plane (William & Carter, 1996). Twinning is not so commonly observed in CG Au. The appearance of nano-twin seems to be unique to UFG Au wires (Kulicke, 2005).

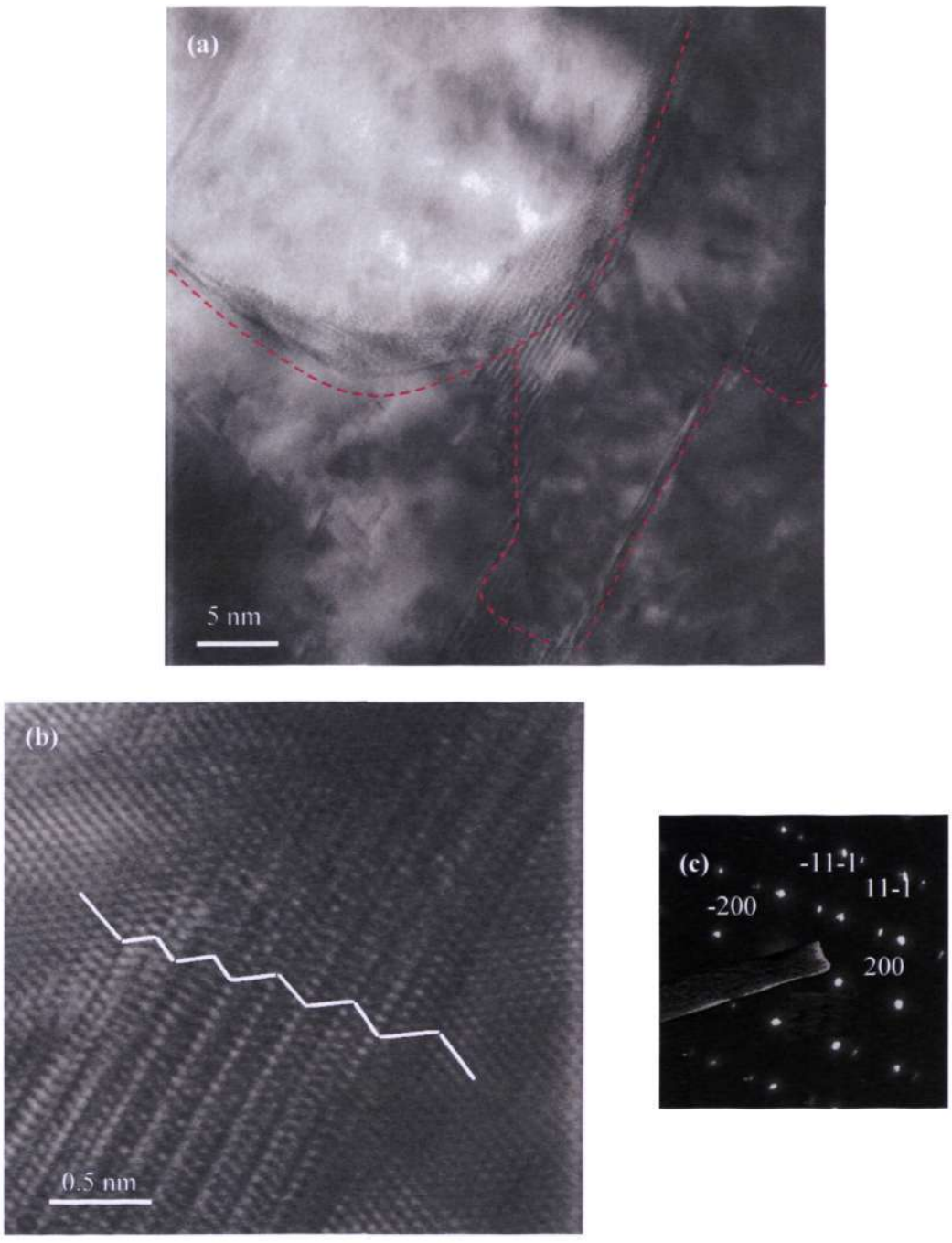

Figure 5-21 TEM image of Au250Ca showing (a) Multiple twins originating from grain boundaries; (b) HRTEM of the twins and (c) typical diffraction patterns obtained from twins.

Twinning is harder to occur in metals with finer GS, as the twinning stress gets higher with reduced GS. However, molecular dynamics (MD) simulation has suggested a transition of twin nucleation mechanism, from pole mechanism to partial dislocation initiated, as GS gets into the very fine size regime (Cheng, 2003). Also, this prediction has been verified by several groups with direct TEM evidence (Huang, 2006; Chen, 2003). For example, Huang et al. has conducted a systematic study to compare two twin formation mechanisms in CG and UFG/ NC ECAP-Cu. in CG Cu, twinning was observed to form in the area with highly localized stress, such as the intersection of shear bands. The twin nucleation mechanism in CG metals is called the pole mechanism, which was first suggested by Venables. The process starts with full dislocation, which dissociates under the action of shear stress, and the gissile Shockley partial moves away from the sessile Frank partial on the plane, leaving an intrinsic fault. Upon meeting a 'pole' (usually a screw dislocation), the partial can rotate around the pole and successively pass on each of the parallel planes and form a twin. As GS continues to decrease, at one point the critical shear stress to nucleate full dislocation will become higher than partial dislocation. In this regime, twins are predicted to form via partial dislocation emission from GB, as observed by Huang in UFG and NC Cu (Gorelik, 1981; Huang, 2006). The critical stress required for nucleating full dislocation is formulated by classical dislocation theory:

$$\tau_F = \frac{2AGb_F}{GS} \qquad (5\text{-}5)$$

while the stress required to nucleate a partial dislocation is:

$$\tau_P = \frac{2AGb_P}{GS} + \frac{SFE}{b_P} \qquad (5\text{-}6)$$

Here b_F and b_P are the magnitudes of the Burgers vectors of the perfect dislocation and the Shockley partial dislocation, respectively. The parameter A reflects the character of the dislocation and other parameters represent their usual meaning as previously mentioned. By equating the two equations, the critical GS at which the transition occurs is ~ 20 nm for Au.

Based on the understanding gained from TEM and MD studies so far, Cheng et al. has classified these differences in deformation mechanism as a function of GS (Fig. 5-22). At the finest GS (GS < 10 nm), no lattice dislocations have been observed in TEM experiments, and MD simulations predicted that the only plastic deformation mechanisms possible are GB processes like GB sliding. Besides small GS, grains are usually required to be round in shape and have high angle GB, to facilitate GB rotation and GB sliding mechanism (Zhang, 2004; Zhao, 2008a). The next-highest GS regime is "Nano-2" (50 nm > GS > 10 nm) , in which partial dislocations first become active in FCC metals, that grains may be sheared by Shockley partial dislocations, which are absorbed in the opposite GB, leaving an intrinsic SF behind. This is the regime where partial dislocation mediated process (PDMP) occurs. The third regime of GS behavior has been dubbed "Ultrafine", referring to GS between 50 nm and 1000 nm. The higher end of the GS boundary of the UFG regime is the GS above which unit dislocations can shear the grains in FCC metals, i.e. the trailing partial can be nucleated before the entire grain is sheared by the leading partial. In the UFG regime, lattice dislocations are nucleated in GB, and

shear the grains. The major difference between this regime and the behavior of traditional metals is that the dislocation sources can only be in GB in the UFG size regime, while both boundary and intragranular sources are important in traditional metals. Finally, at GS > 1000 nm, intragranular dislocation sources will compete with GB dislocation sources to produce deformation, and "normal" metal behavior is to be expected. This regime has been called the "Traditional" range (Cheng, 2003).

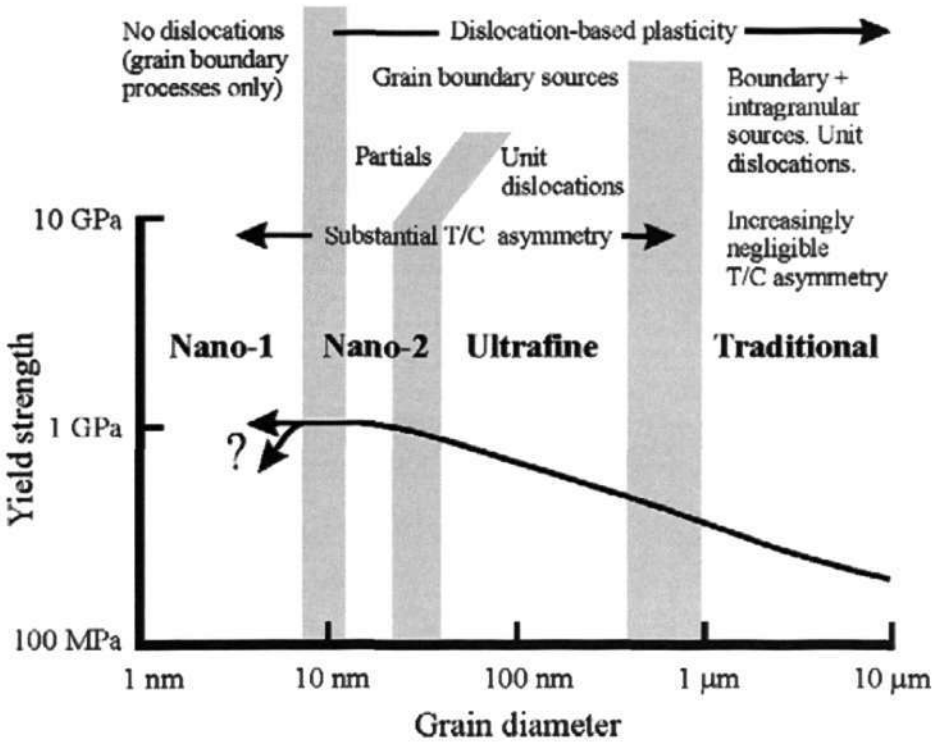

Figure 5-22 Deformation mechanism map for FCC metals, using Cu as an example (Cheng, 2003).

In this study, twins are observed to nucleate from the GB or GB junctions in Au250Ca. In Fig. 5-21, the red lines delineate the boundaries of grains. This suggests that twin nucleation occurs via a mechanism unique to UFG/ NC metals, which is partial dislocation nucleation from the GB. Also, judging from the prevalence of partial dislocations and SF, it seems that PDMP has at least participated in the deformation process of Au250Ca, i.e. the behavior seems to approach Nano-2, even though the GS in this work is relatively big. However, Cheng et al. has noted that the boundaries are not exact, and it is expected to vary as a function of materials, and material constants such as SFE and microstructure.

It is postulated that dopants that segregate to GB can also reduce the SFE in the case of UFG/ NC metals, on top of the segregation to SF as in CG materials. It is known that in CG metals, dopants that segregate to GB can create ledges which are conducive to dislocation generation (Murr, 1975). Similar scenarios can happen in UFG or NC materials, but probably partial dislocations instead of full dislocations shall be emitted, as dictated by the GS. It follows that segregation of Ca to the GB in UFG Au wires can encourage the emission of partial dislocations (giving SF) from the GB, where the ease of SF formation is a sign that SFE has been reduced (Yamakov, 2004). Fig. 5-23 shows the HRTEM of Au250Ca. It can be seen that there is a ledge at the GB, and a twin is generated from the ledge, which could correspond to what was described earlier. Also, the localization of twin formation in Au wires seems to support the deduction that the areas with SF/ twin could be the area where the Ca is concentrated at. Ca first segregates to the GB to accelerate the partial dislocation nucleation process, and also segregates to

SF to stabilize their existence. Therefore, through this double enhancement route, segregating dopant could have a more obvious impact on SFE. Also, it was reported that the impact of SFE on material properties of UFG/ NC materials will be larger than in CG metals (Yamakov, 2004). The hardness of 2 mm Au rod with larger GS experienced ~20% hardness improvement with 90 ppm of added Ca (Saraswati, 2004). For Au wires with very fine GS, tensile strength is increased by 400% with the same level of Ca addition. The results imply that segregating dopants may have a greater role in determining the mechanical properties of UFG and NC metal than their CG counterpart.

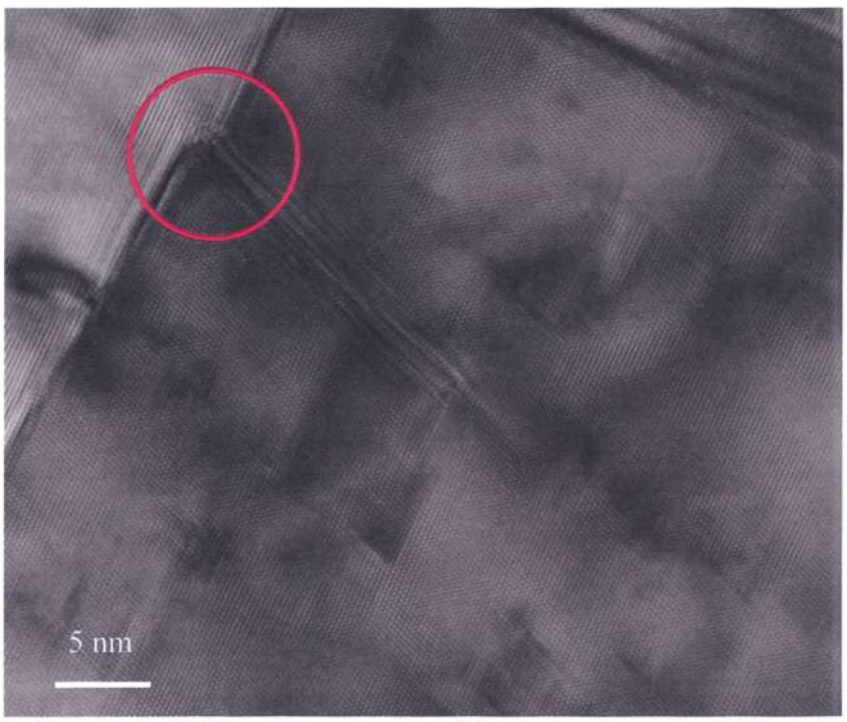

Figure 5-23 TEM images of Au250Ca, showing twin generation from a ledge on the GB.

The occurrence of the above mentioned structures is not absolute in one sample type, but represents the typical microstructure observed. For example, cell structure is

very commonly observed on Au20Ca wires, but these samples also contain areas without distinct cell structure. Also, Au90Ca has more mixed type of structure which is intermediate between Au20Ca and Au250Ca.

It is concluded that the microstructures observed match well with our expectation for Au20Ca with high SFE and Au250Ca with low SFE (Table 5-1). Therefore, in addition to the direct evidence obtained from SFW and SF density measurement, the microstructures observed also support the fact that Ca has effectively reduced the SFE of Au wires (Hong, 1990; Humphreys, 2004). Also, with increasing Ca content, the deformation process has begun to involve more partial dislocation movement (as opposed to slip). The GS range in this work is higher than the proposed boundary for PDMP, which is between 50 to100 nm. This is probably the combined consequence of a lower SFE, and possibly localized stress which is introduced by Ca segregation to GB and/or SF. It is suggested that dopant can segregate to both SF and GB to reduce SFE in UFG/ NC materials, because of their tendency to emit partial dislocations from the GB. Combined with their sensitivity towards SFE, it is deduced that segregating dopants should have greater influence on the properties of FG materials, as demonstrated in this work.

5.4 Texture Measurement with Electron Back-scattered Diffractometer (EBSD)

As pointed out in the discussion about diffraction patterns, preferred orientation (texture) of Au wires seems to get more random with Ca addition. It is expected that a change in SFE will influence the final deformation texture of the wires (e.g. Gorelik, 1981). To confirm this, and to obtain grain orientation information, EBSD study was conducted. While the procedures for characterizing fine wires with XRD have been reported, this method measures the average texture of bundled wire (Montesin, 1992). EBSD is more suited and more reliable to characterize localized texture of single wire strand (Cho, 2002; Wulff, 2002) and is used in this work.

Texture results could differ, depending on the instrument selected and the method of sample preparation. For example, Heizmann has shown that (110) pole figures of cold drawn steel wires are dissimilar in neutron beam and X ray beam measurements, due to the shallower diffraction volume of the latter. Also, texture results are dependant on whether the whole wire is examined and to which depth, if cross-section is used (Heizmann, 1994). For EBSD, the penetration volume is even shallower than X-rays, since electron beam is used in this case. For these reasons, results obtained in this study are only compared with similar EBSD studies conducted on Au bonding wires that are cross-sectioned to the center.

The representation of crystallography texture is conventionally done by means of pole figure and Euler angle. Typical (111) pole figure for Au wire is presented in Fig. 5-24, which is similar to what Cho et al. has obtained on 25 μm Au bonding wires (Cho, 2006). The presence of preferred orientation is revealed by the clustering of points in the figure, as high-lighted by the red lines.

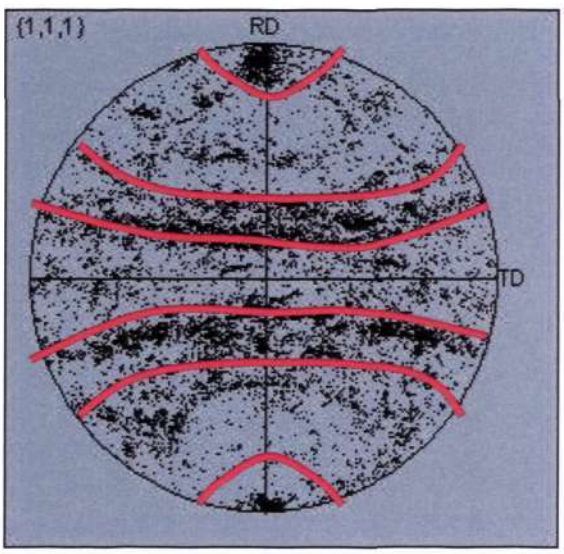

Figure 5-24 Typical pole figure of Au wires.

Also, wire texture is often described by orientation distribution function (ODF) in Euler space. It is known that for Au bonding wire, the Brass, S and Copper are the major components (Cho, 2006). Table 5-2 lists these texture components:

Table 5-2 Texture components in Au wires (φ_2= 45° section) (Humphreys, 2004; Cho, 2006)

Component, symbol	{hkl}	<uvw>	φ_1	Φ	φ_2
Copper, C	112	111	90	35	45
S	123	634	59	37	45
Brass, B	011	211	54	90	45
			125	90	45

The ODF of Au250Ca, Au90Ca and Au20Ca are shown in Fig. 5-25. There are five distinct major peaks for the map of Au250Ca, located near {30°, 78.75°, 45°}, {70°, 39.38°, 45°}, {100°, 78.75°, 45°}, {160°, 39°, 45°} and {180°, 78.75°, 45°}. Two of the peaks at {30°, 78.75°, 45°} and {100°, 78.75°, 45°}, are close to the ideal brass component. Also, the peak at {70°, 39.38°, 45°} is close to the ideal copper component. This is in agreement with literature, where brass and copper are two of the major components found in Au bonding wire. The component S is usually found in wire in the earlier drawing stage, i.e. in bigger diameter, and reduces in percentage when going down to final fine wire size. In the study conducted by Cho et al., they have found S component in wire as fine as 25 μm (Cho, 2006). Wire size in this study is also 25 μm, but S component is not detected for the three wires studied. In Au20Ca, orientation which is closer to brass texture is observed. Copper components, on the other hand, become less prominent. Au90Ca has intermediate texture compared to Au20Ca and Au250Ca, and has more resemblance to Au20Ca since it also does not contain copper component.

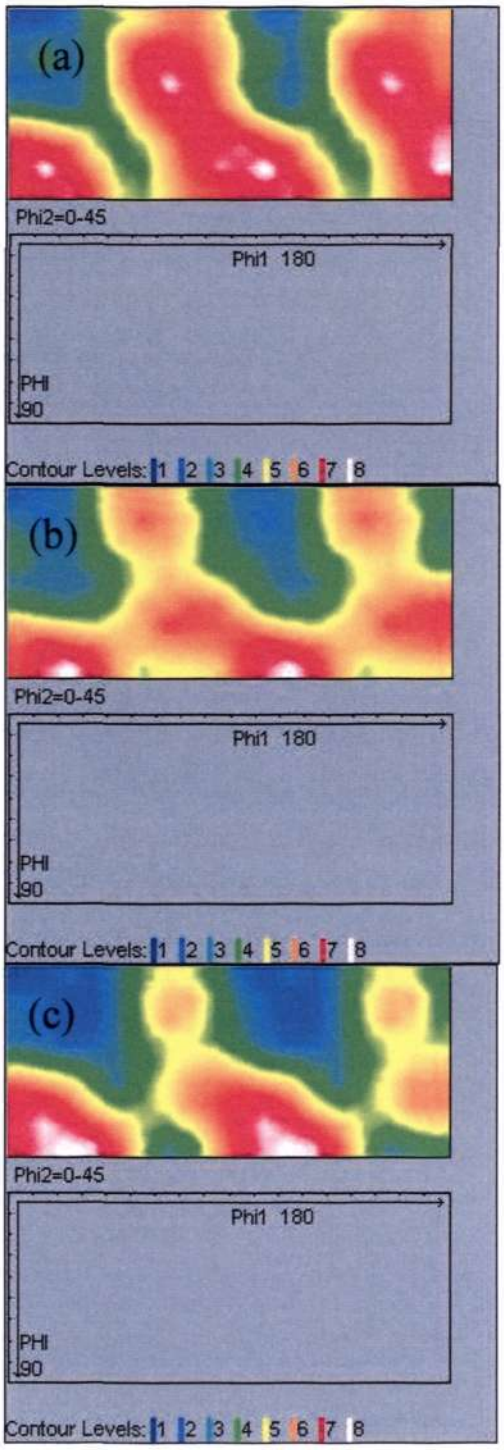

Figure 5-25 Typical ODF (φ_2= 45° section) for Au wire, a) Au250Ca; b) Au90Ca and c) Au20Ca.

EBSD data can also be presented in the form of misorientation angle distribution. By definition it is generated based on the rotation along the shared axis, that one pixel is compared with all neighbors, and the lowest angle is taken (Randle, 1997). Misorientation angle distribution of the wires is shown in Fig. 5-26. For all three wires, the misorientation peaks at ~5-10° and ~40-60°, which agree well with literature data (Cho, 2002). The differences between the three wires are not obvious in this form of representation. However, it is clear that the distribution is non-random, and the peak is different from the Mackenzie plot for the randomly distributed cubic crystals, which peaks at 45° (Mackenzie, 1958). Based on the misorientation angle distribution obtained, a simulation model was built, which we will discuss in Chapter 6.

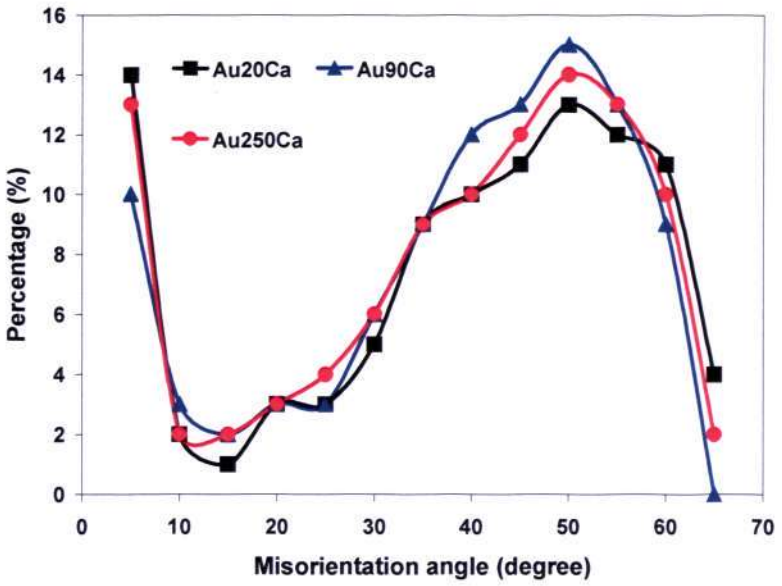

Figure 5-26 Misorientation angle distribution of Au wires.

We have seen that the pole figure, ODF and misorientation distribution angle obtained in this study share common characteristics with those observed in other studies

on Au bonding wires. For the purpose of this project, orientation imaging map (OIM) and the ratio of <100>/ <111> are used as representation of texture, to compare among wires with different levels of Ca. This form of representation is chosen mainly because of the strong correlation between SFE and the ratio of <100>/ <111> in Au Wire (Gorelik, 1981).

Texture evolution of wires is shown in OIM in Fig. 5-27, which includes the data of Au5N. The texture of Au5N contains ~ 80% of <100>, with minor amount of <111> and others complex fiber. This texture is vastly different from the rest of the Ca-doped wires, which they are made up of mainly <111> grains. For Au20Ca, almost all of the grains have their <111> aligned along wire axis. As more Ca is added, <100> texture starts to appear at the surface and the core of the wires. This type of texture, with major <111> and <100> distributed only at the center and surface of the wires was also observed by Cho et al. (Cho, 2002). The black spots on the map correspond to those non-indexed points. This may be caused by poor pattern quality, overlapping patterns at the GB, or the area may be too severely deformed. Also, it can be seen that the mesh size used in Au5N (~0.09 μm^2) is larger than the rest of the wires (~0.02 μm^2), for which the latter is the smallest available mesh size. Mesh size is typically chosen in relation to GS, whereby smaller mesh size is required for materials with finer grains. This is to ensure that there are sufficient detection points within a grain (Humphreys, 2001). However, in practice, the choice of mesh size is limited by the electron beam size. Therefore the resolution can be improved if field emission scanning electron microscope is used. It is also apparent that the GS of Au5N is much larger than the rest of the wires, which

corresponds well to the optical and SEM images of Au5N presented in section 5.2. The variation of <100>/ <111> ratio is summarized in Fig. 5-28. It can be seen that the ratio <100>/ <111> in Au wires gets higher with increasing Ca content.

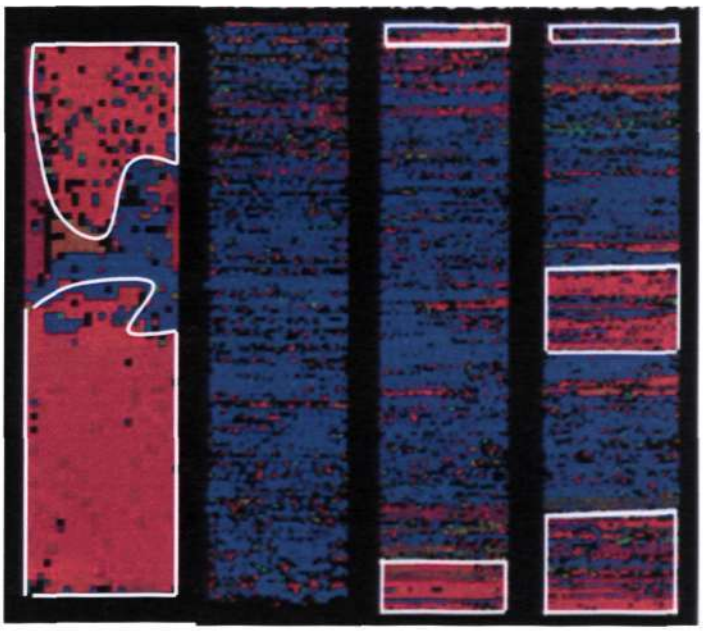

(a) (b) (c) (d)

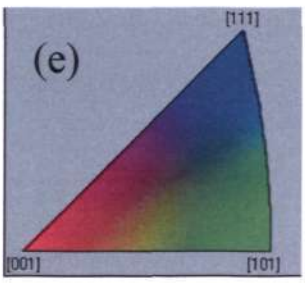

Figure 5-27 EBSD OIM texture distribution of Au wires wrt wire axis, and the grains with <100> orientation is marked by white boxes. a) Au5N; b) Au20Ca; c) Au90Ca; d) Au250Ca and e) color key of the orientation.

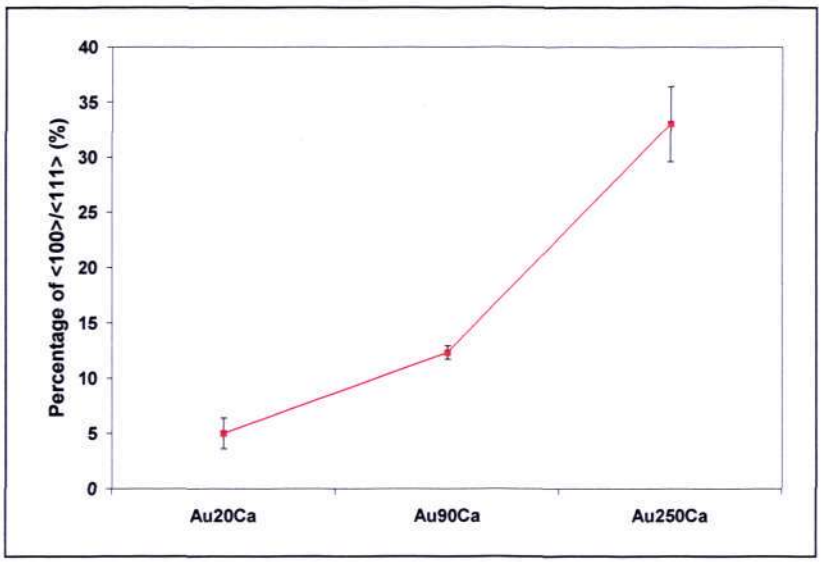

Figure 5-28 Ratio of <100>/ <111> as a function of Ca.

A second parameter, the Taylor factor, is also an indicator for the proportion of <111> to <100> grains. Taylor factor is defined as (Castro, 2006):

$$M = \sum \delta\gamma_i / \delta\varepsilon \qquad (5\text{-}7)$$

Where $\delta\gamma_i$ stands for the amount of microscopic deformation shear stress on any one of the activated slip systems in a given grain, and $\delta\varepsilon$ represents the macroscopic plastic deformation applied externally. For the same value of critical resolved shear stress, those grains with higher Taylor factor will bear a higher flow stress, in which the grains can be considered to be stronger (Cho, 2002). In this work, the average Taylor factors were calculated using the EBSD software. The values are estimated with the standard 12 slip systems for FCC metals, assuming that the {111} <110> slip system is

operative, loading direction is in the drawing direction and velocity gradient appropriate to uniaxial extension as (Wright, 1993):

$$\varepsilon_{ij} = \begin{pmatrix} -0.5 & 0 & 0 \\ 0 & -0.5 & 0 \\ 0 & 0 & 1 \end{pmatrix} \qquad (5\text{-}8)$$

It is known that <100> oriented grains have the lowest Taylor factor whereas the <111> oriented grains have the highest Taylor factor under tensile deformation (Cho, 2002), therefore it can be used as an indication of the proportion of grain orientation. In Fig. 5-29, it can be seen that Taylor factor decreases with higher Ca content, which agrees with previous results that more <100> grains are present when Ca concentration increases. The difference does not seem to be great though, that the Taylor factor ranges between 2.27 to 2.29.

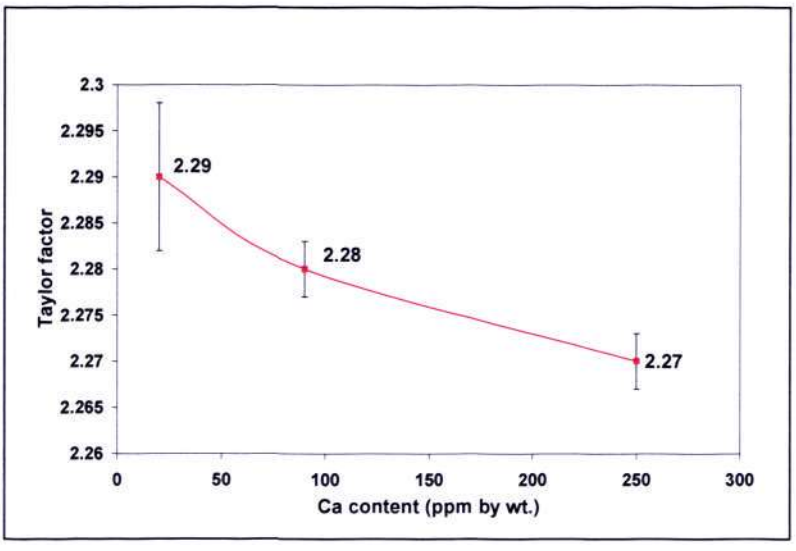

Figure 5-29 Taylor factor of Au wires estimated from EBSD results.

There are two schools of thought to explain the formation of deformation texture in wires. In the first, dislocation density is the key. In the early stage of deformation, cell formation is typically formed by rearrangement of trapped glide dislocations. These will be followed by more localized deformation such as the formation of microshear bands or twinning, when the number of dislocation density grows in a heavily deformed area. At the later stage, the grains will undergo rigid body rotation. The reason for the formation of different deformation texture is attributed to the difference in cross-slip frequency and therefore dislocation density. With low SFE, the dislocations are tightly bounded to their slip planes and are therefore difficult to annihilate. As a result, the accumulated dislocation density increases (section 5.5), which has been confirmed in Au250Ca. These dislocations can be absorbed in the GB, and the Burgers vector components which do not annihilate will produce a change in the orientation relation between the crystal lattices in the two grains. The resultant misorientation is therefore larger, which is the deviation from natural <111> when dislocation density is higher (Aernoudt, 1993; Humphreys, 2004).

From another perspective, this means that Au250Ca has gone through more rigorous extent of deformation than Au20Ca. This is evident from the microstructure of Au250Ca which displays more twin formation and grain rotation. It is generally recognized that the addition of foreign element will accelerate the deformation process. For example, it is known that second phase particle can increase the rate of dislocation generation, and develop local misorientation gradient. This leads to an increased rate in

the generation of high angle GB area with strain so that a submicron grain structure can be obtained at a considerably lower strain than in single-phase alloy (Apps, 2003).

Another mechanism for the formation of deformation texture in wire that was first proposed by Ahlborn and Wassermann is that mechanical twinning is the source of the <100> component (Ahlborn, 1963). It was suggested that the <111> wire texture transforms to the <115> orientation by twinning taking place along the <112> direction, which rotates to the nearby <100> orientation by further deformation (Fig. 5-30). This suggestion which is based on twinning seems to be consistent with our observation, since both the amount of <100> and twin density are higher in wires with higher Ca content. However, the amount of twins observed does not seem to be ubiquitous in our sample, but appears in localized region. In this sense, the first explanation provides a more logical explanation for the formation of deformation texture in Au wires. This could be similar to the classical discussion on rolling deformation texture, whereby metals with higher SFE deform via homogeneous slip, in which the end deformation texture could be well predicted by the full constraints and the relaxed constraints of the Taylor theories (Hirsch, 1988). In our case, this resembles the scenario that homogeneous deformation has occurred in Au20Ca, which has higher SFE and therefore deformation texture formed is largely <111>, as this is the natural deformation texture for drawing. Wires with high Ca content have lower SFE, whereby heterogeneous deformation occurs, leading to localized deformation, such as grain rotation and/or mechanical twinning, which contributes to <100> texture.

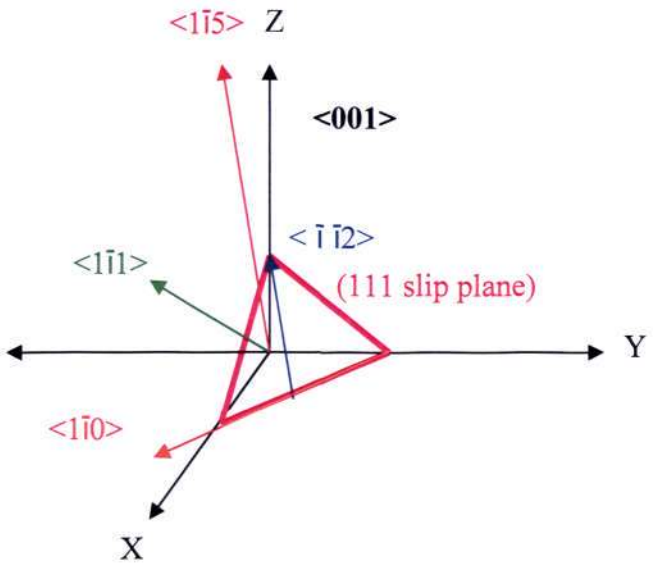

Figure 5-30 Schematic of the possible deformation directions during drawing of FCC Au wires.

Lastly, Schmid factor (S_m) can also be calculated from the EBSD data. S_m is defined as cos φ cos λ, where φ is the angle between the tensile axis and the normal to the slip plane, λ is the angle between tensile axis and slip direction, as depicted in Fig. 5-31. S_m is an important parameter; since it can shed light on the impact of texture have on the mechanical properties of materials (Courtney, 2000).

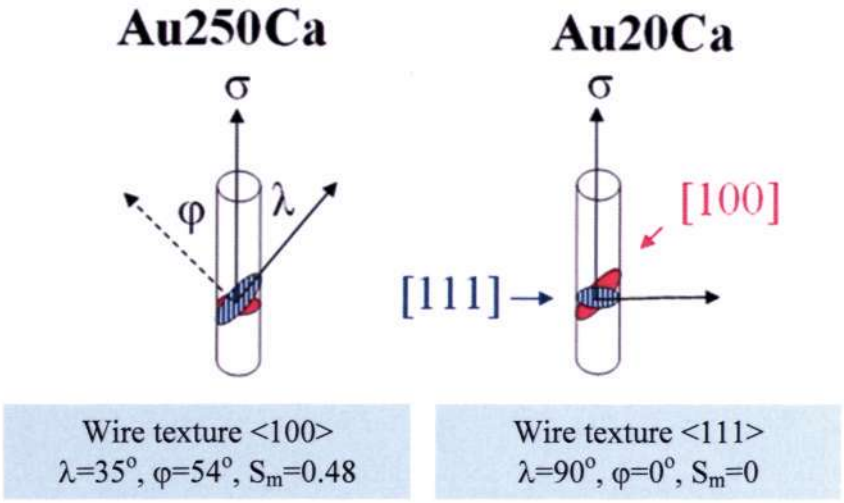

Figure 5-31 Schematic drawing of the grain orientation in Au wires.

Eight planes belong to the {111} family in FCC structure, which are (111), $(\bar{1}\bar{1}\bar{1})$, $(\bar{1}11)$, $(1\bar{1}\bar{1})$, $(11\bar{1})$, $(\bar{1}\bar{1}1)$, $(\bar{1}1\bar{1})$ and $(1\bar{1}1)$ respectively. These eight planes form an octahedron (double pyramid) in FCC crystal (Courtney, 2000). To estimate S_m of <111> and <100> wire texture, the inclination angle of the tensile axis with all the eight planes have to be calculated.

Graphic software Solidworks is being used in this work for the calculation of the angles, as seen in Fig. 5-32 (a). In Au20Ca, two planes of {111} family oriented perpendicular to the wire/ tensile axis, giving $\lambda=90^{\circ}$. On the other hand, the remaining six planes have an inclined angle of 19.5° with the tensile axis. The table in Fig. 5-32 (e) illustrates the interplanar relationship of {111} planes in FCC structure. The possible angles between the {111} planes are 0°, 70.5°, 109.5° and 180°.

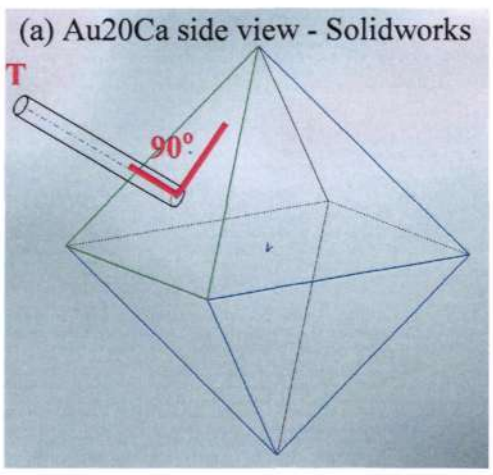

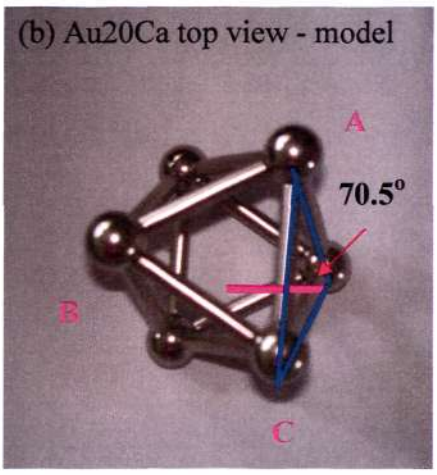

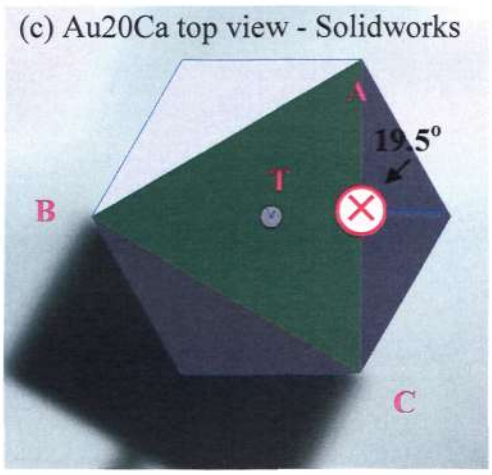

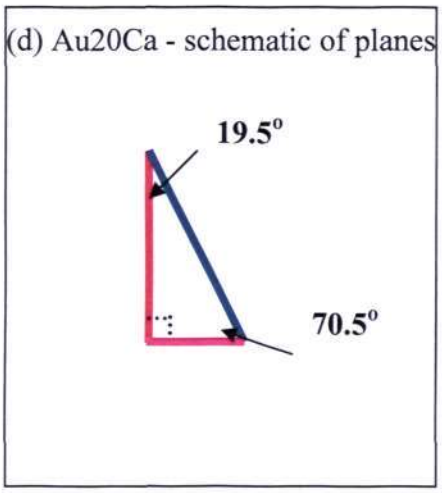

(e) Interplanar relationship of {111} planes in FCC structure (Edington, 1975)

g	Vr Volt	Vi Volt	Amplitude	Phase deg.	||g|| nm-1	||g|| nm	g./ g0	<(g, g0)
(1,-1,1)	26.01553	2.60155	26.14528	5.71059	4.25565	0.23498	1	0.000000
(1,-1,-1)	26.01553	2.60155	26.14528	5.71059	4.25565	0.23498	1	70.52878
(-1,1,1)	26.01553	2.60155	26.14528	5.71059	4.25565	0.23498	1	109.47122
(-1,1,-1)	26.01553	2.60155	26.14528	5.71059	4.25565	0.23498	1	180

Figure 5-32 Inclination angle between tensile axis and {111} planes in Au20Ca: (a) Au20Ca side view drawn with Solidworks; (b) Au20Ca top view of actual model (c) Au20Ca top view drawn with Solidworks; (d) Schematic of planes of Au20Ca; and (e) Interplanar relationship of {111} planes in FCC structure.

For the case of Au250Ca, the scenario is slightly more complicated. Considering the case of <100> wire texture, two of the {111} planes will be at 35° with respect to tensile axis, as shown in Fig. 5-31. Also, four planes are at 7.09° (Fig. 5-33(b)) and two planes are at 35.5° angle (Fig. 5-33(c)) with the tensile axis.

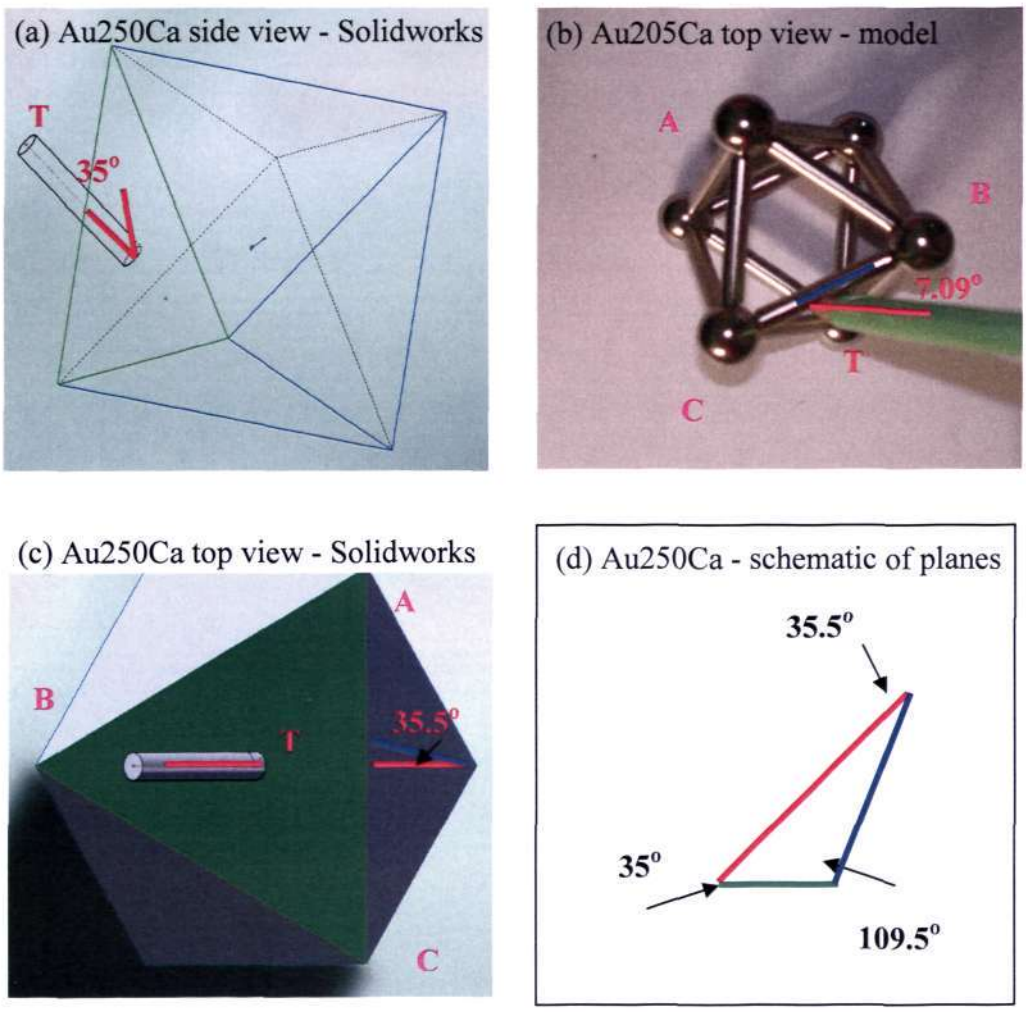

Figure 5-33 Inclination angle between tensile axis and {111} planes in Au250Ca: (a) Au250Ca side view drawn with Solidworks; (b) Au250Ca top view of actual model (c) Au250Ca top view drawn with Solidworks; and (d) Schematic of planes of Au250Ca.

With these, the average S_m from wire texture <111> and wire texture <100> can be estimated as:

Wire texture <111>

= Sum of S_m of 8 {111} planes /8

= [|cos 90 cos 180 | x 2 + |cos 19.5 cos 109.5 | x 6] / 8

= (0 + 0.31 x 6)/ 8 = 0.23

Wire texture <100>

= Sum of S_m of 8 {111} planes /8

= [|cos 35 cos 54 | x 2 + |cos 35.5 cos 54.5 | x 2 + |cos 7.1 cos 97.1 | x 4] / 8

= (0.94+ 0.95+ 0.49)/ 8 = 0.30

Therefore it is seen that wire with <111> texture shall have lower average Schmid factor than <100> texture. However, it is not straightforward to estimate the S_m of the wires as there are many other factors which could have contributed, e.g. the contribution of strain hardening, and the difficulty to estimate the average orientation of all the crystal aggregates. EBSD is used instead for the estimation of S_m of individual wires. S_m is estimated with EBSD software, in which the experimentally determined orientation matrix is substituted into the following equation:

$$S_m = S_X n_X = \cos\lambda \cos\varphi \qquad (5\text{-}9)$$

When (x, y, z) is the specimen coordinate system, with x the axis of the external

load, (x, y) the plane of the investigated specimen surface, z is the axis perpendicular to the investigated specimen surface, S_z is the surface component of the unit slip vector, S_x is the x co-ordinate of the unit slip vector and n_x is the x co-ordinate of the unit slip plane normal (Blochwitz, 1995). The trend of S_m with Ca concentration is plotted in Fig. 5-34, and indeed there is an increasing trend of S_m with Ca. The average S_m determined by EBSD ranges between 0.211 to 0.283, falling at the middle of the possible range of 0 to 0.5.

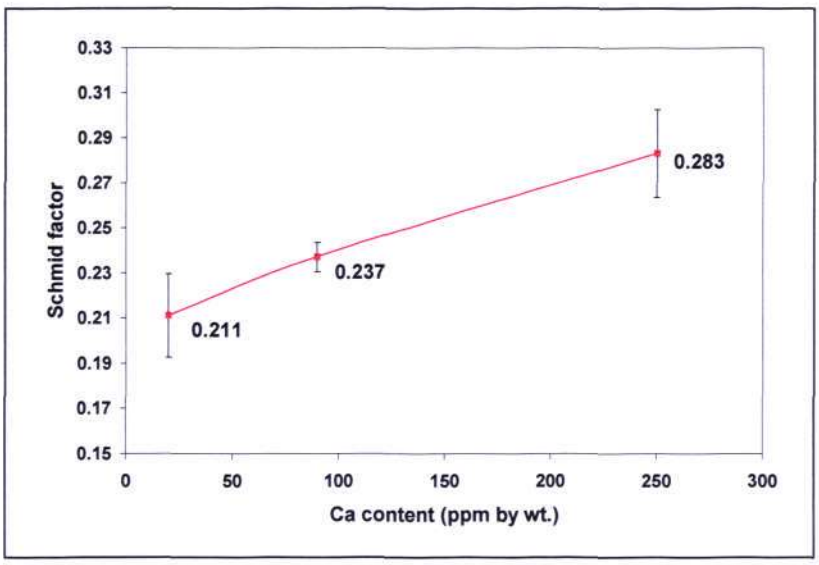

Figure 5-34 Average Schmid factor as a function of Ca content.

5.5 Dislocation density estimation

We have observed with TEM that dislocation density inside the Au wires with higher Ca content seems to be higher. To confirm this point, we have employed several

methods to determine the dislocation density inside the Au wires. There are several common methods, such as TEM, DSC, XRD, resistivity measurement etc. In TEM method, dislocation density is estimated by counting the number of intersecting dislocations with grid lines. This method is applicable when individual dislocations can be clearly resolved (Rohatgi, 2002). Because as-drawn Au wires are heavily deformed, the dislocations can not be easily resolved. Therefore this method is not suitable in our case and is not used. In this section, we will focus on DSC and XRD techniques. Both methods use similar principle that the energy (attributed primarily to dislocations) released is measured, then dislocation density is estimated with formula which relate energy within a material to dislocation density.

5.5.1 Differential Scanning Calorimetry (DSC)

Stored energy measurement was employed by many researchers as an indirect means for dislocation density estimation, as the presence of dislocations in a material is equivalent to a certain amount of stored internal energy (Scholtz, 1999; Rohatgi, 2002). Typical DSC curve of Au wires is displayed in Fig. 5-35. There are usually two broad peaks in the curve- the first one occurs at ~250°C while the second peak is usually at ~350°C. The observation of two peaks is consistent with another reported DSC study on Au wires (Shah, 2004). They presume that the first and the second peak correspond to the recovery and recrystallization phenomena respectively, which is in agreement with our analysis. After going through the first energy release at ~250°C, the microstructure seems to be similar to the microstruture of wires in the as-drawn state, showing that no

recrystallization reaction has occurred. However after the second peak at ~350°C, more equiaxed grains start to appear at the wire surface, signifying that recrystallization has taken place (Kulicke, 2005). The observation is also consistent with literature, whereby exothermic event occurs at $<0.3T_M$ (T_M is the melting point of Au, which is ~1064 °C), corresponding to the first peak, and is usually associated with polygonisation effects due to the formation of low angle GB and recovery, when tangled dislocation arrays release energy. On the other hand, the reaction occurring at $>0.3T_M$, which is the second peak in this case, is more related to the softening of crystal structure and possibly recrystallization, forming relatively dislocation free grains and high angle GB (Hull, 2001).

The total stored energy is taken as the sum of the energy from the two peaks, and their variation is displayed as a function of Ca in Fig. 5-36. There is a general trend that the stored energy released is higher when the wires contain more Ca, except that the stored energy of Au60Ca and Au90Ca are about the same. The order of magnitude of the measurements is similar to that observed by Clarebrough et al. (Clarebrough, 1952).

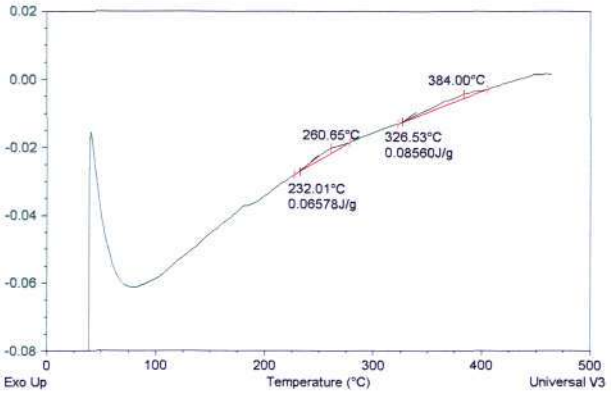

Figure 5-35 Typical DSC curves of Au wires, showing the presence of two broad peaks.

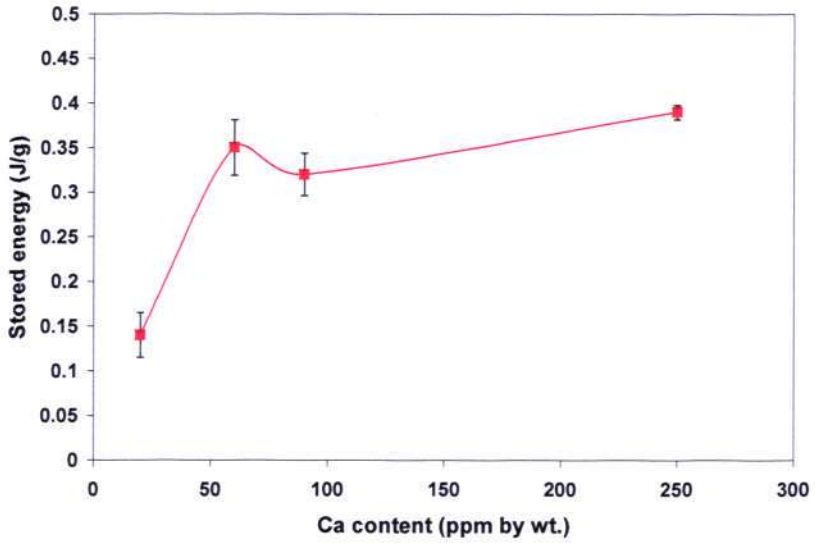

Figure 5-36 DSC stored energy plotted as a function of Ca content.

In cold deformation process, most of the work expended is given out as heat, and only a small fraction remains as stored energy in the metal. Stored energy has two sources, namely the presence of lattice strain and imperfections, while the contribution of the former is usually very small. Therefore the major part of the energy storage is often ascribed to the presence of lattice imperfections. These include impurity, point defects, planar defects, grain size, twinning or orientation. For GS and orientation, they affect the stored energy by modifying the dislocation density and distribution (Martin & Doherty, 1980). This study deals with compositional variation in the low ppm level and is neglected, such that any stored energy variation observed in our study should be attributed to defects.

Firstly, twinning may contribute to thermal energy. However, it is found that the existence of twinning is not ubiquitous in the Au wires of this work, and the overall volume fraction is very low, compared to others studies (Shen, 2005). Therefore, it is deduced that twinning shall not have a major role, given its low density. It is reported that the mobility of point defects is high, except in the special case of deformation at very low temperature, point defects do not contribute significantly to the stored energy of deformation (Zhang, 2001), and is not considered in this study.

GB posses surface energy and their possible contribution to the thermal energy can be estimated (Rohatgi, 2002). Assuming the grains are perfect cylinder of radius r and length L, the total surface area per volume, A, is:

$$A = (2 \pi r^2 + 2 \pi r L) / \pi r^2 L = (2r + 2L)/rL \qquad (5\text{-}10)$$

The surface energy per unit volume attributable to the GB is given as $A\gamma_{Au,}$ where γ_{Au} is the grain boundary energy of Au (0.378 J/m^2) (Murr, 1975). The GB surface energy per gram ranges between 0.001 to 0.003 J/g for the Au wires in this study. Since the magnitude is relatively minute, this effect is neglected in this work. Instead, the focus is on comparing the dislocation density among different compositions. For the purpose of dislocation density estimation, both energies released during recovery and recrystallization are considered.

The dislocation density (ρ) is calculated from the DSC data as:

$$\rho = \frac{\text{net energy released per mole}}{\text{molar volume x } E_{\perp}} \qquad (5\text{-}11)$$

where $E_{\perp}$ represents the energy per unit length of a dislocation, also called the self-energy of a dislocation. $E_{\perp}$ can be calculated as:

$$E_{\perp} = \frac{Gb^2}{4\pi k} In \frac{R}{r_o} \qquad (5\text{-}12)$$

where G is the shear modulus (27 GPa for Au), b is the Burgers vector (taken as a/2[110], which is ~ 0.289 nm), k equals 1 for screw and (1-υ) for an edge dislocation, with υ being Poisson's ratio (0.420 for Au), R is an outer cut-off radius and r_o is an inner cut-off radius, where r_o has been estimated to be about b/2 (r_o is taken as 0.144 nm). The value of R is expected to lie between the values of distance between the dislocations in the tangles and the cell size. In this work, the value of R is taken as the cell size of Au250Ca, which is ~ 100 nm. Taking k=1 for simplicity, $E_{\perp}$ is estimated to be 1.17E-9 J/m and 2.02 E-9 J/m respectively. Using 10.2 E-6 m^3 as the molar volume of Au (Winter, 1993), the ρ estimated from DSC stored energy is summarized in Table 5-3. Since only the averaged stored energy is used for the calculation, there is no standard deviation for the estimation.

Table 5-3 Dislocation density estimated from DSC stored energy

	Dislocation density (m^{-2})
Au20Ca	**6.08E14**
Au60Ca	**1.52E15**
Au90Ca	**1.39E15**
Au250Ca	**1.69E15**

5.5.2 X-ray Diffractometry (XRD)

Microstrain measurement by XRD is another common method used for dislocation density estimation. An example of a XRD pattern for the Au wires is shown in Fig. 5-37. XRD pattern for the selected 2θ range of 30° to 80° matches with the characteristic Au diffraction peaks extracted from the JCPDS standard (JCPDS file no. 04-0784). There are 9 peaks for FCC Au diffraction pattern according to JCPDS file. However, because of the smaller scanning range selected, only 4 peaks, namely (111), (200), (220) and (311) are detected.

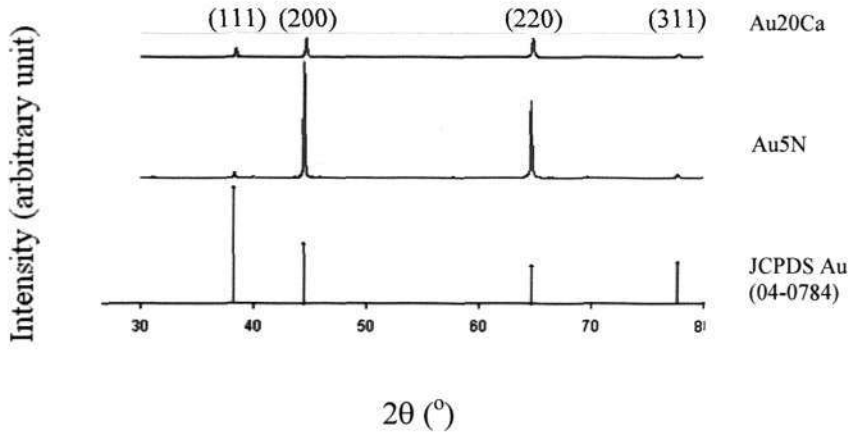

Figure 5-37 Typical XRD pattern for Ca-doped Au wires and Au5N.

It can be seen that the peaks of doped wires are much broader and shorter than Au5N. By measuring these broadening, dislocation density inside a material can be estimated (Chapter 3). The peak broadening (full width at half maximum, β) has three sources: instrumental effects, small particle size, and lattice strain in the material. The individual contribution of the instrumental effect can be separated using several methods (Cullity, 1967 ; Krill, 1998). In this work, the instrumental broadening effect was corrected using parabolic correction as follows (Klug, 1974):

$$\delta(2\theta) = B\left(1 - \frac{b^2}{B^2}\right) \qquad (5\text{-}13)$$

where δ(2θ) is the instrumental broadening corrected peak broadening, b is the β of Au5N and B is the β of the Ca-doped Au wire. The effect of crystallite size is expected to be small, since the GS of Au wires in this work is greater than 100 nm (Krill, 1998).

Most commonly the crystallite size is determined by measuring the Bragg peak width at half the maximum intensity, and estimated using the Scherrer formula (Klug, 1974):

$$\beta_\tau = \frac{\lambda}{\tau \cos\theta} \qquad (5\text{-}14)$$

where λ is the x-ray wavelength, θ is the Bragg angle and τ is a mean 'effective' size of the coherent scattering region normal to the reflecting planes. In addition, due to the additional stress-induced broadening β_ε the following Wilson formula is taken into consideration,

$$\beta_\varepsilon = 4\varepsilon \tan\theta \qquad (5\text{-}15)$$

where ε is a dimensionless value (microstrain) and is usually assumed to be proportional to the square root of the density of dislocation. Assuming that the contributions to the Bragg peak are mutually independent, the total β is as follows:

$$\beta = \beta_\varepsilon + \beta_\tau = \frac{\lambda}{\tau \cos\theta} + 4\varepsilon \tan\theta \qquad (5\text{-}16)$$

Hence, rearranging this equation yields the following:

$$\beta \cos\theta = \frac{\lambda}{\tau} + 4\varepsilon \sin\theta \qquad (5\text{-}17)$$

By plotting the measured value $\beta \cos\theta$ as a function of $4 \sin\theta$ (Williamson-Hall plot), one can estimate the microstrain, ε from the slope of the straight line. Fig. 5-38 shows a typical Williamson-Hall plot of Au wires.

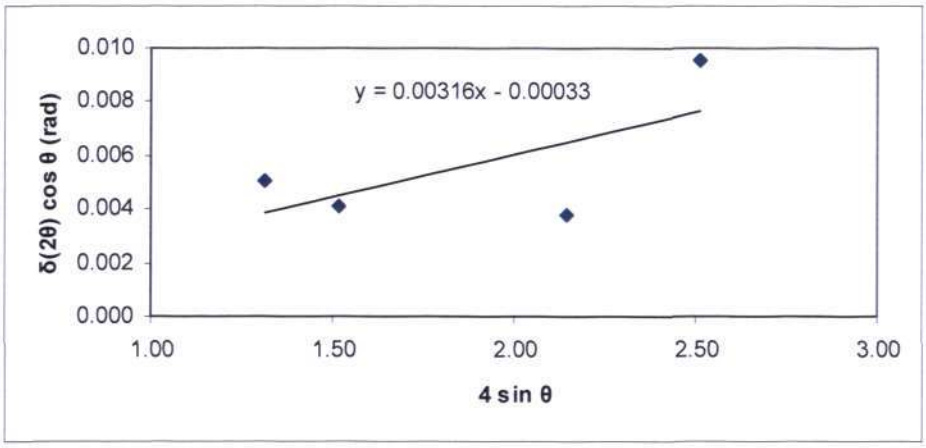

Figure 5-38 Typical Williamson-Hall plot for Au wires.

The microstrain estimated from the Williamson and Hall plots are summarized in Fig. 5-39. There is a similar trend as in the case of DSC stored energy that in general, higher Ca leads to more microstrain. Also, Au60Ca and Au90Ca have similar levels of microstrain. Any lattice imperfection will cause additional diffraction-line broadening in general. Therefore, GS, dislocations, vacancies, interstitials, and substitutional impurities could all lead to increase in lattice strain, with dislocations having the largest effect (Balzar, 1999; Warren, 1969). The effect of low level doping and big GS are neglected, therefore the microstrain is attributed to the rest of the planar defects.

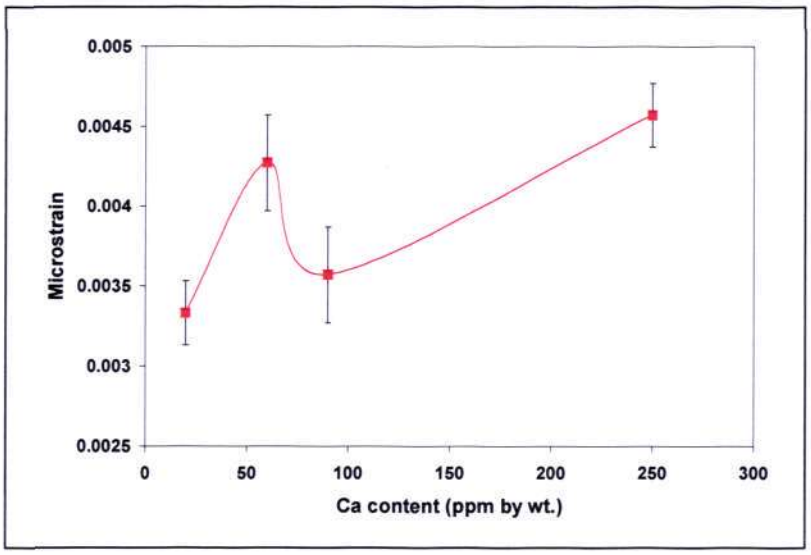

Figure 5-39 XRD microstrain plotted as a function of Ca.

To estimate dislocation density, similar approach as in DSC stored energy estimation is used. After evaluating the amount of microstrain in the wires, the strain energy is then divided by the self energy of one dislocation, such that number of dislocation can be approximated. The lattice strain energy per unit volume is:

$$E_{Strain} = CG < \varepsilon^2 > \qquad (5\text{-}18)$$

Where G is again the shear modulus. The dislocation self energy is defined as in Eq. 5-12. Thus ρ is estimated as:

$$\rho_{\varepsilon} = \frac{A < \varepsilon^2 >}{Fb^2} \qquad (5\text{-}19)$$

Here $A=\pi kC/ \ln(R/ r_o)$, where most variables are as defined previously, C is a

scaling constant in the range of 4 to 7.5, and is taken as 5.75 in this work. F is a correction factor that accounts for the mutual interaction energy of dislocations, and is taken as 1 (Balzar, 1999). The parameters are set as the same values as those used in DSC stored energy calculation. The estimated dislocation density is shown in Table 5-4. The dislocation densities estimated by the two methods are plotted in Fig. 5-40. It is clear from the graph that the dislocation densities estimated by both techniques exhibit the same trend. With more Ca added, dislocation density increases in general. The range of dislocation density estimated by DSC and XRD are on the order of 10^{14} - 10^{15}, and the order of magnitude is in agreement with most reported dislocation density for deformed metals (Scholtz, 1999; Rohatgi, 2002). For Au60Ca and Au90Ca, the difference in dislocation density estimated through DSC is relatively small. For XRD, the density is rather low at Au90Ca.

Table 5-4 Dislocation density estimated from XRD microstrain

	Dislocation density (m^{-2})
Au20Ca	**8.51E14**
Au60Ca	**1.40E15**
Au90Ca	**9.78E14**
Au250Ca	**1.85E15**

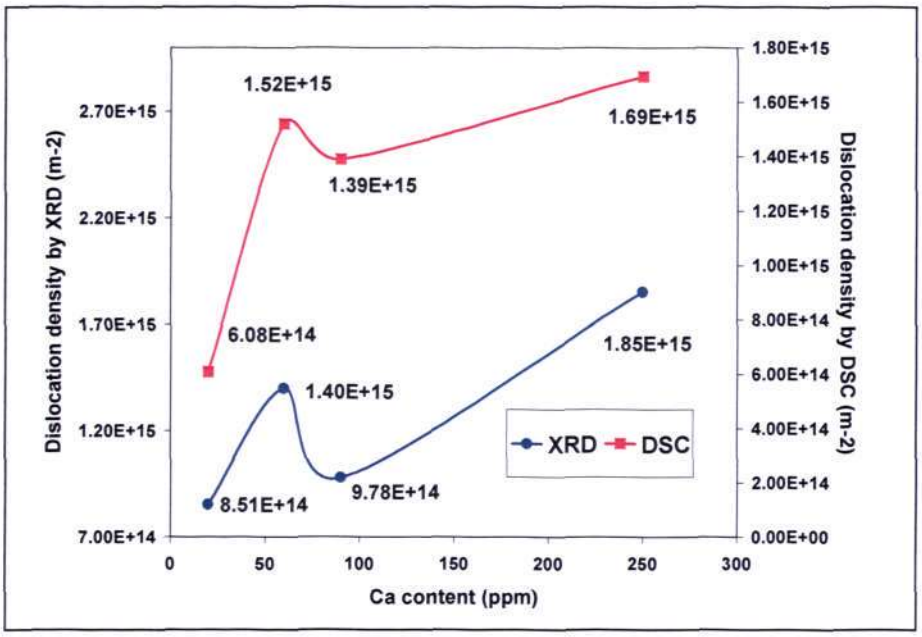

Figure 5-40 Dislocation density estimated from DSC stored energy and XRD microstrain.

5.6 Plastic instability in tension

One proven approach for enhancing ductility of UFG/NC metals is by suppressing their premature plastic instability in tension (Wang, 2004b). This instability originates from the fact that UFG/ NC materials have an inherently low strain hardening rate, which is caused by their inability to accumulate dislocations because of the small GS (Zhu, 2004).

In this sub-chapter, four relevant parameters will be discussed, which are the strain hardening rate (n), uniform elongation (ε_u), strain rate sensitivity (m) and activation volume (v).

According to Hart's criterion for instability against necking, localized plastic instability will take place when the left hand side of Eq. (5-20) falls below zero (Dieter, 1986):

$$\frac{1}{\sigma}\left(\frac{\partial\sigma}{\partial\varepsilon}\right)_{\alpha} - 1 + \left(\frac{\partial\log\sigma}{\partial\log\alpha}\right)_{\varepsilon,T} \leq 0$$
$$(\frac{1}{\sigma} \bullet n) - 1 + (m) \leq 0 \qquad (5\text{-}20)$$

where σ is the true yield strength, ε is the true strain, α is the strain rate, T is the temperature. The two important parameters n and m are the strain hardening rate and strain rate sensitivity respectively.

5.6.1 Strain hardening and Uniform Elongation

The trend of normalized strain hardening rate (n/σ) vs. true strain for the as-drawn wires is plotted in Fig. 5-41. The curves are obtained by the following procedure:

1. Fitting of the true stress-strain curve to obtain a function that best describe the curve
2. Getting strain hardening rate by differentiating the fitting function - d (stress)/d (Strain)
3. Normalize strain hardening rate by every corresponding tensile strength
4. Plot the normalized strain hardening rate with respect to true strain

As can be seen from the graph, there is no significant difference in strain hardening rate between Au wires with different levels of Ca. In the magnified curves, slight difference is observed, that the strain hardening is the lowest for Au20Ca, but

comparable for the rest of the Au wires with higher Ca. In all cases, the initial strain hardening rates are high, but soon flatten into plateau.

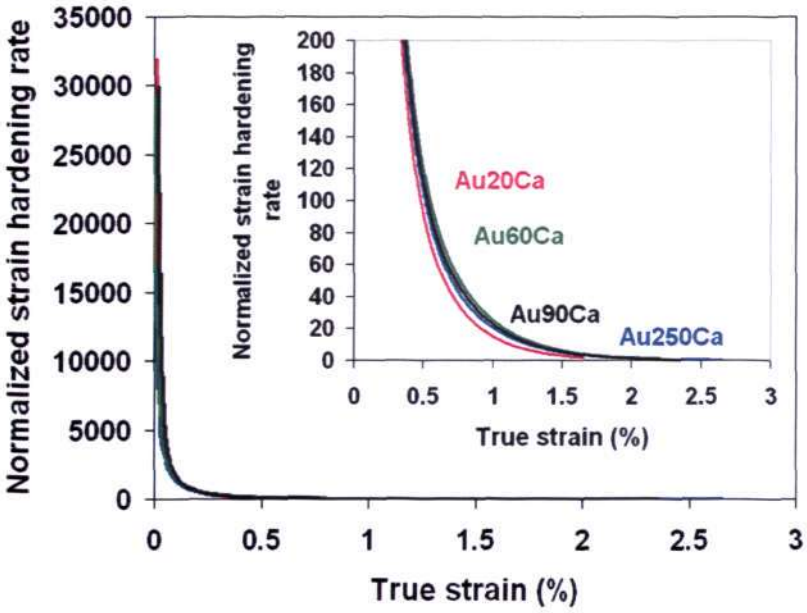

Figure 5-41 Normalized strain hardening rate vs. true strain for Au wires at various levels of Ca. In the inset are the magnified curves.

Also, the uniform strain is defined by Considère criterion (Dieter, 1986):

$$(\partial\sigma/\partial\varepsilon)/\sigma \leq 1 \qquad (5\text{-}21)$$

Uniform elongations (ε_u) of the wires are the elongation when necking commences. It is determined at the strain when normalized strain hardening rate equals to one. As can be read from Fig. 5-41, Au20Ca is the only case which has lower uniform elongation (1.6%), compared to the rest of the three wires (all are having ε_u ~2.1%). This suggests that certain extent of the ductility enhancement may originate from the strain hardening. However, this effect does not extend to the wires with higher Ca

concentration. It is known that reduced SFE will lead to higher n (Ebrahimi, 2004). However, probably because dislocations are highly saturated in high Ca sample, n did not increase substantially.

5.6.2 Strain rate sensitivity and Activation Volume

Strain rate sensitivity (m) can be obtained from the slope of log stress- log strain rate curve at a given strain and temperature. The m values in this study are calculated between 0.5% and 1% strain at room temperature. Figure 5-42 shows the yield strength variation as a function of strain rate. The values of m obtained for Au20Ca, Au60Ca, Au90Ca and Au250Ca are 0.0199, 0.0194, 0.0209 and 0.0233 respectively. To the authors' knowledge, there is no reported m value for UFG Au. In this work, comparisons are mainly made wrt some other common UFG FCC metals, such as copper (Cu) and nickel (Ni). UFG/ NC FCC metals were reported to have higher m, compared to CG metals. For example, UFG Cu having GS in the range of 200-300 nm has m of ~ 0.019 (Wei, 2004) and the m of NC Ni with GS ~ 30 nm lies between 0.01-0.03 (Torre, 2002). Since m is defined in logarithmic terms, the relatively high values of m in UFG/ NC metals will lead to obvious yield strength difference upon strain rate change. This behaviour is very different from CG Cu, which with their low m of ~ 0.004, is known to be rate-insensitive. In fact, the m value is approaching the level of CG BCC metals that are known to be rate sensitive within normal strain rate and temperature. The m values obtained in this study agree reasonably well with the reported m value for UFG FCC metals. Also, the m of Au wires does not change significantly with different Ca content, and have the value of ~ 0.02.

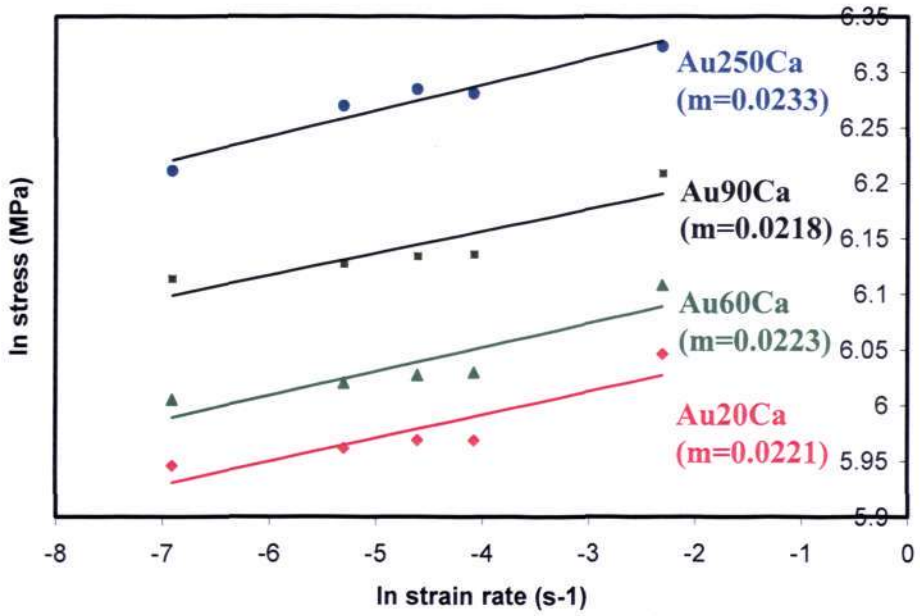

Figure 5-42 A double logarithmic plot of flow stress versus strain rate, from which the strain rate sensitivities (m) can be extracted.

The second parameter, the activation volume, v* is defined as (Li, 2007):

$$v^* = -\frac{\partial \Delta G}{\partial \sigma} \qquad (5\text{-}22)$$

where ΔG = minimum Gibbs free energy that has to be supplied to overcome obstacles at a given temperature. In addition, the experimental v* can be measured by:

$$v^* = K_B T \left(\frac{\partial \ln \alpha}{\partial \sigma}\right)_T \qquad (5\text{-}23)$$

where K_B is the Boltzman constant and T is the temperature, the rest are as previously defined. A linear fit of ln (strain rate) versus stress gives the slope; the values

are then substituted into the Eq. 5-21 for v*. The meaning of v* is broadly defined as the rate of decrease of activation enthalpy with respect to flow stress. This value measures the average volume of dislocation structures involved in the deformation process and its magnitude depends on the nature of the deformation mechanism (Li, 2007). All v* reported in this study are given in normalized form through dividing by the cube of the Burgers vector (b^3). The calculated v* are $17b^3$, $15b^3$, $13b^3$ and $13b^3$ for Au20Ca, Au60Ca, Au90Ca and Au250Ca respectively (Fig. 5-43). Again, the v* does not change much with Ca content. The range is slightly lower than the reported value of 25-75 b^3 for UFG aluminium (Hayes, 2004) and 41-48 b^3 for UFG Cu (Wei, 2004). The values also correspond to the v* range for materials with GS of 10 nm to 1 μm, which is ~ 20- 300 b^3, according to the classification of Conrad et al (Conrad, 2002). This is to be compared with the large v* value, around $1000b^3$, for undeformed CG Cu (Wei, 2004). This is consistent with the trend that with smaller GS, v* decreases.

Wei. et al. have attempted to explain the trend of higher m and smaller v* with a reduction in GS. They have explained it based on different obstacle spacing. In CG materials, obstacle spacing is defined to scale with dislocation density, while it is presumed to depend on GS for the case of UFG/ NC materials. This is based on the understanding that for CG FCC metals, the primary obstacle is the cutting of forest dislocations. With GS decreasing into UFG and NC regimes, now it is the large number of GBs and/or subgrain boundaries that serve as obstacles to dislocation motion. The rate-limiting process is increasingly influenced by dislocation–GB interactions. This type of process typically involves small volumes, for example, when one views the process as

"either dislocation nucleation or de-pinning from the boundary during its propagation", the process would entail an activation length that is a fraction of that of the edge of a grain, thus the small v*. Since v* and m are inversely proportional to each other, the resulted m is therefore larger (Wei, 2004).

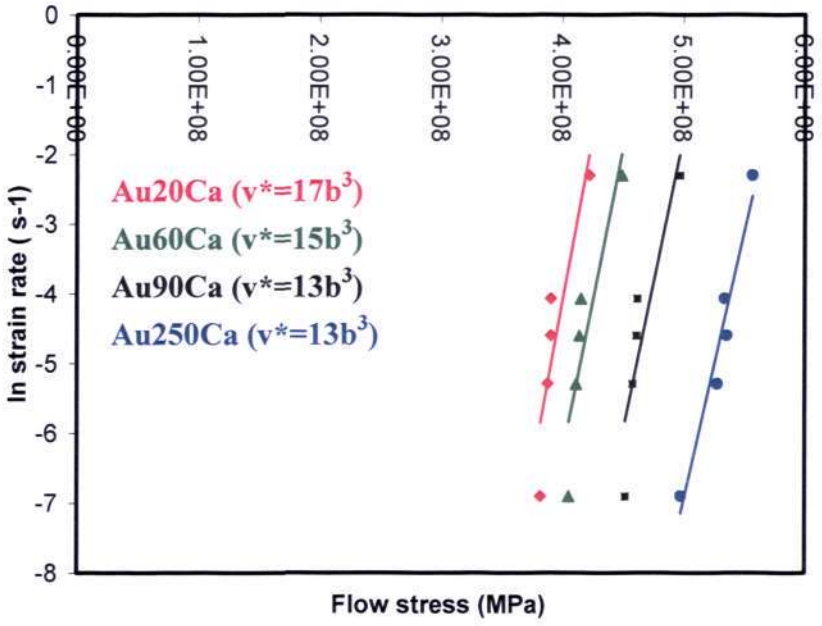

Figure 5-43 Plot of natural logarithmic of strain rate versus flow stress, from which the activation volume (v*) can be extracted.

An analysis of m and v* can give insight into the rate controlling mechanism in the plastic deformation of metals. Although the m value of UFG/NC materials are observed to be much higher than CG materials, the m value is still much smaller than that expected for the plastic deformation process controlled by GB sliding (m = 0.5) or Coble creep (m = 1.0). Taken as a whole, the results indicate that GB diffusion-mediated mechanisms are not yet dominant over dislocation-based processes for Au wires. Also,

the almost constant values obtained signify that there is no migration of deformation mechanism, as we increase Ca content.

Tensile true and engineering stress strain curves of the as-drawn Au wires at several levels of Ca doping are shown in Fig. 5-44. It can be seen that the true and engineering stress strain curves of Au20Ca almost overlap perfectly with each other, showing that there is no significant necking. The separation between true and engineering stress strain curves gets larger at higher Ca levels, which is more obvious in Au90Ca and Au250Ca. This implies that if differences exist, Au wires with higher Ca will have more plastic instability. However, the differences are very minor. It is concluded that based on the observation on m, n, ε_u, v* and stress-strain curves, Ca does not seem to suppress the necking instability of Au wires.

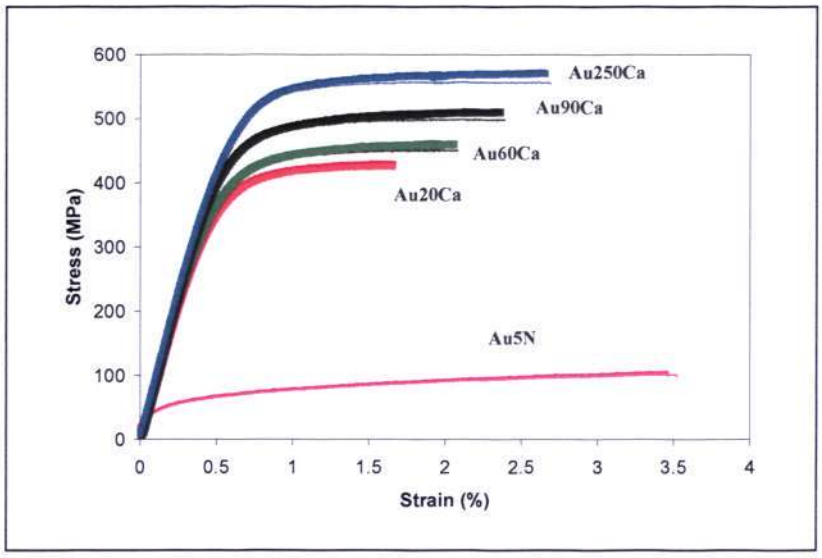

Figure 5-44 True (thick line) and engineering (thin line) tensile stress strain curves of Au wires.

5.7 Working Mechanism of Ca in Au wires

Experimental results from a series of tests designed to unveil the underlying working mechanism of Ca in Au wires are presented in previous section. Based on the results obtained, here we will discuss the possible mechanism which describes how Ca works in Au wires. The key is to propose a mechanism, which can provide explanation for the unusual concurrent improvement in both strength and ductility.

It is well known that, in the case of conventional CG materials, GS reduction has a beneficial effect on both strength and ductility, which is the ***grain refinement*** mechanism (Hertzberg, 1996; Courtney, 2000). This is the driving force behind the increasing research effort on mechanical properties of UFG and NC materials. The strengthening of the materials is assumed to result from the presence of abundant GB that serve as obstacles to dislocation motion. For ductility, this expectation is based on experience with CG materials, in which GS affects yield and fracture strength differently. As GS reduces, the fracture strength increases more than the yield strength, and the materials become more ductile (Lu, 2001b). It has been suggested that the small GS can lead to reduced flaw size and decreased stress concentration, thereby suppressing the crack nucleation/ propagation instability, and enhancing ductility (Wang, 2002). Therefore, grain refinement is one potential mechanism that could be responsible for the phenomenon observed in this work.

For the estimation of strength improvement, both grain refinement and solid solution are considered. The estimated yield strength improvement via grain refinement mechanism is done by Hall-Petch equation:

k $(GS)^{-0.5}$ of Au250Ca- k $(GS)^{-0.5}$ of Au20Ca

= 0.06 $(119E\text{-}9)^{-0.5}$ - 0.02 $(219E\text{-}9)^{-0.5}$

= 130 (MPa)

The calculation assumes that σ_o is the same for Au20Ca and Au250Ca, and the k value of Au250Ca is the same as what has been estimated for Au90Ca (chapter 4). Also, strength improvement due to conventional substitution solid solution strengthening is:

$$\sigma_y = \frac{G\varepsilon_S^{3/2} c^{1/2}}{700} \qquad (5\text{-}24)$$

where G is the shear modulus of the solvent, c is the concentration in at% and ε_s is defined as:

$$\varepsilon_s = \left| \frac{\frac{1}{G}\frac{dG}{dc}}{(1+0.5\left|\frac{1}{G}\frac{dG}{dc}\right|)} - \beta \bullet \frac{1}{a}\frac{da}{dc} \right| \qquad (5\text{-}25)$$

$$\varepsilon_s = \left| \varepsilon_G^{'} - \beta\varepsilon_b \right| \qquad (5\text{-}26)$$

Here ε_G (dG/Gdc)/ ε_b (da/adc) is the fractional change in shear modulus/ lattice parameter per unit solute concentration of solute atom, and β is an empirical constant related to the relative importance of screw and edge dislocations during plastic flow. Both ε_b and β are always taken as positive, while ε'_G can be positive or negative depending on whether the size and modulus effects reinforce each other. Assuming that β is 3, lattice constant and shear modulus increase linearly with composition, and lattice constant scales with the average atomic radius (considering both solute and solvent) (Courtney, 2000), the strength improvement is:

σ_y of Au250Ca- σ_y of Au20Ca

$= 27E9 \times ((1.58)^{3/2})/700 \times (0.12)^{0.5} - 27E9 \times ((1.58)^{3/2})/700 \times (0.01)^{0.5}$

$= 15 - 7.6$

$= 7.4$ MPa

The estimated strength improvement from grain refinement and solid solution gives a total of 137.4 MPa, and this value matches rather well with the experimental value (150MPa). Additional strength may come from sub-GB, SF and twin boundaries that are not accounted for. It is therefore concluded that the major mechanism for strength improvement are grain refinement and solid solution strengthening.

However, while the anticipated strength improvement over CG materials has indeed been realized in many NC/ UFG studies, rarely has the predicted ductility enhancement by grain refinement been observed. In general it is reported that the

ductility of NC/ UFG metals is much lower than that of their CG counterparts, even for metals that are extremely ductile in CG form. For example, as illustrated in Fig. 2-7 in Chapter 2, ECAP-Cu with average GS of ~300 nm has EL of ~15%, while conventional CG Cu can have EL as large as ~ 70%. Specifically, Wang et al. has introduced the concept of having bi-modal or multi-modal GS materials, which exhibit higher ductility by regaining strain hardening capacity. In this case, they purposely introduced grains of ~1700 nm, to couple with the original NC grains. Therefore, larger grains resulted in higher ductility, as opposed to what has been proposed by the theory, which predict ductility increment with smaller GS (Wang, 2004). Based on these general observations in the field, it is suggested that grain refinement mostly does not lead to ductility enhancement in this GS range, and is not likely to provide explanation for the ductility improvement in our study. For example, annealed wires with larger GS have higher ductility than as-drawn wires with smaller GS (Kulicke, 2005). In summary, grain refinement is seen to account well for the strength improvement observed in this study. However, the improvement in ductility requires further explanation.

As discussed, the ***suppression of plastic instability*** in tension is the only proven method for ductility improvement in UFG/ NC metals so far, and the discussion is not complete without reviewing this concern. Either by raising the strain hardening rate (m) or the strain rate sensitivity (n), plastic instability can be delayed and this will prevent the occurrence of premature necking. We have shown that the normalized strain hardening rate of Au20Ca is slightly lower compared to the rest of the wires, corresponding to the lower uniform elongation observed (section 5.6). This suggests that there exist slight

differences in strain hardening behavior with Au wires with 20 ppm Ca and the rest of the wires. However, the strain hardening rate and uniform elongation of Au60Ca, Au90Ca and Au250Ca are all comparable. Also, m is not increased by Ca addition. Therefore, it is concluded that Ca does not significantly affect the plastic instability of the Au wires, and this does not seem to be the mechanism to provide an explanation for the progressive increment in ductility.

Also, it was suggested that new, GB-related mechanisms are operative in materials with very fine GS, which differs from the conventional cutting of forest dislocation mechanism in CG materials. These mechanisms can contribute to higher ductility in UFG/ NC materials. As discussed in section 5.3, the behavior of the Au wires seems to be approaching the 'Nano-2' regime, where PDMP has participated in the deformation process. However, it is not likely that GB sliding has occurred in our samples. First, our GS are far from the predicted boundaries of 10 nm and below, where GB rotation and GB sliding are preferred. Second, the elongated grain shape of Au wires does not favor these mechanisms, as long grain shape is known to be effective in inhibiting GB sliding as interlocking of GB occurs (Hertzberg, 1996). Also, both the values (m~0.002) and the consistency of m and activation volume (v*) signifies that GB sliding (m~0.5) has not taken place, and the mechanism does not migrate as Ca increases. Therefore the contribution of ***GB sliding*** to the ductility of Au wires is not anticipated.

Twinning can also lead to higher ductility, as they increase the capacity for dislocation multiplication, giving higher n (Dao, 2006) and/or higher m (Ma, 2004).

These twins can refer to growth-in twin formed during processing (Shen, 2005; Zhao, 2006) or deformation twins which occur during actual deformation test (Wu, 2006a). We have not observed deformation twinning which was produced during tensile deformation process in this work. This agrees with literature observation, as deformation twinning usually occurs in samples that were subjected to complicated stress states and high stress levels, such as during indentation, grinding, high-pressure torsion, high-rate cold rolling etc. The only reported deformation twin generated during uniaxial tensile testing is conducted at cryogenic temperature (Wu, 2006a). The density of growth-in-twin does seem to get higher with Ca, however, their existence is not ubiquitous, and the overall volume fraction is very low, compared to others studies (Shen, 2005). Also, twins enhance ductility by improving m and/ or n, which is not observed in this study. To summarize, twinning does not provide satisfactory explanation to the ductility improvement observed. It is believed that ductility enhancement by twinning alone is usually very limited. However, the orientation change resulting from twinning may place new slip systems in a favorable orientation wrt the stress axis so that additional slip can take place (Zhang, 2004). This leads us to the next mechanism, which is related to the texture of the Au wires.

The evolution of ***texture*** with Ca was shown, that the ratio <100>/<111> in Au wires gets higher with increasing Ca content. There are possibly two implications from the change of texture. Firstly, texture affects the level of the resolved shear stress (τRSS) experienced on slip planes, which are the major strain carrier (Courtney, 2000):

$$\tau_{RSS} = \frac{P}{A_o} \bullet \cos\varphi \cos\lambda = \frac{P}{A_o} \bullet S_m \qquad (5\text{-}27)$$

Here P is the axial load, A_o is the cross-sectional area of the sample and S_m is the Schmid factor as previously defined. The grains with higher S_m will experience higher τ_{RSS}, therefore fulfilling the critical resolved shear stress easily. Consequently, it is easier for slip to be initialized in these grains. Secondly, the change in texture may activate other secondary slip systems (Valle, 2006). However, Au being FCC does not have secondary slip system (Courtney, 2000).

Au20Ca is expected to have very low average S_m value, as it has predominant <111> wire texture. This orientation is 'the worst orientation to slip', as some of the {111} planes are orienting at right angle with respect to the tensile axis, and the average S_m is low (section 5.4) . It is therefore foreseeable that the ductility of Au20Ca will be largely constrained by these {111} planes. The addition of Ca has reoriented some of the {111} slip planes to be close to 'the ideal orientation to slip' (45° off the tensile axis, which gives maximum S_m ~0.5), and this is the <100> wire texture. And through calculation, we have seen that <100> wire texture has higher average S_m. Therefore, the average S_m from all the polycrystalline aggregate in Au250Ca will be much higher than in the case of Au20Ca. Au250Ca is expected to have better ductility, with these favorably oriented slip planes. The values of S_m estimated from EBSD results have confirmed this deduction, that S_m of Au20Ca and Au250Ca are 0.211 and 0.283 respectively (section 5.4). With higher S_m, Au250Ca has removed the deleterious texture for plastic flow, and gains ductility.

Similar approaches of modifying texture for higher ductility in UFG/ NC materials were also adopted by several groups (Mukai, 2001; Agnew, 2004; Valle, 2006). Magnesium alloy produced with conventional extrusion process has a low ductility, when the slip plane is oriented perpendicular to the extrusion/tensile axis (this gives S_m ~0). Mukai et. al were the first to demonstrate that in the case of the ECAP process, the slip planes reoriented at ~45° to the tensile axis, such that the elongation was twice larger than the sample produced with conventional extrusion process (Mukai, 2001). For the case of Mishra et al., they have added 0.2% cerium into magnesium to improve ductility. This has been attributed to the corresponding microstructural changes that the orientation of the basal slip plane is re-oriented to yield a larger average S_m (Mishra, 2008). This effect is very similar to what has been observed in this work. It is important to note, however, that yield strength usually decreases at the expense of ductility when texture engineering is invoked. Here, the strength in Au250Ca is high, as the samples contain more grain and twin boundaries, effective solid solution strengthener as well as SF and dislocations. To the author's knowledge, this is the first demonstration that even with a change in texture which yields higher ductility, the yield strength of the UFG metals is also enhanced. The summary of the working mechanism is presented in Fig. 5-45.

It can be seen from Fig. 5-45 that some boxes are highlighted in blue, which refer to mechanisms operative in both CG and UFG/ NC materials. Boxes that are high-lighted in red refer to the mechanism that is only applicable for UFG/ NC materials. It is known that segregation of solute to the SF to stabilize them is the mechanism of SFE reduction in the solid solution of CG metals (Hirth, 1986). It is proposed that Ca not only reduce

SFE through segregation to SF as in the case of CG materials, but they also concentrate along the GB and triple junction to serve as dislocation source for partial dislocations. The rationale is based on the fact that GB is the dominant dislocation source in FG materials, and partial dislocation instead of full dislocation emission is favored (Cheng, 2003). In this sense, Ca first accelerates partial dislocation nucleation (by segregating to GB) and later stabilizes their existence (by segregating to SF). This leads to effective SFE reduction at low dopant concentration. It is therefore inferred that segregating dopant shall have a greater impact on SFE of UFG/ NC materials, compared to their CG counterpart. Also, it is known that the effect of SFE on material properties is more pronounced at smaller GS, where the emission of partial dislocations is more prevalent (Yamakov, 2004). As a result, Ca plays influential role on the mechanical properties of Au wires even when present at low ppm level. And this effect is of course dopant dependant. For example, Ebrahimi et al. has shown that Cu is more effective than iron on SFE reduction and therefore mechanical properties of Ni (Ebrahimi, 2004).

SFE reduction leads to the formation of profuse partial dislocations, whose density continues to accumulate, since they can not cross-slip because of their edge component, which also gets stabilized by Ca (Courtney, 2000) (Fig. 5-45). The direct consequences for lowering SFE are: the attainable minimum GS should get smaller, SF and twin densities get higher (Mohamed, 2003, Zhao, 2007) and there will be higher proportion of grains with <100> aligning with wire axis (Gorelik, 1981). The strength mainly comes from grain refinement, defects and solid solution, as discussed previously. Ductility is improved in Au250Ca since the <100> orientation has higher Schmid factor,

and is therefore released from the severe constraint that is imposed by <111> wire texture in Au20Ca. By manipulating SFE, several authors have also increased the ductility of UFG and NC materials, via increasing n (Ebrahimi, 2004; Zhao, 2006). This behavior seems different from CG materials, where lower SFE will lead to higher strength, but not higher ductility in all cases (Zhao, 2006). This is probably because n is not the limiting factor of ductility in CG materials. In our case, n is not increased by Ca, possibly because of the saturation of dislocations, which is expected to have a discounted effect on n (Huang, 2008). Lastly, GB-related mechanism that is not operating in CG materials has been ruled out, based on GS, grain shape and m value obtained.

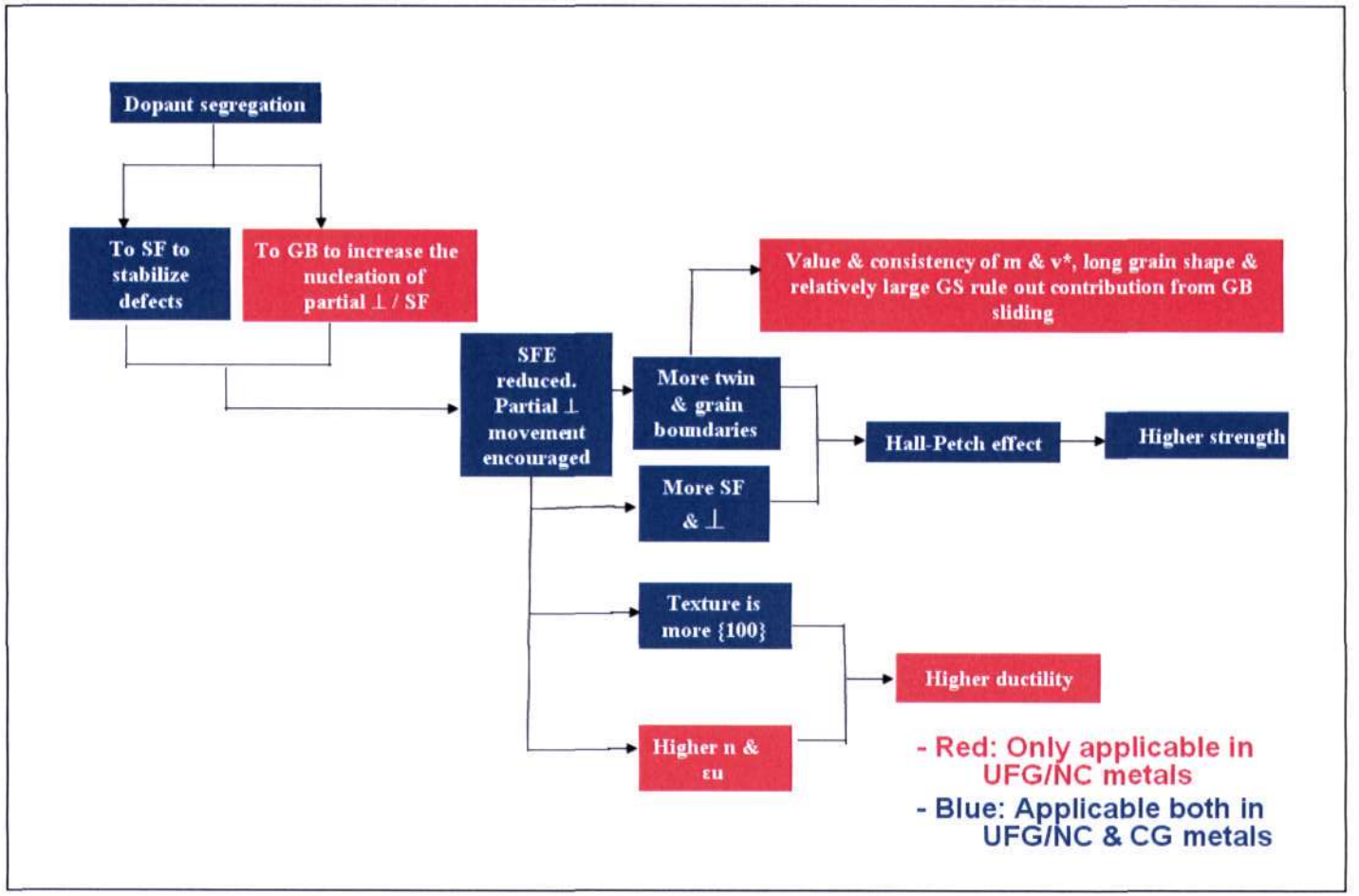

Figure 5-45 Summary of the working mechanism of Ca in Au wires. Red boxes are those that are applicable only in UFG/ NC materials but are not expected to operate in conventional CG materials.

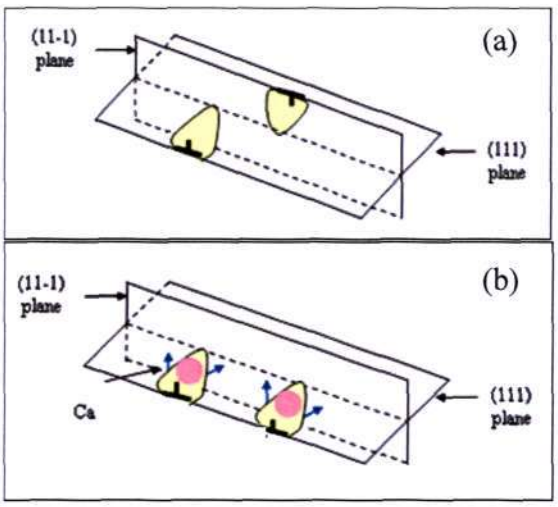

Fig. 5-46 (a) Dislocations traveling freely on {111} planes without Ca and (b) Pinning of partial dislocations by Ca, which dislocation can not cross-slip.

To conclude, the strengthening effect of Ca originates mainly from grain refinement, solid solution and dislocations/SF strengthening. The ductility improvement is a result of increased <100> texture which gives high Schmid factor, with also mild contribution from the suppression of plastic instability. All of the responsible microstructures have the common source of SFE reduction, which is induced by the strong segregation tendency of Ca.

5.8 Chapter Summary

To summarize, the objective of this chapter, i.e. to identify the working mechanism of Ca in Au wires has been achieved. Along with some findings that focus on the difference in behavior between CG and UFG/ NC metals, the summary is as follows:

1. The postulation that SFE of Au wires has been reduced by Ca is proven by statistical measurement of SFW and SF density measurement, the enclosing partial dislocations are identified as Shockley and Frank type. Also, observations on slip mode, dislocation distribution/density and texture further confirmed the SFE reduction.
2. Based on the prevalence of partial dislocations and twins, and that they are generated from the GB, this shows that PDMP has taken place. Our GS range of 100-500 nm is higher than the suggested boundary for PDMP, which is between 10 to 50 nm.
3. It is proposed that on top of dopant segregation to SF (as in CG metals), segregation to GB in UFG and NC metals could also enhance the effectiveness of SFE reduction. This is supported by the occurrence of localized, abundant partial dislocations and twins, some of which are generated from the GB ledge, even though we are not able to locate Ca in this work.
4. It is known that the effect of SFE is more pronounced at smaller GS, with the result that Ca has significantly larger effect on the mechanical properties of Au wires, even when present in the ppm level. This is demonstrated by comparing the

strengthening effect of doping between Au rod and UFG Au wires, in which the effect is 20 times larger in the latter. The results imply that the effectiveness of segregating dopant in reducing SFE can be used a strategy for the accomplishment of dual improvement in UFG/NC materials.

5. Strength improvement by Ca comes from abundant GB, twin boundaries, SF and solid solution. The ductility mainly originates from a favorable texture, which has higher average Schmid factor and is more conducive to deformation. Both of these microstructures have the common source of lower SFE. The predicted improvement from the respective mechanisms matches reasonably well with the experimental results.
6. When texture engineering is invoked, yield strength is usually sacrificed at the expense of ductility. This work is the first demonstration that by tailoring two simple parameters- grain size and orientation, simultaneous improvement in strength and ductility can be achieved.

Chapter 6

Dopant selection criteria for dual improvement in UFG Au wires

The ultimate objective of this project is to establish selection rules for dopants that can concurrently improve the ductility and strength of Au wires. The initial postulation that Ca can reduce the SFE of Au wires effectively has been proven in this work. Therefore the establishment of criteria should start from the impact of dopant on the SFE of materials. Based on the original mechanism, it is known that dopants that will preferentially segregate can reduce SFE effectively, therefore segregation tendency of dopant is the second consideration (Hirth, 1986). Third, dopants that segregate to GB may induce embrittlement or act as GB cohesion enhancer. Obviously, we would want to avoid the first scenario. Hence, the impact of dopant on the GB cohesion after segregation should also be taken into account (George, 1991).

6.1 Dopant Selection Criteria for Influencing Stacking Fault Energy

It is known that SFE of a metal is generally lowered by alloying, while the effectiveness of the solute will depend on the solid solubility and valency of the solute. A simple expression has been derived relating SFE and alloying concentration:

$$\ln \frac{SFE_{alloy}}{SFE_{solvent}} = \delta[\frac{c}{(1+c)}]^2 \qquad (6\text{-}1)$$

where $SFE_{solvent}$ represents the SFE of the pure metal (solvent) and SFE_{alloy} represents the SFE of the alloy, δ is a constant, and $c = x/ x'$, with x is defined as the solute concentration and x' the solid solubility limit at high temperature (Murr, 1975). From here, it can be seen that SFE of the base metal can be reduced more if the solid solubility of the solute is low in the metal. Second, it is also known that SFE reduction is more effective with elements of higher valency, i.e. having higher numbers of electrons in the outermost energy level of an atom (Reed-Hill, 1991).

Solid solubility itself can be influenced by several factors, as suggested by Hume-Rothery's and Darken-Gurry's Rules (Barrett and Massalski, 1966; Cahn, 1996,):

i) Differences in Atomic Sizes

If the difference between the atomic sizes of the component elements forming an alloy exceeds ~ 15%, solid solubility should become restricted. This is known as the 15% rule. It has been shown that when the size rule alone is applied, low solubility predicted is usually true, but the prediction of extensive solubility on the basis of small size difference is only 50% successful.

ii) Differences in Electronegativity

The likelihood of the formation of solid solution is related to the chemical affinity of the participating elements, and will decrease when the two elements have greater differences in electronegativity. The criteria is said to be 0.4.

iii) Differences in Valency

It was also suggested that solubility is related to their respective valencies, namely, that the amount of the solid solution in the element of lower valency is always greater. This is sometimes called the 'relative valency effect'. For example, Cu (univalent metal) will dissolve approximately 40% zinc (bivalent metal) in solid solution but the solution of copper in zinc is limited.

Therefore for the consideration of impact of dopant on SFE of metals, the parameters of concern are solid solubility, valency, size and electronegativity.

6.2 Dopants Criteria for Segregation Tendency

To have an indication of whether an element has the tendency to segregate, one needs to look at the segregation energy (E_{seg}) of the dopant. E_{seg} is the difference in binding energy at T = 0 K of a dopant atom at a GB/ SF site versus one at a bulk site (Schweinfest, 2004). As segregation energy is not available in the literature, we have used simulation method to deduce this parameter.

To deduce the segregation energy to GB ($E_{Seg\ GB}$) and SF ($E_{Seg\ SF}$), three modeling structures were built, namely the simple bulk Au structure, the GB and the SF structures, as shown in Fig. 6-1. On top of Ca, one of the common dopants, platinum (Pt) is also considered for comparison. For simplicity, idealized GB structure based on the coincidence site lattice (CSL) model (Chapter 3) was built (Murr, 1975). Data from our work as well as that from literature indicate that the misorientation angles of Au wires peak at ~5-10° and ~40-60° (Chapter 5; Cho, 2003). As segregation is favored at high angle, a GB with Σ= 5 (53.13°) [001] twist boundary is constructed. This boundary is formed by the rotation of 53° about [001] axis. For the SF structure, Frank partial dislocation was built, where the {111} plane is shifted by 0.236 nm (a/3<111>). The three structures were constructed as a 21-layer slab, and the dopant is placed at the center of the structure. Each crystal was geometrically optimized using COMPASS (Condensed phase Optimized Molecular Potential for Atomistic Simulation Studies), which is a molecular mechanical method. The Smart algorithm, which is a cascade of the Steepest Descent, ABNR (Adjusted basis set Newton–Raphson) and Quasi-Newton methods, was used in

the calculation. A force convergence of 4.336 E-5 eV was defined for the final structure. After the first level of geometry optimization, a finer ab initio geometry optimization was performed. Ab initio software named DMol3 from Acclerys was used. In the second stage, even more refined optimization with ab initio method was performed.

For more delicate calculation, cluster of smaller size was used. The GB and the SF clusters possess ~70 atoms, and the bulk contains ~100 atoms respectively. DMol3 uses an ab initio numerical method within the framework of density functional theory to evaluate the energy gradient of the structure. A frozen core approximation was applied to the inner atomic orbitals for Au and Pt atoms, such that only the orbitals beyond 5s were considered as the self-consistent valence orbitals and those below 5 s were taken as core orbitals. For Ca, they were treated as in all-electron case due to their much fewer numbers of electrons. The structure was firstly geometrically optimized with a looser criterion employing double numerical (DN) basis set. Convergences were set at 1E-4, 2.725E-3 eV, 0.545 eV/ Å and 0.05 Å for the self-consistent field density, energy, force and displacement respectively. After obtaining the structure, the final binding energy was calculated using a more refined calculation that employs the double numerical basis with polarized functions (DNP). Convergence was defined as achieved when a self-consistent field density difference of <1E-6 was reached during the optimization cycles. In both cases, the functional of the exchange correlation energy used was the Perdew-Wang generalized-gradient approximation (GGA).

The binding energies of six systems are compared: bulk Au with Ca/ Pt, Au SF with Ca/ Pt and Au GB with Ca/ Pt. Four E_{seg} are computed: E_{seg} of Ca to GB and SF; And E_{seg} of Pt to GB and SF. The results are shown in Table 6-1. A high E_{seg} shows that the dopants have high tendency to segregate to the site, to lower the energy of the system.

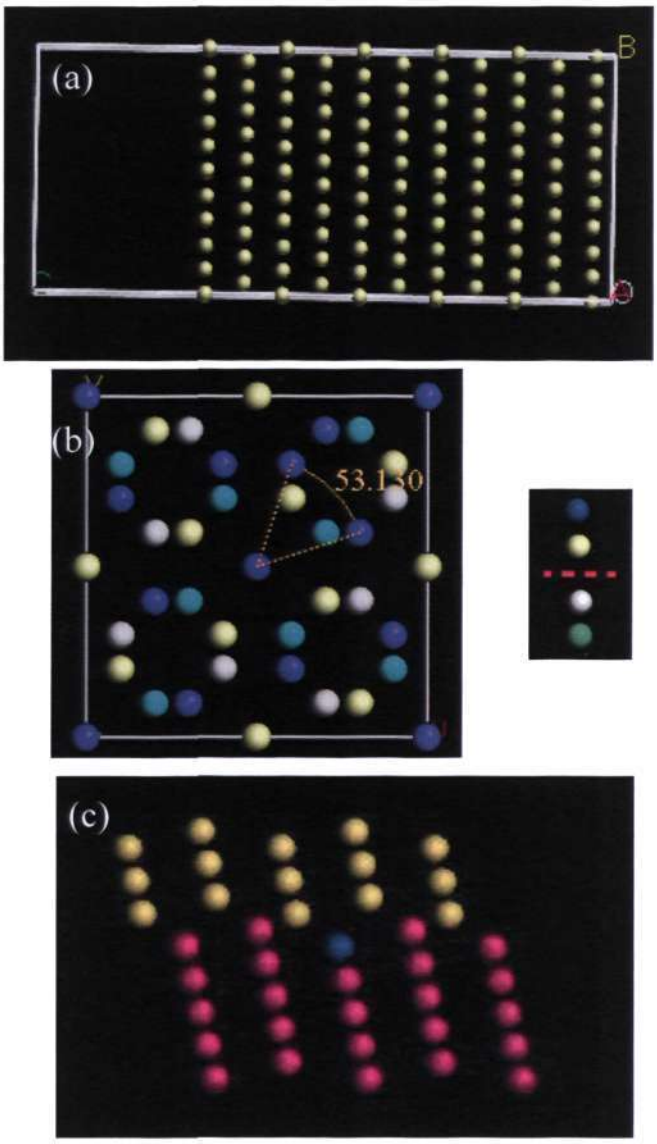

Figure 6-1 The atomic configuration of (a) An Au bulk structure; (b) An Au Σ =5 (53.13°) [001] twist boundary. Structures are shown in projection along [001] with two planes on either side of the boundary. The stacking sequence of planes is indicated on the right hand side and (c) Stacking fault that is formed by Frank partial dislocation, viewed from [110], with the blue atom being the dopant.

Table 6-1 Segregation energy of dopants at various sites

Eseg (kJ/mol)	Ca	Pt
To stacking faults	65	22
To grain boundaries	117	61

First, it is obvious that Ca has higher segregation tendency than Pt. This is in agreement with the theoretical prediction of GB segregation tendency of solute. The tendency for segregation increases as the size misfit between the solute and matrix increases, (i.e. when the solubility is low) and as the solute-solute bond strength decreases (Porter & Easterling, 1992). For example, solid solubility of Ca in Au is 1.8 at% (0.36 wt %) at ~800^{o}C while Pt is completely miscible in Au (Massalski, 1986). As for the second criterion, Ca-Ca has low bond strength of 46 kJ/ mol while Pt-Pt has strong bond strength of 357 kJ/ mol. The bond strength values taken are the bond enthalpy between gaseous diatomic species (Winter, 1993). Therefore Ca should have a high tendency for GB segregation than Pt. The E_{seg} for known segregating element is ~100 kJ/ mol. For example, sulphur which tends to segregate in nickel, has E_{seg} of 96 kJ/mol (Yin, 2005). Therefore Ca has very high chance to segregate to GB and SF. Second, it can be deduced that the chances of segregating to GB is higher than to SF, however this comparison is valid on a high angle GB only.

6.3 Dopants Criteria for Enhancing Grain Boundary Cohesion

Segregation of dopants can be beneficial or detrimental to the mechanical properties of the base materials, depending on their impact on GB cohesion (G_{coh}). For example, several studies have classified the effect of dopants on the fracture strength of alloy steels using simulation method (Fen, 2001). To our knowledge, no similar study has been conducted on Au bonding wire before. However, it is known that inappropriate dopant segregation can potentially cause intergranular fracture in Au wires (Kulicke, 2005), as shown in Fig. 6-2. It is also known that doping can increase the GB cohesion to bring up ductility, as in the well-known case of boron doping in ordered intermetallic compounds such as Ni_3Si (Subramanian, 1997). Therefore in this section, we will consider the impact of dopants on the GB cohesion of Au wires, after they segregate to the GB. Again, because this parameter is not available on the open literature, simulation was used as a mean to deduce the parameter. Rice &Wang theory (Rice & Wang, 1989) has given a simple criterion by which the effect of a dopant on GB cohesion could be predicted.

Based on Griffith's elastic fracture theory (Griffith, 1920), a classical theory in this field, Rice and Wang (Rice & Wang, 1989) described a distinction between brittle separation and crack tip blunting by dislocation emission, and this mechanism is widely thought to relate to whether a fracture will occur. If the ideal work, $2\gamma_{int}$, of interfacial

separation is less than the work of dislocation nucleation, G_{disl}, the interface is intrinsically cleavable; otherwise, the crack tip will become blunt and ductile crack propagation will occur.

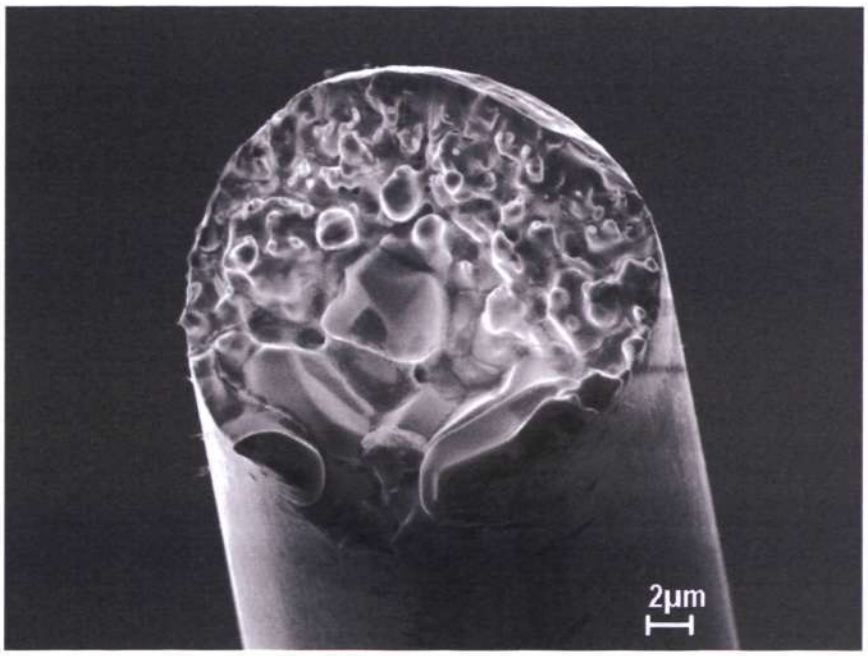

Figure 6-2 Intergranular fracture on experimental wires.

In their thermodynamic model, Rice & Wang have given a clear description of the effects of solute segregation on $2\gamma_{int}$, in spite of the uncertainty of G_{disl} caused by the dislocation complexities such as different slip orientations, local heterogeneity of plastic flow, etc. It was concluded that $2\gamma_{int}$ has a nearly linear relation with the difference (Δg_b-Δg_s) which results from decohesion of the GB:

$$2\gamma_{int} \approx (2\gamma_{int})_0 - (\Delta g_b - \Delta g_s)\Gamma \qquad (6\text{-}2)$$

The term $(2\gamma_{int})_0$ is the separation work of a clean interface, Γ is the solute coverage of the GB, Δg_b and Δg_s are the Gibbs free energy changes of the GB and the FS due to the presence of dopant. Using this equation, one can associate the brittle/ ductile effect of doping with the change of $2\gamma_{int}$ by the free energy difference. The vibrational and configurational entropy parts of the free energies are neglected and Δg_b and Δg_s are defined as the energies of segregation of the dopant to the GB and FS, ΔE_b and ΔE_s, respectively, which are defined as:

$$\Delta E_b = E(GB) - E(D/GB) + E(D_1) \qquad (6\text{-}3)$$

$$\Delta E_s = 1/2[E(FS) - E(D/FS)] + E(D_2) \qquad (6\text{-}4)$$

The terms E (GB), E (D/GB), E (FS) and E (D/FS) are the binding energies of the GB with and without the dopant and the binding energies of the free surface (FS) with and without the dopant, respectively. Terms E (D_1) and E (D_2) are the binding energies of a monolayer of dopant at GB and FS respectively. The factor of one half in Eq. 6-4 is to account for the two dopants added in the FS system. The relative tendency for a dopant to strengthen or embrittle GBs can be predicted by a key quantity called the strengthening energy, ΔE, which is defined as:

$$\Delta E \equiv \Delta E_b - \Delta E_s \qquad (6\text{-}5)$$

A negative value for ΔE denotes enhancement of GB cohesion and a positive value denotes embrittlement of the GB (Wu, 1996). Conceptually this can be understood as follows: a dopant which prefers to go to a FS of a crack (a crack is a FS within the material) can block material from flowing in to blunt the crack, and is therefore embrittling.

A long-standing question to be answered is how GB segregant induces either strengthening or embrittlement effects on the GB, i.e. if the GB cohesion is reduced, the material will become more brittle. Some studies have concluded that the embrittlement/strengthening tendency of segregant depends solely on the relative atomic radius of host and dopant and that the effect has a purely mechanical origin. For example, Schweinfest et al. has refuted an electronic hypothesis by showing that bismuth embrittles Cu by pushing the Cu atoms apart at the interface. The study compared the effects of bismuth and lead (which have similar atomic radius but different electronegativity), and the effects induced on the GB were indistinguishable (Schweinfest, 2004). On the other hand, some studies supported the view that the electronic interaction among the host and dopant is the main mechanism. The GB de-cohesion caused by sulfur (S) in nickel (Ni) was shown to be the result of a short-range repulsive interaction among S atoms in the GB region, which led to large GB expansion (Yamaguchi, 2005). Parameters that could be relevant are electronegativity, number of electrons and resulting spatial anisotropy of bonding (Wu, 1996). In most cases, it is believed that both electronic and geometry effects are crucial (Fen, 2001). In general, it is widely accepted that large segregants are detrimental as they tend to push the GB apart

and cause decohesion. Also, more electro-negative segregants can withdraw electrons, resulting in anisotropic bonding that weaken the bonds in planes perpendicular to the GB to act as a GB cohesion enhancer (Cahn, 1996). In this study, besides determining the effects of dopants on the cohesion of Au GB, the effects are also correlated to the size and electronegativity for the understanding of mechanism.

One additional structure, i.e. the FS of Au was built. The Au (110) FS was obtained by removing the upper half of the GB configuration, resulting in an 11-layer slab. Going into the stage of ab initio optimization, the FS clusters possess ~50 atoms. For the FS system, the dopant was placed pseudomorphically on the next Au sites on both sides of the slab. The rest of the computational details were kept the same as in the previous calculation for fair comparison. We have considered multiple dopants in this section, and the result is summarized in Table 6-2.

Following Ferro's work, we have classified the dopants based on their position on the periodic table (Ferro, 2003). The dopants considered in this study are: 1) Group 10 and 11 which are expected to have extensive solid solubility in Au; 2) Group 2 which is expected to have very limited solid solubility in Au; 3) Group 1 with low electronegativity and 4) Group 15 and 16 which are the typical impurities. These dopants are chosen because they are more commonly used or found in the manufacturing process of Au wires.

Table 6-2 Strengthening energy of various dopants with their atomic radius and electronegativity

Group	Elements	strengthening energy, ΔE	Metallic radius (Å)	Electronegativity
	Gold (Au)	-	1.46	2.54
Group 10, 11	Palladium (Pd)	-0.71	1.37	2.2
	Silver (Ag)	-0.74	1.44	1.93
	Platinum (Pt)	1.25	1.39	2.28
Group 2	Beryllium (Be)	-1.61	1.12	1.57
	Calcium (Ca)	-0.11	1.97	1
	Strontium (Sr)	1.41	2.15	0.95
	Barium (Ba)	2.68	2.22	0.89
Group 1	Lithium (Li)	0.05	1.55	0.98
	Potassium (K)	2.06	2.35	0.82
* Group 15, 16	Nitrogen (N)	-1.19	0.75	3.04
	Oxygen (O)	0.27	0.73	3.44
	Phosphorus (P)	-0.07	1.06	2.19
	Sulfur (S)	0.69	1.02	2.58

* For group 15 and 16, covalent radius were considered

The dopants that fall under Group 10 and 11 includes: palladium (Pd), platinum (Pt) and silver (Ag). These elements are very similar to Au in terms of their atomic radius and electronegativity. Also, all of them have FCC structure like Au. Therefore, this group of elements is believed to dissolve completely into Au matrix (Massalski, 1986), especially in the typical ppm range of doping in Au wire. They have the opportunities to

segregate to the GB, because there is abundant GB in the UFG Au wires. From Table 6-2, it can be observed that two out of three elements are GB enhancer, with Pd being the strongest (ΔE= -0.71). However, it is surprising that Pt is a GB embrittler. Based on the simulation results, it was predicted that the majority of Gp. 10 and 11 dopant would have a beneficial effect on the ductility of Au wires.

The second group of interest is Group 2 that includes: barium (Ba), strontium (Sr), calcium (Ca) and beryllium (Be). Among them, Be and Ca are very commonly applied in the doping of Au bonding wires, and are predicted to enhance GB cohesion. Be being 23% smaller than Au has a ΔE of –1.61, which is the highest among all the simulated elements. This value is also slightly higher, compared to ΔE values obtained in other studies. While Be and Ca are good for the GB, Sr and Ba seem to be very harmful to Au GB. This could be attributed to the size difference alone: Ba and Sr are 52% and 47% larger than Au atom. In these cases, the low electronegativities of Ba and Sr are not beneficial.

Group 1 is not so commonly used for doping Au wires, but their low electronegativity could have been beneficial. Only two elements, lithium (Li) and potassium (K) were used in simulated tests. Table 6-2 shows that both elements are GB embrittlers. The large size of K is probably responsible for the embrittlement effect, but the radius of Li is only ~6% different from Au. It is observed that all elements having electronegativity lower than 1 are GB embrittlers in Au, which includes Li, K, Ba and Sr.

Among them, the atomic radius of K, Ba and Sr are more than 45% bigger than Au. It is not conclusive whether the low electronegativity or the big atomic radius of the elements are responsible for the effects.

The last studied group including impurities from group 15 and 16, like phosphorus (P), sulfur (S), nitrogen (N) and oxygen (O). These impurities could be unintentionally introduced, especially during the manufacturing process. For this group of elements, covalent radius was considered. The impurities were added at the interstitial site in the simulation, instead of a substitution site as in other groups of elements. The radius of the octahedral and tetrahedral interstitial site of FCC Au structure is ~0.579 Å and 0.3 Å, respectively. The impurity elements considered here have slightly larger atomic radius than the interstitial site. However, these impurities are commonly assumed to occupy an interstitial site as reported in similar simulation studies, especially since more space is expected in the GB. Table 6-2 shows that N and P are predicted to have a ductilization effect on Au GB, while S and O are predicted to be embrittlers. It can be observed that N has a strong enhancing effect, with ΔE of -1.19. There was no similar study on Au which we can reference to. In Fe and tungsten (W), N has been predicted to be an enhancer (Fen, 2001) and an embrittler (Kim, 2004) by different groups. While P is a common embrittler in other systems (Fen, 2001), it is predicted to be an enhancer (ΔE = -0.07) in Au. Besides P, S is another common embrittler, which agrees with our results. Finally, O is simulated to be a neutral impurity, which does not influence GB cohesion in W (Grujicic, 1997), but it is predicted to be harmful in this study. In their work, the effect of solute segregation on dislocation evolution near the crack tip was considered, on top of

$2\gamma_{int}$. Instead of using ab initio simulation, the method employed was molecular dynamics.

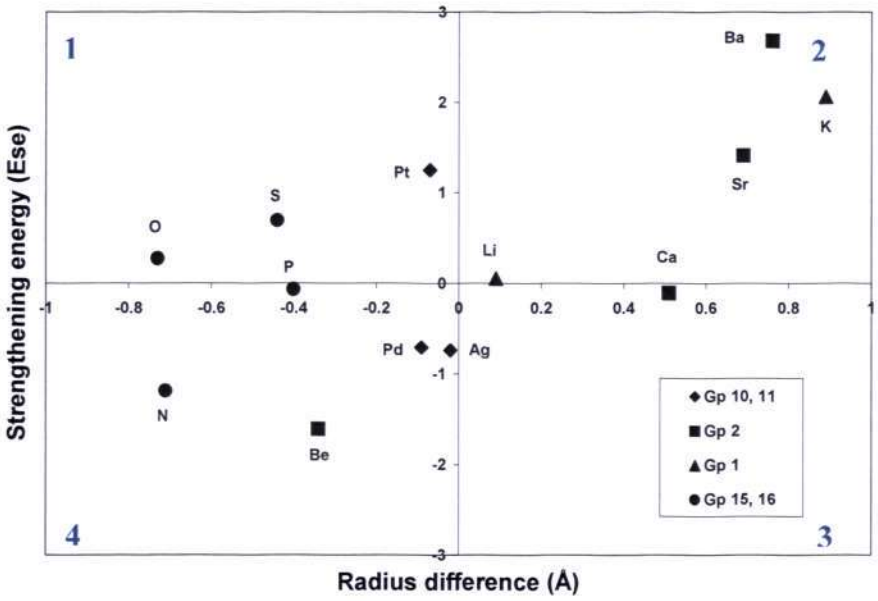

Figure 6-3 Strengthening energy as a function of radius difference between Au and various dopants. (r_{dopant}-r_{gold}). Those with a negative radius difference are dopants that are smaller than Au.

In Fig. 6-3, the strengthening energy is plotted as a function of radius difference between the dopant and Au (Δr). Those with a negative Δr are dopants with a smaller atomic radius than Au. The graph indicates that dopants that are smaller than Au are, in general, beneficial to Au (five dopants: P, Pd, Ag, Be and N) and only three elements (O, S, Pt) are predicted to be detrimental. Among them, the result of Pt is most surprising. It is clear that big-sized dopants are detrimental, as seen from those elements that are sitting in the second quadrant (Ba, K and Sr). This shows that, in general, the prediction is consistent with the view that big-sized dopants can reduce GB cohesion.

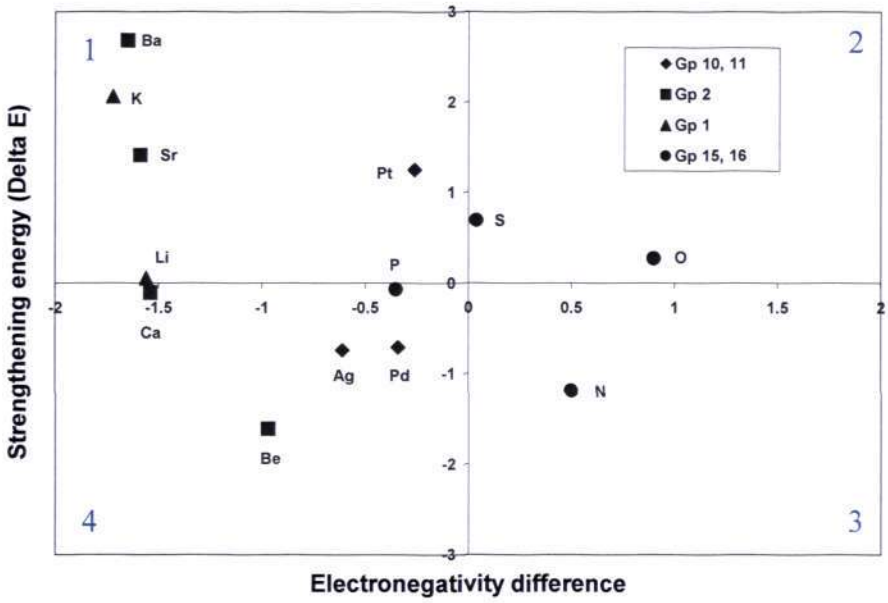

Figure 6-4 Strengthening energy as a function of electronegativity difference between Au and various dopants (n_{dopant}-n_{gold}). Those with a negative electronegativity difference are dopants with lower electronegativity than Au.

Fig. 6-4 compares the strengthening energy with the difference in electronegativity with Au (Δn). The more negative that Δn is, the less electronegative is the element than Au. Consistent with our expectation, elements with low electronegativity exert good effect on GB cohesion (Ca, P, Ag, Pd and Be). This is evident from the many points that fall into the fourth quadrant (negative ΔN, negative ΔE). However, quite a number of elements also seem to behave differently, even though they also posses low electronegativity (Ba, K, Sr, Pt and Li). Among them, it is highly possible that Ba, K and Sr gather the effect from their large misfit size. Therefore, it seems that the size effect dominates over the electronic effects in this case. This conclusion contradicts with what was reported by Shang et al. (Shang, 2001). They found

that the electronic and geometry effect have opposite roles in determining whether a dopant is embrittling or not, and that the chemical effect is dominant. Their study is also based on a first-principles DMol3 method like our study. Only three tested elements have electronegativity higher than Au. One is calculated to be enhancer (N) and two are embrittlers (O and S). However, electronegativity may not be the only parameter in dictating the chemical effects between the dopant and the matrix.

In summary, dopants having a smaller atomic radius and lower electronegativity than Au are more beneficial for Au GB cohesion. Therefore, these three parameters should be considered when establishing the criteria.

6.4 Establishment and Verification of Dopant Criteria on Dual Improvement in Au Wires

The above mentioned criteria are listed in Table 6-3. Besides Ca, platinum (Pt) and beryllium (Be) are also included for comparison (Pt and Be are also common dopants used in the wire bonding industry). Those properties that are highlighted in purple refer to the properties that have fulfilled the criteria. Out of the nine suggested criteria, Ca has satisfied seven of them. On the other hand, Pt which is known to have negligible impact on Au wire properties (at low concentration) does not fulfill any of the criteria (Kulicke, 2005). Therefore it has been demonstrated that the proposed criteria work well in these two examples. It can be seen from the SFE portion that the criteria converge to a requirement of dopant with low solid solubility. The applicability range of the suggested

criteria has the restriction of dopant concentration, i.e. the concentration must be below their solid solubility, above which precipitation should occur.

Table 6-3 Summary of properties with respect to the proposed criteria for dual improvement in Au wires

		Criteria	Ca	Be	Pt	Au
SFE	Solid solubility (at %)	The lower the better	1.8 @ 800 °C	0.2 @ 580 °C	complete solid solubility	N.A.
	Δ radius (%)	> 15%	35	-23	-6%	N.A.
	Δ electronegativity	> 0.4	-1.54	-0.97	-0.34	N.A.
	Crystal structure	Different	Same	Differ ent	Same	N.A.
	Valence	The higher the better	2	2	1	1
GB segregation	Segregation energy	The higher the better	117	87	61	N.A.
GB cohesion	Strengthening energy	The more negative the better	-0.11	-1.61	1.25	N.A.
	Radius (Å)	The smaller the better	1.97	1.12	1.39	1.46
	Electronegativity	The lower the better	1	1.57	2.28	2.54

Also, Be is noticed to fulfill all the criteria well. To examine the applicability of the model, Au wires were doped with Be to determine if the predicted concurrent strengthening and ductilization effect will be realized. Stress-strain curves of the two

wires with different levels of Be is shown in Fig. 6-5. As in the notation for Ca-doped Au wires, Au10Be and Au15Be refer to Au wires with 10 ppm Be and 15 ppm Be respectively. It is seen that with additional 5 ppm of Be, both ductility and strength of Au wires gets higher. This result is in agreement with a previous report, in which Brenner et al. have reported the beneficial effect of Be on both strength and ductility of Au wires in the 60's (Brenner, 1966).

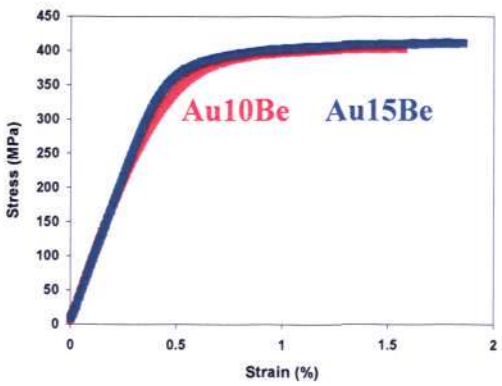

Figure 6-5 Engineering stress-strain curves of Be-doped Au wires.

Based on the results from the three tested dopants, the effectiveness of the proposed criteria has been demonstrated. Further work is in progress to verify the effect of other dopants on the mechanical properties of Au wires.

6.5 Chapter Summary

In this chapter, criteria on dopant selection for the realization of concurrent strength and ductility (dual) improvement in Au wires are proposed. The summary is as follows:

1. The more efficient is a dopant in reducing the stacking fault energy of Au wires, the more likely it could lead to dual improvement. The relevant parameters are solid solubility, the differences of radius and electronegativity with solvent, crystal structure and valency.
2. The more likely is a dopant in leaving the matrix and be segregated to areas like stacking faults and grain boundaries, the more likely it is for dual improvement to take place. Segregation energy gives an indication of the segregation tendency of the elements. As segregation energy is not available in the literature, the values are deduced using an ab initio simulation within the framework of density functional theory.
3. Upon segregation to the grain boundaries, it is important that the dopant induce desirable effect to the grain boundaries, instead of embrittling them. The impact of dopant on grain boundary cohesion is again investigated using ab initio calculation, based on thermodynamic model of Rice and Wang. The derived parameters of concern are the strengthening energy, and the absolute value of the radius and electronegativity of dopant.
4. The proposed criteria have been experimentally verified in three systems: gold-calcium, gold-beryllium and gold-platinum. Both calcium and beryllium have

fulfilled the criteria and were demonstrated to bring about the unique effect of simultaneously increasing the strength and ductility of Au wires.

Chapter 7

Conclusions and Suggested Future Work

7.1 Conclusions

The objective of this project, which is to establish dopant selection criteria for strength and ductility enhancement in Au wires at low dopant level, has been achieved. This is accomplished via the assessment on the effects and mechanisms of Ca in Au wires. The conclusions and original contributions from this thesis are summarized as below:

1. The addition of Ca progressively and consistently increases both strength and ductility of Au wires, by as high as 60% and 96% respectively. This intriguing effect has been demonstrated in as-drawn and annealed wires, and at five different strain rates.
2. Ca is also shown to retard high temperature creep rates of Au wires by ~4 to 6 times. The stress exponent (1-2), activation energy (~ 06-0.9 eV) and grain size (GS) exponent (3-4) obtained all point to a grain boundary (GB) diffusion mediated GB sliding creep mechanism. It is postulated that Ca could have segregated to the GB to impede the creep process.

3. Hall-Petch coefficient is increased by Ca addition, from 0.02 MPa• $m^{1/2}$ for Au20Ca to 0.06 MPa• $m^{1/2}$ for Au90Ca. As the coefficient reflects boundary properties, this implies that Ca could have segregated to the GB to encourage dislocation generation and strengthen the GB more effectively.
4. The postulation that SFE of Au wires has been reduced by Ca is proven directly by statistical measurement of stacking fault (SF) width and density. The partial dislocations enclosing SF are identified to be Shockley partial and Frank partial. Microstructure observations on slip mode, dislocation density/ distribution and texture have further supported this conclusion.
5. Based on the results obtained, potential mechanisms, such as plastic instability suppression, twinning-induced plasticity and GB sliding are ruled out. Strength improvement by Ca comes from abundant GB, twin boundaries, SF and solid solution. The ductility mainly originates from a favorable texture, which has higher average Schmid factor and is more conducive to deformation. Both of these microstructures are related to the common source of a lowered SFE. The magnitude of improvement predicted by these mechanisms also agrees reasonably well with the experimental results.
6. When texture engineering is invoked, yield strength is usually sacrificed at the expense of ductility. This work is the first demonstration that by tailoring two simple parameters- grain size and orientation, simultaneous improvement in strength and ductility can be achieved.
7. The results on creep and Hall-Petch coefficient are very strong evidence to show that GB segregation of Ca has occurred, to explain for the obvious impact

observed from low level dopant. Also, the results agree with the high segregation tendency of Ca, as predicted by ab initio simulation. The segregation energy obtained is comparable to the segregation energy of known segregating systems. However, Ca is not identifiable with either EDX or EELS in current work due to the extremely low dopant concentration, as expected from the scarcity of direct evidence in the field.

8. It is observed that partial dislocation mediated process (PDMP) has taken place, even though the GS range of 100-500 nm in this work is higher than the reported boundary for PDMP, which is between 10 to 50 nm. Also, there are localized, abundant partial dislocations and twins, some originating from GB ledges. Based on this observation, it is proposed that on top of dopant segregation to SF (as in the case of coarse-grained (CG) metals), segregation to GB in UFG and NC metals could also enhance the effectiveness of SFE reduction. This double effect will lead to efficient SFE reduction with segregating dopants in UFG/ NC metals.
9. As segregating elements affect SFE more prominently at finer GS, and the effect of SFE is more pronounced in UFG/ NC metals than in CG, the result is that Ca has a disproportionately larger effect on the mechanical properties of Au wires at low concentration. It is seen that the effect of doping on strength is ~ 20 times more in UFG Au wires, compared to Au rod. The results imply that the effectiveness of segregating dopant in reducing SFE can be used as a strategy for the accomplishment of dual improvement in UFG/ NC materials.
10. Based on this learning, three relevant areas for the formulation of criteria are the impact of dopants on SFE, segregation tendency and GB cohesion. The more

efficient is a dopant in reducing the SFE of Au wires, the more likely it can lead to dual improvement. The relevant parameters are solid solubility, the differences of radius and electronegativity with solvent, crystal structure and valency.

11. Second, the more likely is a dopant in leaving the matrix and be segregated to areas like SF and GB, the more likely it is for dual improvement to take place. Segregation energy gives an indication on the segregation tendency of the elements. As segregation energy is not available in the literature, the values are deduced using ab initio simulation within the framework of density functional theory.
12. Lastly, upon segregation to the grain boundaries, it is important that the dopant induces desirable effect to the GB, instead of embrittling them. The impact of dopant on GB cohesion is again investigated using ab initio calculation, based on the thermodynamic model of Rice and Wang. The parameters of concerned are the strengthening energy, and the absolute value of the radius and electronegativity of dopant.
13. The proposed criteria have been experimentally verified in two additional systems: gold-beryllium and gold-platinum. Both calcium and beryllium have fulfilled the criteria and were demonstrated to bring about the unique effect of simultaneously increasing the strength and ductility of Au wires, in agreement with published patents. Platinum on the other hand, does not conform to the guidelines, and it shows insignificant impact on wire properties at the ppm level. These criteria are limited to dopant concentration below the solid solubility limit, and shall be especially applicable for UFG/ NC system.

In summary, the initial objective of this project, i.e. to propose dopant selection criteria for dual improvement in Au wires, has been successfully achieved and verified. This is a significant first step to bring wire manufacturer a step closer to the successful implementation of ultrafine pitch bonding, by overcoming the first hurdle- the stringent requirement on both high strength and ductility for manufacturability. The established criteria also serve as a basis for the categorization of dopants and for the set up of a 'dopant library' for Au wire. On the other hand, this work has also demonstrated the effectiveness of segregating dopant on inducing dual improvement in UFG and NC metals, compared to their CG counterpart. This suggests that the potential impact of dilute alloying on the properties of UFG/ NC metals, much overlooked in modern metallurgy, could well be an effective development strategy for continual improvement.

7.2 Suggested Future Work

The findings in this work have established several promising directions for further work to be built upon. The work can be geared towards engineering consideration, i.e. from the perspective of wire manufacturer. Or, some ideas stemming from this work can be applicable in the study of UFG and NC metals. It is recommended that future work can be performed as summarized here:

1. The suggested criteria is targeted on the impact of dopant on mechanical properties of Au wires, which as discussed, is the first problem faced in the making of wires. To build a more

comprehensive 'dopant library', other factors, such as the effect of dopants on device reliability, bondability, looping performance etc have to be considered as well.

2. Similar approaches can also be extended to other wire types, such as copper wires and aluminum wires. This is especially true for copper wires, which is gaining popularity due to its much lower cost compared to Au wires. One of the major problems with copper wires is with its high hardness which translates into poor bondability, that the problem could be addressed by alloying.
3. The locations of Ca have not been directly identified in this work. It is suggested to ascertain the highest dopant concentration that can be dissolved in Au. And EELS and EDX should be conducted on this sample, at the areas with abundant stacking faults, twins and GB, especially the GB which twins are observed to be nucleated from.
4. Systematic comparison of effect of segregating dopant between UFG/ NC and CG metals shall be interesting, that the SFE and mechanical properties can be studied.
5. Current system focuses on binary systems only. The interaction effect of multi component doping can be studies, which positive impact might be derived from these systems.

6. The effect of nano-twin in Au wires and Cu wires may be pursued, especially this is currently a very hot topic in the study of mechanical properties of nano crystalline materials.

Chapter 8

References

Aernoudt, E., Houtte, P. V. & Leffers, T. (1993). *Plastic deformation and fracture of materials.* Weinheim: VCH publisher, p.90, Ch. 6, deformation and textures of metals at large strains.

Afanasyev, V. (1981). *Recrystallization in metals and alloys*. Moscow: MIR Publisher.

Agnew, S. R., Horton, J. A., Lillo, T. M. & Brown, D. W. (2004). Enhanced ductility in strongly textured magnesium produced by equal channel angular processing. *Scripta Materialia*, 50, 377-381.

Ahlborn, H. & Wassermann, G. (1963). EinfluB von Verformungsgrad und- temperatur auf die Textur von Silberdrahten. *Z. Metallk*, 54, 1-6.

Asaro, R.J., Krysl, P., Kad, B. (2003). Deformation mechanism transitions in nanoscale fcc metals. *Philosophical Magazine Letter*, 83, 733–743.

Asaro, R. J. & Subra, S. (2005). Mechanistic models for the activation volume and strain rate sensitivity in metals with nanocrystalline grains and nano-scale twins. *Acta Materialia*, 53, 3369-3382.

ASTM. (1996). *American Society for Testing and Materials: Standard Methods of Testing Fine Round and Flat Wire for Electron Devices and Lamps*, F 219, December 10, 1996.

Baker, I., Nagpal, P., Liu, F. & Munroe, P. R. (1991). The effect of grain size on the yield strength of FeAl and NiAl. *Acta Metallurgical et Materialia*, 39, 1637-1644.

Balzar, D., Ledbetter, H., Stephens, P. W., Park, E. T. & Routbort, J. L. (1999). Dislocation-density changes upon poling of polycrystalline $BaTiO_3$. *Physical Review B*, 59, 3414-3420.

Barrett, C. S. & Massalski, T. B. (1966). *Structure of metals*. U. S. A.: McGraw-Hill.

Birringer, R., Gleiter, H., Klein, H.-P., Marquardt. (1984). Nanocrystalline materials: an approach to a novel solid structure with gas-like disorder. *Physics Letters*, 102A, 365–369.

Blochwitz, C., Brechbiihl, J., Tirschler, W. (1996). Analysis of activated slip systems in fatigued nickel polycrystals using the EBSD-technique in the scanning electron microscope. *Materials Science and Engineering A*. 210, 42-47.

Bosco, E., Enz, S., Baricco, M. (2003). X-ray analysis of microstructure in Au-Fe melt spun alloys. *Journal of magnetism and magnetic materials*. 262, 136-141.

Brenner, B. (1966). Berryllium-gold alloy and article made therefrom. *United States Patent Office*, 3,272, 625.

Budrovic, Z, Swygenhoven, V. H, Derlet, P.M., Petegem, V. S., Schmitt, B. (2004). Plastic deformation with reversible peak broadening in nanocrystalline nickel. *Science*, 304, 273–276.

Caballero, V., Varma, S. K. (1999). Effect of stacking fault energy and strain rate on the microstructural evolution during room temperature tensile testing in Cu and Cu-Al dilute alloys. Journal of Materials Science, 34, 461-468.

Cai, B., Kong, Q. P. Cui, P., Lu, L. & Lu, K. (2001). Creep behavior of cold-rolled nanocrystalline pure copper. *Scripta Materialia*, 45, 1407-1413.

Cahn, R. W. & Haasen, P. (Ed.) (1996). *Physical Metallurgy*. Netherlands: North-Holland.

Carter, D. H. (2000). Deformation of a Aluminium-Berryllium composite [On-line]. Available: www.osti.gov/bridge/servlets/purl/752672eArWQ2/webviewable/752672.PDF

Castro, S. F., Gallego, J., Landgraf, F.J. G. & Kestenbach, H. J. (2006). *Orientation dependence of stored energy of cold work in semi-processed electrical steels after temper rolling*. Materials Science and Engineering A, 427, 301-305.

Chen, M. W. Ma, E., Hemker, K. J., Sheng, H. W., Wang, Y. M. & Cheng, X. M. (2003). Deformation twinning in nanocrystalline aluminium. *Science*, 300, 1275.

Cheo, K. H., Sritharan, T. (2004). *Recrystallization of Gold Bonding Wire*. Final year project report.

Cheng, S., Spencer, J. A., Milligan, W. W. (2003). Strength and tension/compression asymmetry in nanostructured and ultrafine-grain metals. *Acta Materialia*, 51, 4505–4518.

Chew, Y. H., Wong, C. C., Breach, C. D., Wulff, F., Mhaisalkar, S. G., Pang, C. I. & Saraswati. (2004). Effects of calcium and palladium on mechanical properties and stored energy of hard-drawn gold bonding wire. *Thin Solid Films*, 462–463, 346– 350.

Chew, Y. H., Wong, C.C., Breach, C. D, Wulff F. & Mhaisalkar S. (2006a). Effects of calcium on the mechanical properties of ultra-fine grained gold wires. *Journal of Alloys and Compounds,* 415, 193–197.

Chew, Y. H., Wong, C.C., Breach, C., Wulff, F., Mhaisalkar, S. (2006b). Doping-induced simultaneous improvement of strength and ductility in ultrafine grained gold wires. *Journal of Materials Research*, 21, 2345-2353.

Chew, Y. H., Wong, C.C., Wulff, F., Lim, F.C. & Goh, H.M. (2008). Strain rate sensitivity and Hall–Petch behavior of ultrafine-grained gold wires. *Thin Solid Film*, 516, 5376-5380.

Chew, Y. H., Ferraris, C. , Hui, H. K., Wong, C. C. (2008). Simultaneous Improvement of Ductility and Strength by Minute Doping in Ultrafine Grained Au Wires-experiment and First Principle Study. In: *2007 MRS Spring Meeting, San Francisco, CA (USA).*

Cho, J., Chong, M. W., Chan, H. M., Rickman, J. M. & Harmer, M. P. J. (2001). Improved tensile creep properties of yttrium- and lanthanum-doped alumina: a solid solution effect. *Journal of Materials Research*, 16, 425-429.

Cho, J. H., Cho, J. S., Moon, J. T., Lee, J., Cho, Y.H., Rollett, A. D., Oh, K. H. (2002). Characterization of cold drawn gold bonding wire with EBSD. *Material Science Forum Vols*. 408-412, 499-504.

Cho, J. H., Rollett, A. D., Cho, J. S., Park, Y. J., Park, S. H., Oh, K. H. (2006). Investigation on cold drawn gold bonding wire with serial and reverse-direction drawing. *Materials Science and Engineering A*. 432, 202-215.

Conrad, H., Narayan, J. (2002). Mechanisms for grain size hardening and softening in Zn. *Acta Materialia.* 50**,** 5067-5078.

Corti, C. W. (1999). Metallurgy of Microalloyed 24 Carat Golds. Gold Bulletin, 32, 39-47.

Courtney T. H. (2000). *Mechanical behavior of materials*. Singapore: McGraw-Hill. Ch.

Clarebrough, L. M., Hargreaves, M. E., Michael, D., West, G. W. (1952). The determination of the energy stored in a metal during plastic deformation. *Proceeding of Royal Society of London, Series A, Mathematical and Physical Sciences*, 215, 507-524.

Cullity, B. D. (1967). *Elements of X-ray Diffraction,* Addison-Wesley, U. S.A.

Dao, M., Lu, L., Shen, Y. F., Suresh, S. (2006). Strength, strain-rate sensitivity and ductility of copper with nanoscale twins. *Acta Materialia*, 54, 5421–5432.

Dao, M., Lu, L., Asaro, R. J., Hosson, J. T. M. D., Ma, E. (2007). Towards a quantitative understanding of mechanical behavior of nanocrystalline metals. *Acta Materialia,* 55, 4041-4065.

Dieter, G. E. (1986). *Mechanical metallurgy,* (pp.290, 308). 3rd ed. Boston (MA): McGraw-Hill.

Ebrahimi, F., Ahmed, Z. & Li, H. (2004). Effect of stacking fault energy on plastic deformation of nanocrystalline face-centered cubic metals. *Applied Physics Letters,* 85, 3749-3751.

Edington, J. W. (1975). *Practical Electron Microscopy in Materials Science*, Macmillan Philips Technical Library.

EELS in the TEM (2006). EELS in TEM [On-line]. Available: http://laser.phys.ualberta.ca/~egerton/preprint/JesRevRF.doc

Emery, R. D. & Povirk, G. L. (2003). Tensile behavior of free-standing gold films. Part I. Coarse-grained films. *Acta Materialia*, 51, 2067-2078.

Emery, R. D. & Povirk, G. L. (2003). Tensile behavior of free-standing gold films. Part II. Finegrained films. *Acta Materialia*, 51 (2003) 2079-2087.

Engler, O. (2000). Deformation and texture of copper-manganese alloys. *Acta Materialia*, 48, 4827-4840.

English, A. T. & Chin, G. Y. (1965). On the variation of wire texture with stacking fault energy in FCC metals and alloys. *Acta Metallurgical*, 13, 1013-1016.

Erb U. (2004). In: The 7th international conference on nanostructured materials (NANO' 2004), Wiesbaden, Germany.

Erb, U. (1995). Electrodeposited nanocrystals: Synthesis, properties and industrial applications. *Nanostructured Materials*,6, 533–538.

Fen, Y. Q. & Chong, Y. W. (2001). Electronic e€ects of nitrogen and phosphorus on iron grain boundary cohesion. *Computational Materials Science*, 20, 48-56.

Ferraris, C. (2007). *Notes on Transmission Electron Microscopy Immersion Course*. Nanyang Technological University, Singapore.

Ferro, R, Saccone, A., Macciò, D., Delfino, S. (2003). A survey of gold intermetallic chemistry. *Gold Bulletin*, 36, 39-50.

Fundamentals of Wire Bonding Process [On-line]. Available: http://www.TechStar-i.com.

Furukawa, M., Horita, Z., Nemoto, M., Valiev, R. Z., Langdon, T. G. (1997). Factors influencing the flow and hardness of materials with ultrafine grain sizes. *Philosophical Magazine A*, 78, 203-215.

Gallo, A.A. (2004). Green molding compounds for high temperature automotive applications**.** *Business of Electronic Product Reliability and Liability, 2004 International Conference*, Apr 27-30, 57-61.

George, E. P., White, C. L. & Horton, J. A. (1991). Grain boundary cohesion and fracture in ordered intermetallics. *Scripta Matellurgical et Materialia*, 25, 1259-1264.

Gertsman, V. Y., Hoffmann, M., Gleiter, H. & Birringer, R. (1993). The study of grain size dependence of yield stress of copper for a wide grain size range. *Acta Metallurgical et Materialia*, 42, 3539-3544.

Gleiter, H. (2000). Nanostructured materials: basic concepts and microstructure. *Acta Materialia*, 48, 1-29.

Gorelik, S. S. (1981). *Recrystallization in metals and alloys*, Moscow: MIR Publisher.

Griffith, A. A. (1920). The phenomena of rupture and flow in solids. *Philosophical Transactions of the Royal Society of London. Series A*, 221,163-198.

Grujicic, M. & Zhao, H. (1997). Atomistic simulation of S (111) grain boundary fracture in Tungsten containing various impurities on fracture. *International Journal of Refractory Metals & Hard Materials*, 15, 341-355.

Gupta, D. & Rosenberg, R. (1975). Effect of a solute addition (Ta) on low temperature self-diffusion processes in gold. *Thin Solid Film*, 25, 171-180.

Han, G. W., Jones, I. P. , Smallman, R. E. (2003). Direct evidence for Suzuki segregation and Cottrell pinning in MP159 superalloy obtained by FEG(S)TEM/EDX. *Acta Materialia*, 51, 2731–2742.

Hannula, S. P., Wanagel, J. & Li, C. Y. (1984). Evaluation of Mechanical Properties of Thin Wires for Electrical Interconnections. *IEEE Transactions on Components, Hybrids and Manufacturing Technology,* CHMT-6, 494-502.

Hansen, N. (2004). Hall-Petch relation and boundary strengthening. *Scripta Materialia*, 51, 801-806.

Hayes, R. W. , Witkin, D. Zhou, F. and Lavernia, E. J. (2004). Deformation and activation volumes of cryomilled ultrafine-grained aluminium. *Acta Materialia.* 52, 4259-4271.

He, G., Eckert, J. Loser, W. and Schultz, L. (2003) Novel Ti-base nanostructure–dendrite composite with enhanced plasticity. *Nature Materials*. 2, 33-37.

Heizmann, J. J., Montesin, T., Vadon, A. (1994). Circular texture in thin wires. *Materials Science Forum Vol.* 157-162, 701-708.

Herklotz, G., Schrapler, L., Simons, C., Reuel, J. & Cho, Y. C. (2001). U.S. Patent No 6,242,106 B1.

Hertzberg, R. W. (1996), *Deformation and fracture mechanics of engineering materials* , New York: John Wiley & Sons.

Hirsch, P., Howie, A., Nicholson, R. B., Pashley, D. W. and Whelan, M. J. (1977), *Electron microscopy of thin crystals* (pp. 428). New York: Robert Krieger.

Hirsch, J. & Lucke, K. (1988). Overview no. 76: Mechanism of deformation and development of rolling textures in polycrystalline FCC metals-II. Simulation and

interpretation of experiments on the basis of Taylor-type theories. *Acta Metallurgical*, 36, 2863-2882.

Hirth, J.P. & Lothe, J. Theory of dislocations. New York: McGraw-Hill; 1968.

Hong, S. I. & Laird, C. (1990). Mechanisms of slip mode modification in F. C. C. solis solutions. *Acta Mettalurgical Materialia*, 38, 1581-1594.

Hosoda, N., Tanaka, M. Mori, T. U.S. Patent No. 4,885,135, 5 Dec 1989.

Huang, C.X., Wang, K., Wu, S.D., Zhang, Z.F., Li, G.Y. & Li, S. X. (2006). Deformation twinning in polycrystalline copper at room temperature and low strain rate. *Acta Materialia*, 54, 655–665.

Huang, C. X., Wu, S. D., Li, S. X. & Zhang, Z. F. (2008). Strain hardening behavior of ultrafine-grained Cu by analyzing the tesile stress-strain curve. *Advanced Engineering Materials*, 10, 434-438.

Hull, D., Bacon, D.J. (2001). *Introduction to Dislocations*, 4th edn. UK: Butterworth-Heinemann.

Humphreys, F. J. (2001). Review: Grain and subgrain characterization by electron backscatter diffraction. *Journal of Materials Science*, 36, 3833-3854.

Humphreys, F. J., Hatherly, M. 2nd ed. (2004). *Recrystallization and related annealing phenomena*, London: Elsevier.

Kamino, T., Ueki, Y., Hamajima, H., Sasaki, K., Kuroda, K. & Saka, H. (1992). Direct evidence for Suzuki segregation obtained by high-resolution analytical electron microscopy. *Philosophical Magazine Letters*, 66, 27–31.

Kang, D. W. (1999). U.S. Patent No. 5,993,735, 30 Nov. 1999.

Ke, M., Hackney, S. A., Milligan, W. W. & Aifantis, E. C. (1995). Observation and measurement of grain rotation and plastic strain in nanostructured metal thin films. *Nanostructured Materials*, 5, 689-697.

Kitamura, O. (1999). U.S. Patent No. 5,989,364, 23 Nov 1999.

Kim, H. S., Extrin, Y. (2001). Ductility of ultrafine grained copper. *Applied Physics Letters*, 79, 4115-4117.

Kim, M., Geller, C. B. & Freeman, A. J. (2004). The effect of interstitial N on grain boundary cohesive strength in Fe. *Scripta Materialia*, 50, 1341-1343.

Klug, H.P. & Alexander, L.E. (1974). X-Ray Diffraction Procedures for Polycrystalline and Amorphous Materials. New York: John Wiley & Sons, Inc.

Koch, C.C., Morris D.G., Lu K., Inoue A. (1999). Ductility of nanostructured materials, *MRS bulletin*. 24, 54-58.

Koch, C. C. (2003). Optimization of strength and ductility in nanocrystalline and ultrafine grained metals. *Scripta Materialia*, 49, 657-662.

Koch, C. C., (2007). Structural nanocrystalline materials: an overview. *Journal of Materials Science*. 42, 1403-1414.

Krill, C.E. & Birringer, R. (1998). Estimating Grain-size Distribution in Nanocrystalline Materials from X-ray Diffraction Profile Analysis, *Philosophical Magazine A*. 77, 621-640.

Kulicke & Soffa (Pte Ltd), internal report, 2005.

Kumar, K. S., Suresh, S., Chisholm, M. F., Horton, J. A. & Wang, P. (2003). Deformation of electrodeposited nanocrystalline nickel. *Acta Materialia*. 51, 387–405.

Li, H. & Ebrahimmi F. (2004). Transition of deformation and fracture behaviors in nanostructured face-centered-cubic metals. *Applied Physics Letters*, 84, 4307 –4309.

Li, H., Choo, H. & Liaw, P. (2007). The effect of temperature on strain rate sensitivity in a nanocrystalline Ni-Fe alloy. *Journal of Applied Physics*, 101, 063536-1 – 063536-7.

Liao, X. Z., Zhou,F., Lavernia, E. J., Srinivasan, S. G., Baskes, M. I., He, D. W. & Zhu, Y. T. (2003). Deformation mechanism in nanocrystalline Al: partial dislocation slip. *Applied Physics Letters.*83, 632-634.

Liao, X. Z., Srinivasan, S. G., Zhao, Y. H., Baskes, M. I. & Zhu, Y. T., Zhou, F., Lavernia, E. J. & Xu, H. F. (2004). Formation mechanism of wide stacking faults in nanocrystalline Al. *Applied Physics Letters.* 84, 3564-3566.

Liao, X. Z., Zhao, Y. H., Srinivasan, S. G., Zhu, Y. T., Valiev, R. Z. & Gunderov, D. V. (2004a). Deformation twinning in nanocrystalline copper at room temperature and low strain rate. *Applied Physics Letters*, 84, 592-594.

Liu, F. & Kirchheim, R. (2004). Nano-scale grain growth inhibited by reducing grain boundary energy through solute segregation. *Journal of Crystal Growth*, 264, 385-391.

Lu, L., Li, S. X. & Lu, K. (2001a). An abnormal strain rate effect on tensile behavior in nanocrystalline copper. *Scripta Materialia*, 45, 1163-1169.

Lu, L., Shen, Y. F., Chen, X. H., Qian, L. H., Lu, K. (2004). Ultrahigh Strength and High Electrical Conductivity in Copper. *Science,* 304, 422- 426.

Lu, Yulin & Liaw, P. K. (2001b). The mechanical properties of nanostructured materials. *Journal of Materials*, 53, 31-35.

Ma, E., Wang, Y. M., Lu, Q. H., Sui, M. L., Lu,L. & Lu, K. (2004). Strain hardening and large tensile elongation in ultrahigh-strength nano-twinned copper, 85, 4932-4934.

Ma, E. (2003). Instabilities and ductility of nanocrystalline and ultrafine-grained metals. *Scripta Materialia*, 49, 663-668.

Ma, E. (2006). Eight routes to improve the tensile ductility of bulk nanostructured metals and alloys. *Journal of Materials*, 58, 49-53.

Mackenzie, J. K. (1958). Second paper on statistics associated with the random disorientation of cubes. *Biometrika*, 45, 229-240.

Martin, J. W. & Doherty, R. D. (1980). *Stability of Microstructure in Metallic Systems*, Great Britain: Cambridge University Press.

Massalski, T. B. (ed.) (1986) *Binary Alloy Phase Diagram, American Society for Metals*, Ohio: Metal Park.

Milligan, W. W., Hackney, S. A., Ke, M. & Aifantis, E. C. (1993). In situ studies of deformation and fracture in nanophase materials. *Nanostructured Materials*. 2, 267-276.

Mishra, R. K., Gupta, A. K., Rao, P. R., Sachdev, A. K., Kumar, A. M. & Luo, A. A. (2008). Infleunec of Cerium on the texture and ductility of magnesium extrusions. *Scripta Materialia*, 59, 562-565.

Mendis, B. G., Jones, I. P. & Smallman, R. E.(2004). Suzuki segregation in a binary Cu-Si alloy. *Journal of electron microscopy*, 53, 311-323.

Mohamed, F. A. (2003). A dislocation model for the minimum grain size obtainable by milling. *Acta Materialia*, 51, 4107-4119.

Mukai, T., Yamanoi, M., Watanabe, H. & Higashi, K. (2001). Ductility enhancement in AZ31 magnesium alloy by controlling its grain structure. *Scripta Materialia,* 45, 89-94.

Montesin, T., Heizmann, J.J. (1992). Evolution of crystallographic texture in thin wires. *Journal of Applied Crystallography,* 25, 665-673.

Murr, L. E. (1975). *Interfacial phenomenon in metals and alloys*. Canada: Addison-Wesley, p. 131, 152.

Nie, X. , Wang, E., Ye, Y., Zhou, Y. and Wang, D. (1995). Calculations of stacking fault energy for fcc metals and their alloys based on an improved embedded-atom method. *Solid State Communications*, 96, 729-734.

Nieh, T.G., Wadsworth, J. (1991). Hall–Petch relation in nanocrystalline solids. *Scripta Metallagical*, 25, 955–958.

Ning, Y. T. (2001). Alloying and Strengthening of Gold via Rare Earth Metal Additions. *Gold Bulletin*, 34, 77-87.

Noguchi, K., Araki, M., Ohno, Y., (2000). The preparation of transmission electron microscopy specimens of as-drawn gold wire. *Scripta Materialia*, 43, 199-204.

Porter, D. A. & Easterling, K. E. (1992). *Phase Transformations in Metals and Alloys, 2nd edition*. USA: Chapman & Hall.

Prasad S. K., (2004). *Advanced wirebond interconnection technology*. USA: Kluwer Academic Publishers.

Qian, L. H., Wang, S. C., Zhao, Y. H. & Lu, K. (2002). Microstrain effect on thermal properties of nanocrystalline Cu. *Acta Materialia*, 50, 3425-3434.

Randle, V. (1997). *Guide book series: electron backscatter diffraction*. UK: Oxford.

Reed-Hill, R. E. (1991). *Physical Metallurgy Principle 3rd ed.* Boston: PWS-KENT Publishing Company, p. 137.

Rice, J. R. & Wang, J. S. (1989). Embrittlement of interfaces by solute segregation. *Materials Science and Engineering A*, 107, 23-40.

Rohatgi, A., Vecchio, K. S., Gray, G. T., (2001). The influence of stacking fault energy on the mechanical behavior of Cu and Cu-Al alloys: Deformation twinning, work

hardening, and dynamic recovery. *Metallurgical and materials transactions A*, 32, 135-145.

Rohatgi, A. & Vecchio, K. S. (2002). The variation of dislocation density as a function of the stacking fault energy in shock-deformed FCC materials. *Materials Science and Engineering A*, 328, 256-266.

Rollett, A. D. (2005). *Texture Components and Euler Angles: part 2* [On-line]. *Available:*neon.materials.cmu.edu/rollett/27750.old.Spg05/Components_pt2_13Jan05_v2.ppt –

Rosenberg, Y., Machavariani, V.S., Voronel, A., Garber, S., Rubshtein, A., Frenkel, A.I. & Stern, E.A. (2000). Strain energy density in the X-Ray powder diffraction from mixed crystals and alloys, *Journal of Physics: Condensed Matters.* 12, 8081-8088.

Saka, H. (1983). Experimental evidence for Suzuki segregation to the stacking fault of an extended dislocation in a Cu-Si alloy, Philosophical Magazine A, 47, 131–140.

Saraswati, Sritharan, T., Pang, C. I., Chew, Y. H., Breach, C. D., Wulff, F., Mhaisalkar, S. G. and Wong, C. C. (2004). The Effects of Ca and Pd dopants on gold bonding wire and gold rod. *Thin Solid Film*, 462-463, 351-356.

Schweinfest, R. & Paxton, A. T. & Finnis, M.W. (2004). Bismuth embrittlement of copper is an atomic size effect. *Nature*, 432, 1008-1011.

Scholtz, F., Driver, J. H. & Woldt, E. (1999). The stored energy of cold rolled ultra high purity iron. *Scripta Materialia*, 40, 949-954.

Shang, J. X. & Wang, C. Y. (2001). J. Phys, "Electronic effects of alloying elements Nb and V on body-centered-cubic Fe grain boundary cohesion**.** *Journal of Physics: Condensed Matters*, 13, 9635-9644.

Shah, M., Zeng, K. & Tay, A.A.O. (2004). Mechanical characterization of the heat affected zone of gold wirebonds using nanoindentation. *Transactions of the ASME. Journal of Electronic Packaging*. 126, 87-93.

Shen, Y. F., Lu, L., Lu, Q. H., Jin, Z. H. & Lu, K. (2005). Tensile properties of copper with nano-scale twins. *Scripta Materialia*. 52, 989–994.

Simons, C., Schrapler, L. & Herklotz, G. (2000). Doped and Low-Alloyed Gold

Bonding Wires. *Gold Bulletin*, 33, 89-96.

Smallman, R. E. & Ngan, A. H. W. (2007). *Physical Metallurgy & Advanced Materials*. Amsterdam: Butterworth-Heinemann. Ch. 4.

Small Precison tool website (2009): http://www.smallprecisiontools.com/gold-ball-wire-bonding-Process?sprache=en

Song, R., Ponge, D. & Raabe, D. (2005) Improvement of the work hardening rate of ultrafine grained steels through second phase particles. *Scripta Materialia.* 52, 1075-1080.

Stephan, D. (2008). Process flow of Au wires, Kulicke & Soffa.

Subramanian, S., Muller, D. A., Silcox, J., Sass, S. L. (1997). Chemistry, bonding and fracture of grain boundaries in Ni_3Si. *Acta Matererialia*, 45, 3565-3571.

Sun, B. B., Sui, M. L., Wang, Y. M., He, G., Eckert, J., Ma, E. (2006). Ultrafine composite microstructure in a bulk Ti alloy for high strength, strain hardening and tensile ductility. *Acta Materialia*, 54, 1349-1357.

Swygenhoven, v., Caro, H., Farkas, A. D. (2001), Grain boundary structure and its influence on plastic deformation of polycrystalline FCC metals at the nanoscale: a molecular dynamics study. *Scripta Materialia*, 44, 1513-1516.

Tan Thiam Teck. (2003). Effects of Varying Mechanical Deformation on the Relationship between Microtexture, Mesotexture and Current Percolation in Superconductos. PhD Thesis.

Torre, F. D., Swygenhoven, H. V., Victoria, M. (2002). Nanocrystalline electrodeposited Ni: microstructure and tensile properties. *Acta Materialia*. 50, 3957– 3970.

Valiev, R. Z., Alexandrov, I. V., Zhu, Y. T. & T.C. Lowe. (2002). Paradox of strength and ductility in metals processed by severe plastic deformation. *Journal of Materials Research,* 17, 5-8.

Valiev, R. Z., Kozlov, E. V., Ivanov, Y. F., Lian, J., Nazarov, A. A. & Baudelet, B. (1994). Deformation behaviour of ultrafine-grained copper. *Acta Metallurgica Materialia*, 42, 2467- 2475.

Valiev, R. Z., Ivanisenko, Y. V., Rauch, E. F. & Baudelet, B. (1996). Structure and deformation behavior of Armco iron subjected to severe plastic deformation. *Acta Materialia*, 44, 4705-4712.

Valiev, R. Z., Estrin, Y., Horita, Z., Langdon, T. G., Zehetbauer, M. J. & Zhu, Y. T. (2006). Producing bulk ultrafine-grained materials by severe plastic deformation. *Journal of the Minerals, Metals and Materials Society*, 10, 33-39.

Vardaman, E. Jan. (2007), presentation on 'Advanced Packaging Interconnect Trends and Technology Developments'. [On-line]. Available: www.kns.com/_temp/downloads/agendaJuly2007/1.pdf

Valle, J. A. D., Carreno, F., Ruano, O. A. (2006). Influence of texture and grain size on work hardening and ductility in magnesium-based alloys processed by ECAP and rolling. *Acta Materialia*, 54, 4247 – 4259.

Wakai, F., Nagano, T. & Iga, T. (1997). Hardening in creep pf Aluminium by Zirconium Segregation at the grain boundary. *Journal of American Ceramics Society*, 80, 2361-2366.

Walker, Christopher, (2009): http://www.uksaf.org/tech/eels.html.

Wang, Y. M., Ma, E., Chen, M. W. (2002). Enhanced tensile ductility and toughness in nanostructured Cu. Applied Physics Letter, 80, 2395-2397.

Wang, Y.M., Ma, E. (2004a). Three strategies to achieve uniform tensile deformation in a nanostructured metal. *Acta Materialia*, 52 , 1699-1709.

Wang, Y. M., Ma, E. (2004b). Strain hardening, strain rate sensitivity, and ductility of nanostructured metals. Materials Science and Engineering A, 46, 375-377.

Warren, B. E. (1969). *X-Ray Diffraction.* Reading: Addison-Wesley.

Winter, M. (1993). Webelement .[On-line]. Available: http://www.webelements.com/.

Wei, Q., Cheng, S., Ramesh, K. T. & Ma, E. (2004). Effect of nanocrystalline and ultrafine grain sizes on the strain rate sensitivity and activation volume: fcc versus bcc metals. *Materials Science and Engineering A*, 381, 71-79.

Williams, D. B. & Carter, C. B. (1996). *Transmission Electron Microscopy: A Text Book for Materials Science,* New York & London: Plenum Press.

Williamson, G. K. & Hall, W. H. (1953). X-ray line broadening from filed aluminum and wolfram. *Acta Metallurgical*. 1, 22-31.

Weiland, H., Field, D. P. & Adams, B. L.(1986). *Experimental Techniques for Texture Analysis*. Oberursel: DGM.

Wright, S.I., Adams, B.L. & Kunze, K. (2005). Application of a new automatic lattice orientation measurement technique to polycrystalline aluminium. *Materials Science & Engineering A.* 160, 229-240.

Wu, A., Freeman, J. & Olson, G. B. (1996).Effects of carbon on Fe-grain-boundary cohesion: First-principles determination, *Physical Review B*. 53, 7504-7509.

Wu, X., Tao, N., Hong, Y., Lu, J. & Lu, K. (2005). γ, ε martensite transformation and twinning deformation in fcc cobalt during surface mechanical attrition treatment. *Scripta Materialia,* 52, 547-551.

Wu, X., Y. T. Zhu, M. W. Chen & E. Ma. (2006a).Twinning and stacking fault formation during tensile deformation of nanocrystalline Ni. *Scripta Materialia*. 54, 1685-1690.

Wu, X. L. & Ma, E. (2006b). Dislocations in nanocrystalline grains. *Applied Physics Letter*, 88, 231911-1-231911-3.

Wulff, F., Breach, C. D., Dittmer, K. (2003). Crystallographic texture of drawn gold bonding wires using electron backscattered diffraction (EBSD). *Journal of Materials Science Letters*, 22, 1273-1376.

Yamaguchi, M., Shiga, M. & Kaburaki, H. (2005). Grain boundary decohesion by Impurity Segregation in a Nickel-Sulfur System. *Science*, 307, 393-397.

Yamakov, V., Wolf, D., Phillpot, S. R., Mukherjee, K. & Glieter, H. (2004). Deformation-mechanism map for nanocrystalline metals by molecular-dynamics simulation. *Nature Materials*, 3, 43-47.

Yan, Y., Chisholm, M. F., Duscher, G., Maiti, A, Pennycook, S.J. & Pantelides,S.T. (1998). Impurity induced structural transformation of a MgO grain boundary. *Physical Review Letters,* 1998, vol 81, no 17, 3675-3678.

Yin, W. M. & Whang, S. H. (2001). Creep in Boron-doped nanocrystalline Nickel. *Scripta Materialia*, 44, 569-574.

Yin, W. M., Whang, S. H., Mirshams, R. A. (2005). Effect of interstitial on tensile strength and creep in nanostructured Ni, *Acta Materialia*. 53, 383-392.

Youngdahl, C. J., Weertman, J. R., Hugo, R. C. & Kung, H. H. (2001). Deformation behaviour in nanocrystalline copper. *Scripta Materialia*, 44, 1475–1478.

Youssef, K. M., Scattergood, R. O., Murty, K. L., Horton, J. A., C. C. Koch. (2005a). Ultrahigh strength and ductility of bulk nanocrystalline copper. *Applied physics letters*, 87, 091904-1- 091904-3.

Youssef, K. M., Scattergood, R. O., Murty, K. L., Koch, C. C. (2005b). Nanocrystalline Al–Mg alloy with ultrahigh strength and good ductility. *Scripta Materialia*. 54, 251-256. Mg 5%.

Valiev, R. Z., Alexandrov, I. V., Zhu, Y. T., Lowe, T. C. (2002). Paradox of strength and ductility in metals processed by severe plastic deformation. *Journal of Materials Research*. 17, 5-8.

Zehetbauer, M. &Seumer, V., (1993). Cold work hardening in stages IV and V of F. C. C. metals- I. Experimental and interpretation. *Acta Metallurgical et Materialia*, 41, 577-588.

Zhang, X., Wang, R. & Koch, C. C. (2004). Mechanical behaviour of bulk ultrafine-grained and nanocrystalline Zn. *Review of Advanced Materials Science*. 6, 53-93.

Zhang, X. H., Wang, H. Y., Kassem, M., Narayan, J. & Koch, C. C. (2001). Origins of Stored Enthalpy in Cryomilled Nanocrystalline Zn. J. Mat. Res. 16, 3485-3495.

Zhao, Y. H., Zhu, Y. T., Liao, X. Z., Horita, Z. & Langdon, T. G. (2006a). Tailoring stacking fault energy for high ductility and high strength in ultrafine grained Cu and its alloy. *Applied Physics Letters.* 89, 121906-121906-3.

Zhao, Y. H., Bingert, J. F., Liao, X. Z., Cui, B. Z., Han, K., Sergueeva, A. V., Mukherjee, A. K., Valiev, R. Z., Langdon, T. G., Zhu, Y. T. (2006b). Simultaneous increasing the ductility and strength of ultrafine-grained pure copper. *Advanced Materials*. 18, 2949-2953.

Zhao, Y. H., Zhu, Y.T., Liao, X. Z., Horita, Z., Langdon, T. G. (2007). Influence of stacking fault energy on the minimum grain size achieved in severe plastic deformation. *Materials Science and Engineering A*, 463, 22-26.

Zhao, Y. H., Topping, T., Bingert, J. F., Dangelewicz, A. M., Li, Y., Liu, W., Zhu, Y.T., Zhou, Y. Z., Lavernia, E.J. (2008a). High tensile ductility and strength in bulk nanostructured Nickel. *Advanced Materials*. 9999, 1-6.

Zhao, Y. H., Guo, Y. Z., Wei, Q., Dangelewicz, A.M., Xu, C., Zhu, Y.T., Langdon, T.G. , Zhou, Y. Z., Lavernia, E.J. Influence of specimen dimensions on the tensile behavior of ultrafine-grained Cu, Scripta Materialia (2008b), doi: 10.1016/j.scriptamat.2008.05.031.

Zhu, Y. T., Liao, X. Z. (2004). Nanostructured metals: retaining ductility. *Nature Materials,* 3, 351-352.

Zimmerman, A. F., Palumbo, G., Aust, K.T., Erb, U. (2002). Mechanical properties of nickel silicon carbide nanocomposites. *Materials Science Engineering A*. 328, 137-146.

Appendix
Author's Publication List

Journal

1. Y. H. Chew, C. C. Wong, C. D. Breach, F. Wulff, S. G. Mhaisalkar , C. I. Pang, Saraswati. (2004). Effects of calcium and palladium on mechanical properties and stored energy of hard-drawn gold bonding wire, Thin Solid Film, 462-463, 346-350.
2. Y. H. Chew, C. C. Wong, C. D. Breach, F. Wulff, S. G. Mhaisalkar. (2006). Effects of calcium on the mechanical properties of ultra-fine grained gold wires, Journal of Alloys and Compounds, 415, 193-197.
3. Y. H. Chew, C. C. Wong, C. D. Breach, F. Wulff, T. T. Lin, C. B. He. (2006). Effects of Ca on grain boundary cohesion in Au ballbonding wire, Thin Solid Film, 504, 346-349.
4. Y. H. Chew, C. C. Wong, C. D. Breach, F. Wulff, S. G. Mhaisalkar. (2006). Doping-induced simultaneous improvement of strength and ductility in ultrafine grained gold wires, Journal of Materials Research, 21, 2345-2353.
5. Y. H. Chew, C. C. Wong, F. Wulff, F. C. Lim and H. M. Goh. (2008). Strain rate Sensitivity and Hall-Petch Behavior of Ultrafine-grained Gold Wires, Thin Solid Films, 516, 5376-5380.
6. Saraswati, T. Sritharan, C. I. Pang, Y. H. Chew, C. D. Breach, F. Wulff, S. G. Mhaisalkar, and C. C. Wong. (2004). The Effects of Ca and Pd dopants on gold bonding wire and gold rod, Thin Solid Film, 462-463, 351-356.
7. Y. H. Chew, C, Ferraris, H. K. Hui, F. Wulff, Y. H. Zhao, E. J. Lavernia, C. C. Wong. Tailoring grain size and orientation for simultaneous improvement of

strength and ductility in ultrafine-grained gold wires, submitted to Scripta Materialia.

8. Y. H. Chew, H. K. Hui, D. Stephan, Y. H. Zhao, E. J. Lavernia, C. C. Wong. Creep of Ultrafine-crystalline Gold Wires with Calcium doping, submitted to Journal of Alloys and compounds.
9. Y. H. Chew, F. Wulff, H. K. Hui, Y. H. Zhao, E. J. Lavernia, C. C. Wong. Invited to contribute a paper to a special topic volume of Materials Science Forum: Ductility of Nanostructured Materials by Dr Y. H. Zhao from UC Davis.

Conferences

1. Y. H. Chew, C. C. Wong, C. D. Breach, F. Wulff, S. G. Mhaisalkar , C. I. Pang, Saraswati. Effects of calcium and palladium on mechanical properties and stored energy of hard-drawn gold bonding wire, oral presentation at International Conference On Materials for advanced Technologies (ICMAT) 2003, Singapore.
2. Y. H. Chew, C. C. Wong, C. Breach, F. Wulff, S. G. Mhaisalkar, S. L. Lim. Interaction Effects between Calcium and Palladium Dopants on the Mechanical Properties of Fine Gold Bonding Wire, oral presentation at International Conference On Materials Processing For Properties and Performance (MP3) 2004, Singapore.
3. Y. H. Chew, C. C. Wong, C. D. Breach, F. Wulff, T. T. Lin, C. B. He. Effects of Ca on grain-boundary cohesion in Au ballbonding wire, oral presentation at ICMAT 2005, Singapore.
4. Y. H. Chew, C. C. Wong, F. Wulff, F. C. Lim, H. M. Goh. Strain rate Sensitivity and Hall-Petch Behavior of Ultrafine-grained Gold Wires, oral presentation at Thin Films 2006, Singapore.
5. Y. H. Chew, C. C. Wong, Z. Bakar, J. Ling. First-principles Simulation Study on the Effects of Dopants on the Cohesion of Gold Grain Boundary, oral presentation at 32nd IEEE components, packaging and manufacturing technology society

(CPMT), International Electronics Manufacturing Technology Symposium 2008, San Jose, CA (USA).

6. Y. H. Chew, C. C. Wong, C. Ferraris, H. H. Kim. Simultaneous Improvement of Ductility and Strength by Minute Doping in Ultrafine Grained Au Wires-experiment and First Principle Study, oral presentation and collected as on-line journal, at MRS Spring Meeting 2007, San Francisco, CA (USA).
7. D. Stephan, Y. H. Chew, H. M. Goh, E. Pasamanero, E. P. P. Theint, D. R. M. Calpito, J. Ling. A Comparison Study of the Bondability and Reliability. Performance of Au Bonding Wires with Different Dopant Levels, 9th Electronics Packaging Technology Conference (EPTC) 2007, Singapore.
8. C. W. Tok, I. Langut, A. Menache, D. R. M. Calpito, Y. H. Chew. Wire Bonding Improvement Through Optimal Bonding Tools And Materials Selection, 9th EPTC 2007, Singapore.
9. D. Stephan, H. M. Ho, Y. H. Chew, S. Sutiono, H. M. Goh, D. R. M. Calpito, J. Yeung. Reliability Performance and Bondability of Soft Copper Wires, accepted for oral presentation at EPTC 2008, Singapore.
10. Y. H. Zhao, T. Topping, Y. Li, J. F. Bingert, P. Sun, Effie Chew, Wong C. C., R. Z. Valiev, Y. T. Zhu, Y. Z. Zhou, E. J. Lavernia. Microstructure-ductility relationship of ultrafine-grained materials, accepted for oral presentation at TMS Meeting 2009, San Francisco, CA (USA).